Optimized high energy resolution in γ-ray spectroscopy with AGATA triple cluster detectors

Inaugural-Dissertation
zur
Erlangung des Doktorgrades
der Mathematisch-Naturwissenschaftlichen Fakultät
der Universität zu Köln

vorgelegt von
Andreas Wiens
aus Karaganda, Kasachstan

Berichterstatter:	Prof. Dr. Peter Reiter Prof. Dr. Jan Jolie
Tag der mündlichen Prüfung:	20.06.2011

Kurzzusammenfassung

Der AGATA Demonstrator besteht aus fünf AGATA Tripel-Cluster (ATC) Detektoren. Jeder dieser Detektoren beinhaltet drei asymmetrische, 36-fach segmentierte, gekapselte, hochreine Germaniumdetektoren. Der Demonstrator soll die Anwendbarkeit des ortsempfindlichen Nachweises der γ-Strahlung mit Hilfe der Pfadrekonstruktion des γ-Quants (γ-ray Tracking) anhand von Impulsformanalyse zeigen. Die vorliegende Arbeit beschreibt die Eigenschaften für den ortsabhängigen Nachweis innerhalb des Germaniumdetektors, sowie die Optimierungsmaßnahmen an den ersten Tripel-Cluster-Detektoren. Für die Energieauflösung und die Impulsformanalyse ist eine hohe Signalqualität notwendig. Die Signalqualität und die Energieauflösung wurden durch die Modifikation der elektronischen Eigenschaften, v.a. des Erdungskonzeptes des Detektors, verbessert.

Der erste Teil der Arbeit bestand darin, vier Tripel-Cluster-Detektoren am INFN (Nationales Institut für Kernphysik) in Legnaro, Italien, für den AGATA Demonstrator vor den ersten Commissioning- und Kernphysikexperimenten in Betrieb zu nehmen. Die vier ATC Detektoren vereinen 444 hochauflösende Spektroskopiekanäle, eine von der Signalanzahl und Dichte zum ersten Mal erreichte Quantität für In-Strahl γ-Spektroskopie-Experimente. Die sehr gute Qualität der ATC Detektoren wird charakterisiert durch eine durchschnittliche Energieauflösung der Segmente eines jeden Kristalls zwischen $1,943$ und $2,131\,\mathrm{keV}$ bei einer γ-Energie von $1,33\,\mathrm{MeV}$ für die ersten 12 Kristalle. Das Übersprechen (Crosstalk) zwischen den einzelnen Detektoren in den Tripel-Clustern ist vernachlässigbar gering. Das Übersprechen innerhalb eines Kristalls beläuft sich auf ein Niveau von 10^{-3}.

Im zweiten Teil der Arbeit wurden neue Messmethoden zur Verbesserung der Energieauflösung der hochsegmentierten und ortsempfindlichen Detektoren entwickelt. Das Signal-zu-Rausch-Verhältnis wurde verbessert, indem das Zentralelektroden- (Core-) und das Segmentsignal gemittelt wurden. Die Mittelung führte zu einer Verbesserung der Energieauflösung von $21\,\%$ bei γ-Energien von $60\,\mathrm{keV}$ zu einer Halbwertsbreite von $870\,\mathrm{eV}$. Die Kombination mit der Crosstalk-Korrektur brachte für jegliche Segmentmultiplizität eine klare Verbesserung der Energieauflösung hervor. Bei Energien von $1,33$ wurde eine Verbesserung von $20\,\%$ erreicht.

Die Untersuchung des Elektronentrappingeffekts wurde mit einem neuen ortsabhängigen Korrekturverfahren für die Energiemessung abgeschlossen. Die Elektronentrappingkorrektur führte zu einer zusätzlichen Verbesserung der Halbwertsbreite der

Peaks in den γ-Spektren. Eine absolute Energieauflösung von $2,01\,\mathrm{keV}$ wurde bei einer γ-Energie von $1,33\,\mathrm{MeV}$ in dem segmentierten, großvolumigen AGATA Germaniumdetektor erzielt. Der ortsempfindliche Betrieb der Detektoren ermöglichte die Berechnung des Fano-Faktors, der sich auf $F = 0,095 \pm 0,005$ belief. Insgesamt wurde eine signifikante Verbesserung der Energieauflösung erzielt, so dass die neuartigen, segmentierten HPGe AGATA Detektoren mit deutlich verbesserten Eigenschaften den üblichen Ge-Detektoren in der Energie und Ortsauflösung überlegen sind. Die wesentlichen Verbesserungen beruhen zum einen auf der redundanten Energieinformation von unabhängigen Zentralelektroden- und Segmentsignalen, zum anderen auf der Korrektur der ortsabhängigen Trappingeffekte.

Abstract

The AGATA demonstrator consists of five AGATA Triple Cluster (ATC) detectors. Each triple cluster detector contains three asymmetric, 36-fold segmented, encapsulated high purity germanium detectors. The purpose of the demonstrator is to show the feasibility of position-dependent γ-ray detection by means of γ-ray tracking, which is based on pulse shape analysis. The thesis describes the first optimization procedure of the first triple cluster detectors. Here, a high signal quality is mandatory for the energy resolution and the pulse shape analysis. The signal quality was optimized and the energy resolution was improved through the modification of the electronic properties, of the grounding scheme of the detector in particular.

The first part of the work was the successful installation of the first four triple cluster detectors at INFN (National Institute of Nuclear Physics) in Legnaro, Italy, in the demonstrator frame prior to the AGATA commissioning experiments and the first physics campaign. The four ATC detectors combine 444 high resolution spectroscopy channels. This number combined with a high density were achieved for the first time for in-beam γ-ray spectroscopy experiments. The high quality of the ATC detectors is characterized by the average energy resolutions achieved for the segments of each crystal in the range of 1.943 and $2.131\,\mathrm{keV}$ at a γ-ray energy of $1.33\,\mathrm{MeV}$ for the first 12 crystals. The crosstalk level between individual detectors in the ATC is negligible. The crosstalk within one crystal is at a level of 10^{-3}.

In the second part of the work new methods for enhanced energy resolution in highly segmented and position sensitive detectors were developed. The signal-to-noise ratio was improved through averaging of the core and the segment signals, which led to an improvement of the energy resolution of $21\,\%$ for γ-energies of $60\,\mathrm{keV}$ to a FWHM of $870\,\mathrm{eV}$. In combination with crosstalk correction, a clearly improved energy resolution was achieved for events of each hit-segment multiplicity. For γ-ray energies of $1.33\,\mathrm{MeV}$, an improvement of $20\,\%$ was achieved.

The study of electron trapping using a new position-sensitive correction method for the energy measurement was completed. The correction of electron trapping resulted in an additional improvement of the full width at half maximum of the peaks of the γ-spectra. A total energy resolution of $2.01\,\mathrm{keV}$ at $1.33\,\mathrm{MeV}$ was achieved with a segmented, large volume germanium detector. The position-sensitive operation enabled calculating the Fano factor, which resulted in $F = 0.095 \pm 0.005$. Eventually, a significant improvement of the energy resolution was achieved. Consequently,

the novel segmented high-purity germanium AGATA detectors are operated at significantly improved conditions superior to the common Ge detectors in energy and position resolution. The essential improvement arises from the redundant energy measurement of independent core and segment electrodes and from the correction of the position-dependent trapping effects.

Contents

Kurzzusammenfassung **ii**

Abstract **v**

1 Introduction and Motivation **1**
1.1 The Advanced Gamma Tracking Array AGATA 1
1.2 Interaction of γ-rays with matter 4
1.3 Pulse shape analysis PSA 4
1.4 γ-ray tracking 6
1.5 Outline 6

2 Properties of high-purity germanium detectors **9**
2.1 High-purity germanium 9
2.2 The electric field of a germanium diode 10
2.3 The detector signal formation 11
2.4 Energy resolution 11

3 The ATC and its development **15**
3.1 The AGATA crystals 15
3.2 The AGATA triple cryostats 18
3.3 The AGATA preamplifiers 18
3.4 Assembly and adjustment of the ATC detector 22

4 Properties of the ATC detector **37**
4.1 The single detector test 37
4.2 Energy resolution of the first ATC detectors 38
4.3 Crosstalk properties 49
4.4 The AGATA demonstrator in Legnaro, Italy 51

5 Averaging of the core and the segment signals **57**
5.1 Averaging at low energies 58
5.2 Crosstalk correction 68
5.3 Averaging of multifold events 70

6 Charge carrier trapping and its correction **73**
6.1 The origin of trapping 73
6.2 Model for trapping correction 75
6.3 Experimental analysis of electron trapping 78

7 Summary and outlook **97**

References **101**

Acknowledgements **107**

List of Figures

1.1 Schematic figure of the different constituents for γ-ray tracking 2
1.2 AGATA configuration with 180 crystals in 60 triple clusters 3
1.3 Energy dependent attenuation coefficients for γ-ray interactions . . . 5
1.4 Schematic representation of the AGATA demonstrator 7

2.1 Weighting potential ϕ for a segment of a six-fold segmented, coaxial detector 12

3.1 Drawing of the three different crystal geometries 16
3.2 Drawing of the dimensions for the crystal and its segmentation with the segment labeling in the right picture. 17
3.3 Processing steps of the AGATA detector from the bare Ge-crystal to an encapsulated detector 17
3.4 Pictures of the ATC detector 19
3.5 Schematic of detector and electronics compound 20
3.6 Photographs of the three AGATA preamplifiers 21
3.7 FFT spectra for different bias voltages 24
3.8 Main observed oscillations in time and frequency domain 25
3.9 Energy spectrum showing the 1.33MeV line suffering from HF 26
3.10 Microphonic oscillation of baseline shown in frequency and time domain 26
3.11 Capacitance network simulating detector capacitors for tests of preamplifier rise times. 28
3.12 Preamplifier response with different rise times 29
3.13 FFT spectrum of first channel of segment preamplifier before and after modification 30
3.14 Micro match connector showing fretting corrosion 31
3.15 Preamplifier housing with micro match connectors short connected and micro match connector replaced by Fischer connector 32
3.16 Modified carrier PCB for preamplifiers. Top layer of the PCB and dimensions 33
3.17 Test of susceptibility to electromagnetic disturbances at different frequencies with a fast pulser. 34
3.18 Core noise after injection of a fast pulser signal of 1 kV amplitude . . 34

3.19 FFT spectra of the two crystals A and B in the detector ATC1 measured in Legnaro . . . 36

4.1 A single test cryostat for detector tests and characterization measurements. . . . 39
4.2 The triple cluster detector test setup at IKP . . . 39
4.3 The 18 segment spectra of the three sectors A, B, and C measured with ATC1 detector B002 in Legnaro . . . 44
4.4 The 18 segment spectra of the three sectors D, E, and F measured with ATC1 detector B002 in Legnaro . . . 45
4.5 Spectra measured with ^{241}Am and ^{57}Co simultaneously and with ^{60}Co 46
4.6 The peak-to-total ratio for the 36 segments in ATC1 detector B002 . . 46
4.7 Energy resolution values for 122 keV for the core signal and 60 keV for the segment signals . . . 47
4.8 Energy resolution values for the core signal and the segments for ATC1 at 1.33 MeV . . . 48
4.9 Results of the crosstalk measurements of the detectors A001, B002 and C002 in single test cryostats . . . 50
4.10 Relative crosstalk contributions for subsets of the sectors A and F of each detector and the cores . . . 52
4.11 The AGATA demonstrator with four ATC detectors at INFN, Legnaro in summer 2010. . . . 55
4.12 Position information of the interaction points from the PSA for collimated pencil beam . . . 56

5.1 Source positions in the measurement. . . . 59
5.2 Spectra for the core gated by A1 and the average signal of A1 . . . 60
5.3 Energy resolution values for core signals, segments and core-segment average . . . 60
5.4 Energy resolution values for the core-segment average gated by individual segments compared to the calculated expected values . . . 61
5.5 37 $\times$ 37 covariance matrix for all 37 detector signals in S002 from 7.3 μs of noise samples. . . . 62
5.6 Core energy vs. segment energy matrix for segment A1 in detector S002 63
5.7 Core energy vs. segment energy matrix for segment A1 in detector C002 at 1.3 MeV . . . 64
5.8 ^{152}Eu spectrum with 122 keV inset measured with detector B002 in ATC1 . . . 65
5.9 Energy resolution at different energies of ^{152}Eu measured and calculated 66
5.10 Energy dependence plot on the absolute energy resolution . . . 67
5.11 The segment sum energies for 1332.5 keV plotted for different segment multiplicities . . . 68

5.12 Energy shift of the 1.3 MeV γ-ray energy versus number of hit segments for uncorrected and corrected spectra 69
5.13 The add-back segment-sum spectrum of the 1.33 MeV γ ray energy uncorrected and crosstalk corrected 70

6.1 Levels of impurities in Ge band gap 74
6.2 Trapping sensitivities plots for the core for a cut through the center of the detector 77
6.3 Trapping sensitivities plots for segments for a cut through the center of the detector 78
6.4 A clear energy deficit with rising radius is observed due to electron trapping as the electrons are collected at the core electrode. 79
6.5 Radius vs. trapping sensitivities at detector depth $z = 70\,\mathrm{mm}$ for interaction positions determined by the PSA for a measurement with detector B002. 80
6.6 Measured peak energy vs. calculated sensitivity plotted for first two rings for onefolds 80
6.7 Measured peak energy vs. calculated sensitivity plotted for back rings 82
6.8 Impurity concentration vs. slope of fit for each ring 83
6.9 The electric field is plotted vs. radius for two different impurity concentrations 83
6.10 Energy vs. radius matrices at 1.33 MeV in first ring of detector C002 . 85
6.11 Spectra for core, segments, and average of corrected core and segment energy 86
6.12 Centroids of the 1.33 MeV line are plotted for radius intervals of 4 mm for onefold events 87
6.13 FWHM for spectra in radius intervals of $\Delta r = 4$ mm for the core, the segments, and the core-segment average signals 88
6.14 FWHM for the core and the segments at $1.33\,\mathrm{MeV}$ for $\Delta r = 5\,\mathrm{mm}$ and $\Delta z = 10\,\mathrm{mm}$ detector rings measured with detector B002 in ATC1. 89
6.15 FWHM versus radius in the coaxial part of the detector B002 at 1.33 MeV 90
6.16 Energy versus slope of fit for the coaxial part for detector C002 for different energies 92
6.17 The difference in the energy resolution between the uncorrected and corrected spectra 92
6.18 Centroids of the spectra of uncorrected core signals in radius intervals of in 4 mm with a fit with position and energy errorbars together with corrected energy positions 94
6.19 ^{152}Eu spectrum for the uncorrected segment-sum and the final spectrum after trapping correction and signal averaging 95

7.1 The four AGATA triple cluster detectors mounted in the AGATA demonstrator frame in INFN Legnaro 98
7.2 FWHM values measured with ^{152}Eu for the core, uncorrected segment sum 99

Chapter 1

Introduction and Motivation

Major future developments in the experimental and theoretical study of the structure and dynamics of the atomic nucleus focus on exotic nuclei far from stability. This development comes along with the construction of the next generation of beam facilities for the production of instable ion beams. These high-intensity radioactive ion beam facilities are currently being developed world-wide and also bring along new challenges for instrumentation of nuclear spectroscopy. For high resolution γ-ray spectroscopy, the demanding new experiments will be performed with a new generation of γ-ray spectrometers like the Advanced Gamma Tracking Array AGATA [1, 2, 3] in Europe and the GRETA array (Gamma-Ray Energy Tracking Array) in the USA [4, 5].

1.1 The Advanced Gamma Tracking Array AGATA

Ideally, the new generation of γ-spectrometers provide the highest energy resolution together with the utmost detection efficiency to accommodate the requirements of low secondary beam intensity in a broad beam energy range. This energy ranges from the Coulomb energy regime, which is typical of future ISOL (Isotope Separation On-Line) facilities, to the intermediate and relativistic energy regimes of fragmentation facilities. To reach this goal, the novel technique of γ-ray tracking in electrically segmented germanium detectors will be employed. The tracking technique will allow a dramatic detection efficiency increase based on the very high solid angle coverage of a nearly completely closed 4π germanium shell. As a consequence, the concept of physical suppression shields has to be replaced by an equally effective and advantageous way to create photo-peak dominated, high quality spectra. The γ-ray tracking spectrometer will have an unprecedented level of detection sensitivity to γ-radiation.

The γ-ray tracking technique will be based on four different parts (see also Fig 1.1): (i) Highly segmented detectors so that individual γ-ray interactions are distributed over several different segments. (ii) Digital electronics is needed to register all 37 time-dependent signals from this detector. (iii) Pulse shape analysis methods will be employed to convert the traces online into position information. The pulse shapes of

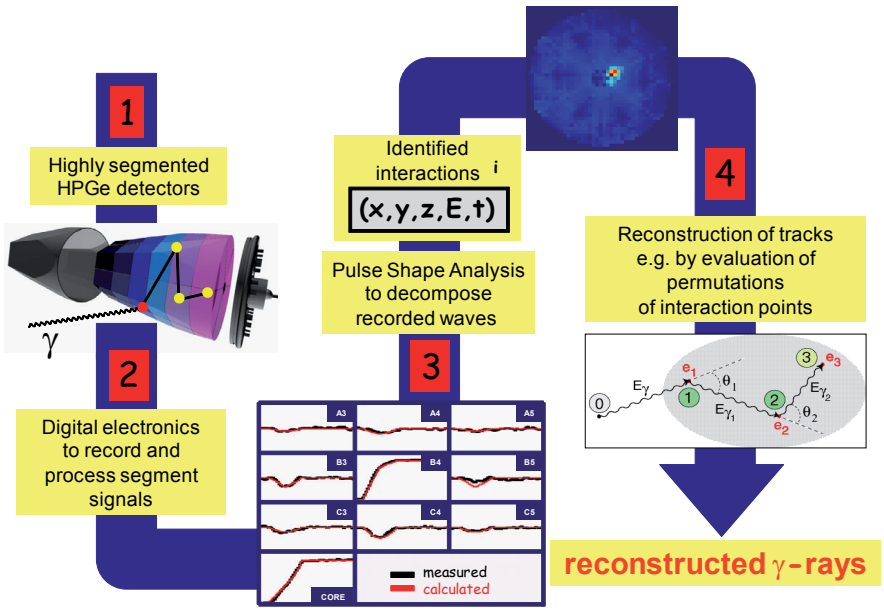

Figure 1.1: Schematic figure of the different constituents required for the new γ-ray tracking array [6].

the detector signals are uniquely determined by the positions of the interaction points. (iv) All energies and coordinates of coincident interactions are processed by the tracking algorithm. The tracking procedure will identify which of these interactions belong together and determine in which sequence they occur by using, for example, the Compton scattering rule.

The AGATA spectrometer will consist of AGATA Triple Cluster (ATC) detector modules. The detector module comprises three encapsulated HPGe detectors with different hexagonally shaped crystals. The high efficiency and very good solid angle coverage without suppression shields will be achieved by assembling the Ge crystals inside the composite cluster detectors with minimal spacing in between them. These types of detectors require a progression of the existing technology for encapsulated Ge cluster detectors, which started with the EUROBALL cluster detector [7, 8] and the MINIBALL cluster detector [9]. The final configuration of the AGATA spectrometer will comprise 60 cluster detector modules with 180 single HPGe detectors and will cover a huge solid angle of nearly 4π (schematic representation in Fig. 1.2).

The large solid angle coverage of almost $80\,\%$ combined with a crystal length of $9\,\mathrm{cm}$ provides a large efficiency for the γ-ray absorption. The total efficiency for the absorption of $100\,\mathrm{keV}$ γ-rays is more than $70\,\%$. Table 1.1 compares the main properties of the final AGATA configuration to an ideal homogenous Ge shell with $100\,\%$ solid angle coverage and $9\,\mathrm{cm}$ thickness. The thickness of the germanium shell, i.e. the crystal length, gains weight at larger energies. A total efficiency of $50\,\%$ is achiev-

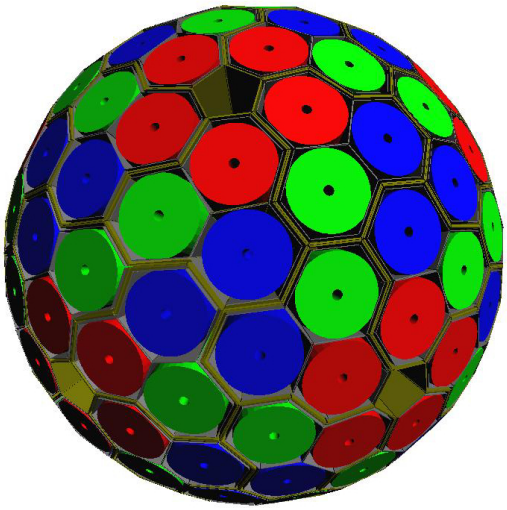

Figure 1.2: AGATA configuration with 180 crystals in 60 triple clusters. The three colors indicate three slightly different shapes of the crystals.

able for γ-rays of $1\,\mathrm{MeV}$. Even for energies around $E_\gamma = 10\,\mathrm{MeV}$ a total efficiency of $25\,\%$ is expected. The gain in efficiency compared to current spectrometers is pivotal for higher γ multiplicities. For γ multiplicities of $M_\gamma = 30$ and a γ-ray energy of $E_\gamma = 1\,\mathrm{MeV}$, the simulated total efficiency amounts to $25\,\%$.

Another feature of the AGATA spectrometer will be the high peak-to-total ratio. The use of the principle of γ-ray tracking will result in a peak-to-total ratio of up to $70\,\%$ for $M_\gamma = 1$ and $E_\gamma = 1\,\mathrm{MeV}$. For higher multiplicities of $M_\gamma = 30$ at the same energy, a peak-to-total ratio of $50\,\%$ is expected. These values are comparable to those of the current spectrometers EUROBALL and GAMMASPHERE, which are optimized for this purpose and operated with BGO Compton suppression shields to achieve the best peak-to-total ratio. The position-sensitive operation allows for an angular resolution of less than $1°$. Therefore, a Doppler correction enables to restore the energy resolution to $\Delta E/E < 0.5\%$ for γ-rays emitted by nuclei at velocities up to $v/c \sim 50\,\%$, which is only two times larger than the intrinsic energy resolution at $E_\gamma = 1\,\mathrm{MeV}$ [2].

The individual HPGe detector is made of n-type high-purity germanium. The outer contact of the crystal is electrically divided into 36 segments. Simultaneous signal processing of all the individual segments and the core contact is performed implying the well-known properties of a HPGe detector, a very high energy resolution, and good timing properties in particular. To achieve the highest energy resolution, the 37 preamplifiers are divided into a cold and a warm part at room temperature. The cold part is located in close proximity to the detector electrodes and is operated at cryogenic temperatures. The preamplifiers provide unperturbed signal traces from the time-dependent charge collection process inside the detector volume.

Properties of		an ideal Ge-shell	AGATA
Efficiency	E_γ=0.1 MeV, M_γ= 1, 0<β<0.5	100%	>70%
	E_γ=1 MeV, M_γ= 1, 0<β<0.5	72%	≈50%
	E_γ=10 MeV, M_γ= 1, 0<β<0.5	15%	≈10%
	E_γ=1 MeV, M_γ= 30, 0<β<0.5	36%	≈25%
P/T	E_γ=1 MeV, M_γ= 1	85%	60 - 70%
	E_γ=1 MeV, M_γ= 30	60%	40 - 50%
Angular resolution	$\Delta E/E < 1\%$	-	< 1°
Maximum	M_γ= 1	-	3 MHz
Event rate	M_γ= 30	-	0.3 MHz
Inner radius		150 mm	170 mm

Table 1.1: Comparison of the main properties of the detectors of the AGATA spectrometer and of an ideal Ge shell of $9\,\mathrm{cm}$ thickness and an inner radius of $150\,\mathrm{mm}$ [2].

1.2 Interaction of γ-rays with matter

In order to be measured, the γ-rays need to interact with the detector material. There are three main effects accomplishing the γ-ray interactions with matter. The three effects have different cross-sections, which depend on the photon energy and on the ordinal number Z of the absorbing material (see Fig. 1.3). The first effect is the photo effect, where the γ-ray transfers its whole energy to an electron and leaves an ionized atom behind. While the photo effect cross-section is proportional to $\sigma_{ph} \sim \frac{Z^{4-5}}{E^{3.5}}$, it is the most probable interaction below $200\,\mathrm{keV}$. The Compton effect describes the inelastic scattering of a photon at electrons with the photon transferring a part of its energy to an electron. With a cross-section of $\sigma_C \sim \frac{Z}{E}$, the Compton effect is the dominant interaction process between $200\,\mathrm{keV}$ and $8\,\mathrm{MeV}$ for germanium. Finally, the pair production creates an electron-positron pair in the Coulomb field of the atomic nucleus by absorbing the γ-ray of at least $1.022\,\mathrm{MeV}$, the rest mass of the electron-positron pair. The cross-section is proportional to $\sigma_{pp} \sim Z^2 \cdot \ln E$. The total interaction probability is the sum of the three effects.

1.3 Pulse shape analysis PSA

A good knowledge of the above-mentioned effects and the manifestations of their characteristics in the detector response are mandatory for γ-ray tracking as well as a precise determination of the interaction position. The outer electrode of the crystal is segmented to obtain position information about the γ-ray interaction. Not only the granularity of the cathode but also the pulse shapes facilitate the position determination. The pulse shapes in a multi electrode system are unique for any interaction

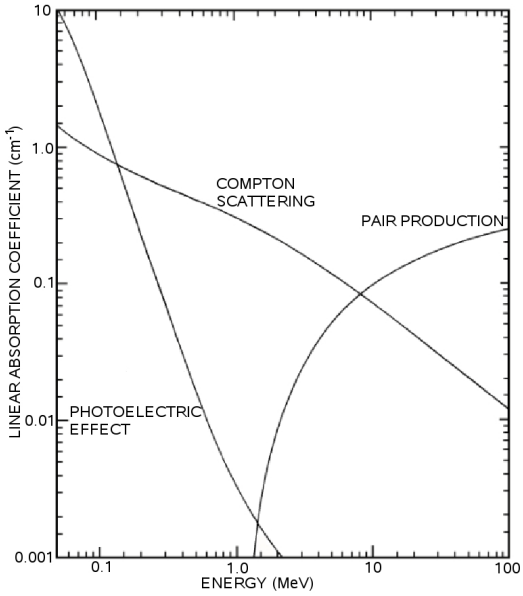

Figure 1.3: Energy dependent attenuation coefficients for the three kinds of interaction of γ-rays with matter.

position and are determined by the mobility of the charge carriers, the weighting potential of the segment electrodes, crosstalk properties, and the response function of the electronics.

The concept of weighting potential is used to describe the mirror charges, which are induced on the electrodes collecting the charge carriers as well as the transient charge signals. The transient signals appear in adjacent segments to those absorbing the γ-rays. The closer the interaction happens to a neighboring segment, the stronger the transient signal becomes. The radial information can be derived from the shape of the signal as electrons and holes show different drift velocities. For PSA a data base is needed which contains the pulse shapes of all the detector signals at any possible interaction position inside the HPGe crystal. Position information is obtained with a regular 3 dimensional grid of $2\,\mathrm{mm}$ grid distance. The pulse shapes are stored for each grid point. A comparison between measured pulse shapes and the pulse shapes of the data base library is used to determine the interaction positions. Ideally, the data base is created by the measured position-dependent detector response for each crystal. However the scan of a large volume crystal is very time-consuming. The use of highly collimated γ-ray sources limits the counting rate and a full scan takes up to three months for the large volume detector. As an alternative, the detector data base is calculated. Results of such pulse shape analysis calculations are given in [10, 11].

An adaptive grid search algorithm is used to decompose the pulse shapes [12] in real time. The algorithm compares the net and the transient signals of the detector to the calculated signals in the basis first on a coarse grid of $5\,\mathrm{mm}$. A second scan searches for the interaction positions in the detector on a finer grid of $2\,\mathrm{mm}$ in the re-

gion identified by the coarse search. The position in the grid providing the minimal χ^2 value for the comparison of the detector and the base signals is accepted as interaction position of the γ-ray.

1.4 γ-ray tracking

The boost in efficiency and in the peak-to-total ratio due to the γ-ray tracking technique arises from reconstruction of the track of the scattered photons inside the crystal and across all individual Ge detectors. The use of veto shields in earlier and current spectrometers limits the total solid angle coverage and rejected the scattered γ-rays between detectors. Spectrometers without Compton suppression shields show a poor peak-to-total ratio. Therefore a maximal solid angle coverage and a very good peak-to-total ratio cannot be obtained simulatneuosly with standard large volume Ge detectors.

For a total absorption of a $1.33\,\mathrm{MeV}$ photon, the most probable number of interaction points is four [4], i.e. before a total absorption, the γ-ray is scattered three times. The scattering may happen between segments or even between crystals. The duty of the tracking algorithm is to disentangle the coincident interaction points of the γ-ray, which are determined through the pulse shape analysis. The Compton scattering rule is applied by combining the energy and position information of the interaction as the energy deposition is angular-dependent in the Compton effect. Interaction belonging to one γ-ray can be identified as well as the order in which they occur. Two categorical tracking algorithms can be applied, back tracking and forward tracking, to get the sequence of the interactions [11].

The AGATA demonstrator is a subset of five ATC detectors of the final array. A schematic of the demonstrator is shown in figure 1.4. The purpose of the demonstrator is to show the feasibility of the principles of γ-ray tracking and pulse shape analysis under real experimental conditions in real time. An important part of the work that is presented in the present thesis was to assemble and install the very first ATC detectors at INFN (National Institute of Nuclear Physics) in Legnaro, Italy [13], to form the AGATA demonstrator.

1.5 Outline

For the new position-sensitive ATC detectors, the highest achievable quality of the detector signals is demanded to meet the specifications of the γ-ray tracking device. The highest energy resolution and a very good signal quality of all signal channels are mandatory to prove the functionality of the demonstrator, especially of the new techniques. A high energy resolution is required for the reconstruction of the γ-ray track via the Compton scattering formula of the tracking algorithm. Moreover, the expected very small energy peaks on a high background level can only be resolved and identified with the utmost energy resolution in the coming experiments at the rare

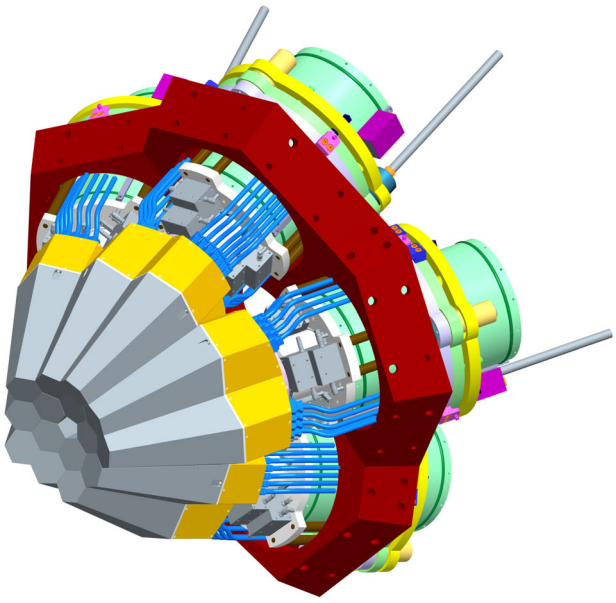

Figure 1.4: The AGATA demonstrator representing a subset of five ATC detectors of the whole spectrometer.

isotope beam facilities. Clean and unperturbed signals are needed for the pulse shape analysis. The net signals as well as the transient signals with the lowest noise level are important for the determination of the interaction position inside the crystal.

The first part of this thesis describes the assembly of the first ATC detectors. Each ATC detector has a higher integration of individual high energy resolution signals than entire current spectrometers like the GAMMASPHERE array. The complex system of an ATC detector with $6\,\mathrm{kg}$ of raw germanium and 111 high resolution channels is a complex and dense interplay of mechanically precise cryostat technology, high vacuum requirements, high voltage supply, low noise signal processing. At the end these new and ambitious detectors meet the requirements and specifications. A detailed description of the detector assembly procedure, debugging strategies, optimization procedures and the final performance of the ATC detectors is subject of this work. The detector properties, which were achieved and measured at the IKP (Institut für Kernphysik) in Cologne, were reproduced at the first host laboratory of the AGATA demonstrator array in Legnaro after integrating the detectors into the local infrastructure.

The properties of high-purity germanium are described with regard to the operation as a detector diode. The energy resolution is described in detail. The noise contributions to the full width at half maximum of the peaks in the γ-ray spectra as well as the new options to improve the resolution are discussed. One way to reduce the electronic noise of the detector is to average the cathode and the anode signals, which is typically not possible with standard HPGe detectors. This measuring scheme improves the signal-to-noise ratio, and consequently the energy resolution due to the statistical un-

correlated electronic noise of the two independent signals. This behavior is analyzed in a wide energy range and as a function of the segment multiplicity of the crystal. The signal averaging has to be combined with crosstalk correction to reach optimized results. Crosstalk appears in segmented detectors due to the mutual capacitive coupling of the core signal and the segment signals and the coupling of the segment signals.

Although the germanium crystals are extremely pure, electron trapping is observable during the migration of the charge carriers to the electrodes. Due to the large volume of the detectors, the long drift length in the crystal amounts up to a maximum of $4\,\mathrm{cm}$. A correction method for incomplete charge carrier collection due to trapping is presented in the last chapter. The new method is based on the position information which is available for the first time. As a final result, the energy resolution of the new ATC detectors was considerably improved. The combination of all measures provides an energy resolution of $\Delta E/E = 0.15\,\%$ for the new ATC detectors for γ-ray energies of $1.33\,\mathrm{MeV}$ for future γ-ray spectroscopy experiments.

Chapter 2

Properties of high-purity germanium detectors

2.1 High-purity germanium

Germanium is the material of choice in high resolution γ-ray spectroscopy. It is a semiconductor with a narrow band gap between the valence and conduction band of $0.7\,\mathrm{eV}$. Therefore, a large number of electron-hole pairs per incident γ-ray is created. This results in a relatively low fluctuation of charges for the γ-rays and thus in a very good energy resolution.

Nevertheless, due to the small band gap, a substantial amount of electrons is thermally excited at room temperature. An excited electron leaves a hole behind in the valence band so that an electron-hole pair is created. The probability to generate an electron-hole pair by thermal excitation is given by

$$p(T) = CT^{\frac{3}{2}} e\left(-\frac{E_g}{2k_B T}\right) \tag{2.1}$$

with temperature T, the width of the gap between valence and conduction bands E_g, the Boltzmann constant k_B and a characteristic proportionality constant of the material C. Therefore, a germanium detector has to be operated close to the liquid nitrogen temperature of $77\mathrm{K}$ to reduce the thermal excitation of the electrons to an insignificant level.

Although germanium can be produced as the purest bulk material at all, there is still a residual amount of impurities. Germanium can be categorized in n- and p-type material, depending on whether the impurities are of valence 5 or valence 3, while germanium is of valence 4. In practice, impurities of both kinds are found in the crystal. They create energy levels sitting in the forbidden band gap. The net effect in n-type germanium is characterized by a residual amount of donor impurities, which results in a much greater number of conduction electrons and in a smaller number of holes compared to the pure material. Therefore, electrons are called the majority

carriers. The very low net impurity concentration amounts to $10^9 - 10^{10}\,\mathrm{cm}^{-3}$ in the AGATA detectors in use. The most important dopants are P, As and Sb with donor levels at 0.12, 0.13 and $0.0096\,\mathrm{eV}$ below the conduction band [14]. These impurities are introduced intentionally in a controlled way on the level of $10^9 - 10^{11}\mathrm{cm}^{-3}$ during the growth of the crystal. A detailed analysis of the distribution of impurities in the germanium volume is described in [15].

2.2 The electric field of a germanium diode

To operate the germanium crystal as a detector, it needs to be equipped with electrodes. Ideally, these electrodes are as thin as possible and show a very high concentration of doped material, p^+ for the one and n^+ for the other electrode. Additionally, the p^+-doped electrode creates a junction with the n-type germanium. At a junction of differently doped material, a diffusion of the charge carriers is observed, which creates a space charge. In turn, the space charge creates an electric field. An equilibrium is established when the electric field prevents additional net diffusion. The buildup of net charge causes an electric potential φ. By solving the Poisson equation

$$\nabla^2\varphi = -\frac{\rho}{\epsilon}$$

one can find the electric potential depending on the charge density $\rho = eN_D$ with the electronic charge e and the density of donor impurities N_D at any point in the detector volume. The electric field is described by the gradient of the potential: $E = -\nabla\varphi$

However, this depleted region is very small but can be extended by an external high voltage so that the germanium is operated as a reverse-biased diode. The depletion, or the so-called active region for a planar detector is inversely proportional to the net impurity concentration N

$$d = (\frac{2\epsilon V}{eN})^{1/2}$$

Therefore, the bulk material is fully depleted at a certain voltage V for a given impurity concentration. With an impurity concentration of $10^{10}\,\mathrm{cm}^{-3}$, the depleted region spans $10\,\mathrm{mm}$ per reverse-biased $1000\,\mathrm{V}$ [16].

If a higher electric field is applied than needed for depletion, the electric potential and the electric field rise. The drift velocity of the charge carriers is strongly field-dependent. Therefore, a strong electric field due to overvoltage is desirable. But the electric field strength is not only proportional to the applied high voltage, it also depends on the impurity concentration of the crystal. The so composed electric field for a coaxial geometry is given by [17]:

$$E(r) = 2 \cdot \frac{eN_D}{4\epsilon} \cdot r + \frac{1}{r}\frac{V_0 - eN_D/4\epsilon}{ln(r_2/r_1)} \tag{2.2}$$

The equation 2.2 is used for the plot in figure 6.9. It shows the electric field in the Ge crystal of AGATA detector B002 at its maximum (front) and minimum (back)

impurity concentration assuming a cylindrical geometry. For smallest radii, the bias voltage is the dominant contribution to the electric field. At larger radii, the first summand in the equation outweighs and the electric field is proportional to the impurity concentration.

2.3 The detector signal formation

The electron-hole pairs, created by an absorption of an incident γ-ray in the depleted material, are separated in the presence of an electric field. They drift in opposite directions to the electrodes with certain drift velocities parallel to the direction of the applied field. The migrating charge carriers induce an electrical current on the electrodes $i(t) = q \cdot \nu \cdot E_\nu$ according to the Ramo theorem. The charge induced in the time interval between t and $t + dt$ is given by

$$\frac{dQ_i}{dt} = -n_{e,h}(t) \cdot (\vec{\nabla}\phi_i \cdot \vec{v}_{e,h})$$

where ϕ_i is the weighting potential on electrode i [18, 19]. The Ramo theorem allows for the creation of a time profile of the charge collection process according to the geometry of the electrodes and to the motion of the charge carriers towards the electrodes.

For a cylindrical detector geometry, equation 2.2 can be used to obtain the electrical field analytically. An impurity concentration of zero is assumed to describe the field only by the geometrical coupling of the electrodes. The weighting potential is a mathematical concept relying on the geometrical configuration of the electrodes for the description of other than planar or purely cylindrical detectors. Starting with the Green's reciprocity theorem, the weighting potential is calculated numerically for a special detector geometry by solving the Poisson equation assuming zero space charge and $1\mathrm{V}$ potential on one of the electrodes and zero V on all other electrodes [20, 21]. Simulation software, such as SIMION, is used to create the detector geometries and to calculate the weighting field by solving the Laplace equation. The calculated weighting field for a six-fold segmented, coaxial detector is shown in figure 2.1.

The signal is completely recorded when both electrons and holes are collected at the electrodes. Therefore, the rise time of the detector signal is determined by the drift velocities of the electrons and holes, which differ significantly for the two charge carriers [22]. The rise time also depends on the interaction position inside the crystal.

2.4 Energy resolution

The AGATA spectrometer takes advantage of the excellent energy resolution of $\Delta\, E/E \approx 10^{-3}$ provided by germanium detectors. The energy peak of a germanium detector for a certain mono-energetic γ-ray energy is ideally a Gaussian distribution

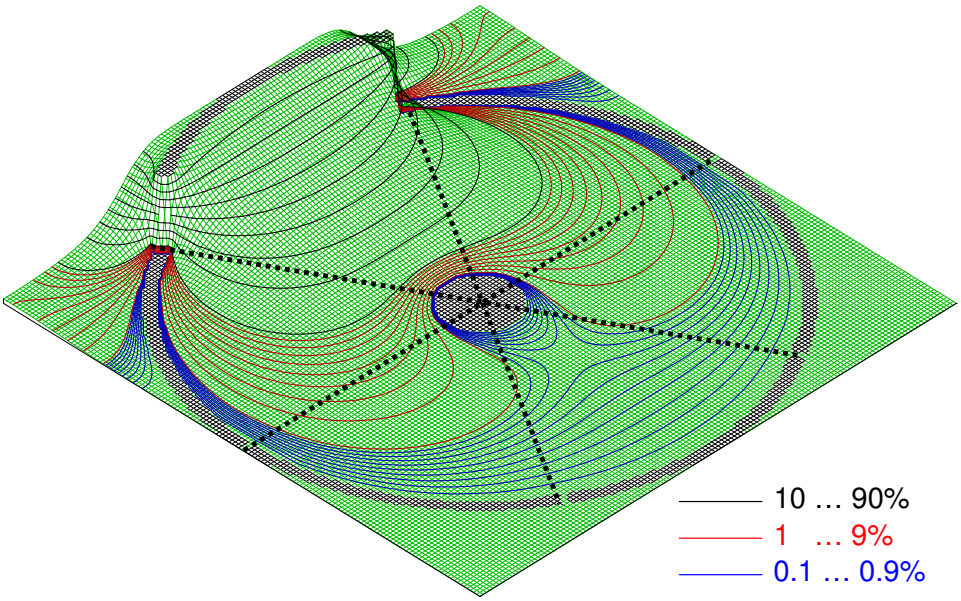

Figure 2.1: Weighting potential ϕ for a segment of a six-fold segmented, coaxial detector [23].

of the measured energy for the total absorption of the γ-ray if the number of measured events is high. The peaks can be fitted with the following function:

$$G(E) = h \cdot \exp\left(-\frac{(E - E_\gamma)^2}{2\sigma^2}\right)$$

The observed energy resolution is given by the width of the peak and three detection effects contribute in a separate way to the total width of the peak. The total full width at half maximum (FWHM) W_T^2 of a peak in a γ-spectrum arises from the statistical fluctuations of the charge carrier collection process, from charge carrier loss and from electronic noise:

$$W_T^2 = W_D^2 + W_X^2 + W_E^2 \tag{2.3}$$

The fast electrons created through the interaction of γ-rays with the germanium material are slowed down to thermal velocity through collisions and excitation of other slow electrons. The average number of slow electrons and holes produced by a γ-ray is proportional to the energy absorbed by the detector. The creation of electron-hole pairs competes with phonon excitation. Therefore the average ionization energy is $2.96\mathrm{eV}$ instead of the bad gap value of $0.7\mathrm{eV}$. The conversion underlies obligatory fluctuations in the number of electrons produced. The probability of the production of each slow electron is not an independent process. Thus, the Poisson distribution is not applicable and the variance of the electron-hole pairs is generally smaller. The Fano factor F is estimated to be approximately 0.1 in germanium detectors. It describes the ratio of the

observed variance compared to pure Poisson statistics [24]. The contribution W_D to the FWHM of the γ-spectra in germanium detectors amounts to

$$W_D^2 = 8 \cdot \ln(2) F \epsilon E \tag{2.4}$$

with $\epsilon = 2.96\mathrm{eV}$ [16], the energy which is needed to create an electron-hole pair, i.e. $\approx 3 \cdot 10^5$ electron-hole pairs are created by a $1\mathrm{MeV}$ γ-ray. E is the γ-ray energy.

The incomplete charge collection reduces the energy resolution. The factor W_X^2 depends on the electric field strength and on the position of the γ-ray interaction inside the crystal, as the amount of lost charge is proportional to the drift velocity and the drift length of the charge carriers. Highly segmented germanium detectors and pulse shape analysis can be used to determine the interaction position of the γ-ray. The identification of the interaction position allows for a correction of the strongly position-dependent trapping effects for the first time in these detectors. Therefore, a significant improvement of the energy resolution can be achieved by a correction procedure as described in chapter 6.

The third summand on the right side of the equation W_E describes the effects coming from the noise generated by the detector-preamplifier compound. The main contribution here is the noise from the field effect transistor (FET) which is part of the very first feedback loop of the preamplifier. Operating these FETs close to liquid nitrogen temperature reduces their thermal noise significantly. If a considerable amount of electrons gets thermally excited, the noise from this so-called leakage current appears also in this term. In normal operation close to liquid nitrogen temperature, this current amounts to a few pA and is negligible. The combination of the individually measured signals at the cathode and anode on an event by event basis clearly increases the signal-to-noise ratio. This procedure is applied and described in chapter 5.

In total, the dependencies of the energy resolution are as follows: $W_T = \sqrt{a \cdot E + b \cdot E^2 + c}$. The first summand rises proportionally to $\sqrt{E}$, i.e. $\sqrt{N}$ as it depends on the variance of the created electron-hole pairs. The trapping contribution is correlated linearly with the energy while the electronic noise does not depend on the γ-ray energy. Electronic noise is the largest contribution at low energies. The first constant is $a = \sqrt{8 \cdot \ln(2) F \epsilon}$ and depends on the Fano factor. The other two constants are determined by a fit to measured values in chapter 5, where also the relative importance of the noise contributions to the overall energy resolution is documented.

An improvement of the energy resolution can be achieved by optimizing the electronic noise contribution and by reducing trapping effects via correction in position-sensitive detectors. The independent measurement of the cathode and the anode signals reduces the contribution of W_D through the signal averaging because their electronic noise is statistically uncorrelated.

Chapter 3

The AGATA triple cluster detector and its assembly

The AGATA spectrometer will comprise 180 asymmetric 36-fold segmented, hexagonally shaped, encapsulated, tapered high purity germanium detectors. Three slightly different asymmetric crystal shapes are used and combined in triple cluster detectors, i.e. 60 ATC detectors will be used in the final array. In order to maximize the solid angle coverage, the spherical surface is tiled with the projection of the same pattern drawn on each of the faces of an enclosed regular polyhedron. The final AGATA configuration is obtained by the decomposition of a truncated icosahedron with 12 pentagons and 20 hexagons to a surface with 12 pentagons and 180 hexagons. For a maximum size of the crystals, this geometry allows an efficient use of the valuable Ge crystal. The detector configuration allows for a $9\,\mathrm{cm}$ thick germanium shell with up to $82\,\%$ of solid angle coverage. This configuration was selected on the basis of its modularity and symmetry as well as for its inner radius of $23.5\,\mathrm{cm}$, which allows for the use of various ancillary detectors.

3.1 The AGATA crystals

The detectors are produced by the company Canberra in Lingolsheim (Strasbourg), France. The three types of detectors used in one AGATA triple cryostat are built out of 36-fold segmented, coaxial HPGe crystals (see figure 3.1). The different detector shapes are assigned an alphanumeric and a color code: A/red, B/green and C/blue. The crystals of the three geometries have a length of $90 \pm 1\,\mathrm{mm}$ and a diameter of $80^{+0.7}_{-0.1}\mathrm{mm}$ at the back. In the front, they are tapered to an irregular hexagonal shape with a tapering angle of $8\,^{\circ}$. The crystal's central hole has a diameter of $10\,\mathrm{mm}$ and extends to $13\,\mathrm{mm}$ from the front end. The sixfold sector-wise segmentation forms rings of 8, 13, 15, 18,18, and $18\,\mathrm{mm}$ starting from the hexagonal front face of the detector (see figure 3.2). Longitudinal segmentation lines are in the middle of the narrowing external faces. Monte Carlo simulations were carried out in order to optimize the size

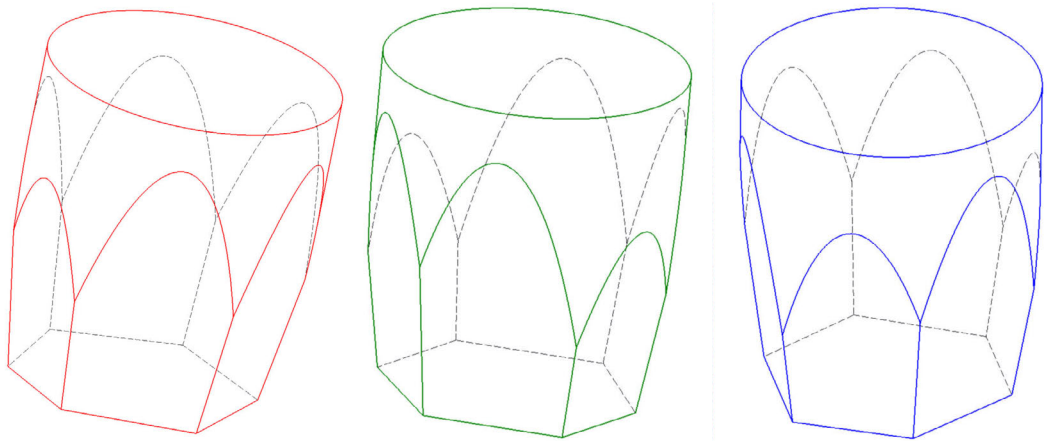

Figure 3.1: Drawing of the three different crystal geometries. All ATC detectors combine the three different crystal shapes. The color code complies with the AGATA labeling convention.

of the individual segments. The width of the rings have been optimized by GEANT4 calculations for uniform distribution of the γ ray interactions and for optimal pulse-shape sensitivity [25, 26]. The AGATA labeling convention assigns the letters A-F to the six sectors around the detector axis, while the numbers 1-6 are used in conjunction with the six rings. The front ring is assigned the number one, followed one by one by the remaining five rings (see Fig.3.2).

A picture of the bare Ge crystal is shown in figure 3.3(a). The typical weight of a Ge crystal amounts to about $2\,\mathrm{kg}$. All crystals are made of n-type HPGe material. The impurity concentration is specified to be between 0.4 and $1.8 \times 10^{10}\mathrm{cm}^{-3}$. The surfaces of these crystals are very delicate. To facilitate the handling without clean room conditions, each crystal is encapsulated and hermetically sealed into an Al canister with $0.8\,\mathrm{mm}$ wall thickness. The encapsulation technology [7] was initially developed for the EUROBALL cluster detectors. The distance between capsule walls and crystal side faces is $0.4-0.7\mathrm{mm}$. The 6×7 connector feed-throughs provide access to each of the 36 segmented outer contacts. They are grouped per sector (Fig. 3.3(b)). The core contact, which is used to apply the high voltage and to obtain the core energy signal, is isolated with ceramic.

A two-layered printed circuit board (Fig. 3.3(c)) is mounted in proximity to the segment feed throughs and acts as an interface for the cold part of the preamplifier electronics. The board allows to connect and dismount detectors from the cryostat in a fast way.

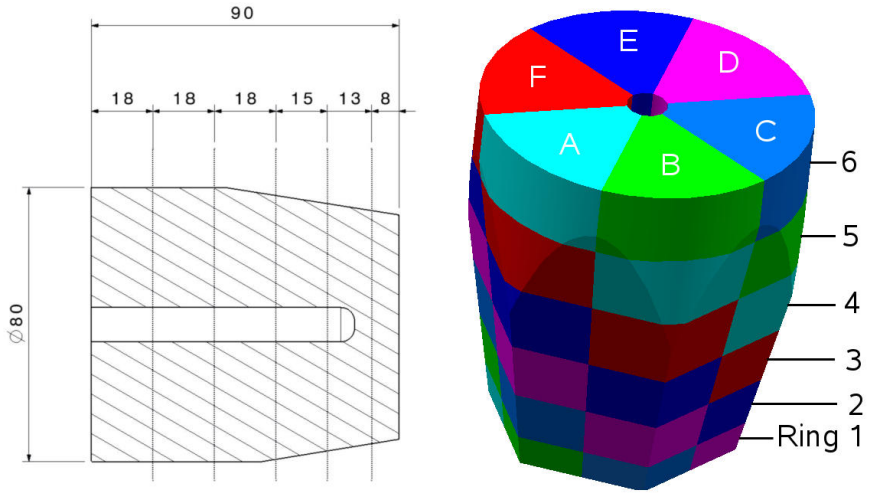

Figure 3.2: Drawing of the dimensions for the crystal and its segmentation with the segment labeling in the right picture.

(a) Unsegmented crystal (b) Encapsulated crystal (c) Detector with PCB

Figure 3.3: Processing steps of the AGATA detector from the bare Ge-crystal to an encapsulated detector with a PCB for cold preamplifier components.

3.2 The AGATA triple cryostats

The hardware of the AGATA triple cryostats is manufactured by the company CTT in Montabaur, Germany. The preamplifiers are provided by the three electronic groups of the AGATA collaboration from GANIL, France, the University of Milano and the IKP, Cologne. Each ATC is housing three crystals, each of a different asymmetry kind. The first triple cryostats were assembled and successfully commissioned in a common effort by CTT and the AGATA detector working group at IKP Cologne.

A closed AGATA triple cryostat is shown in figure 3.4. The end cap is rendered semi-transparent to show the alignment of the detectors relative to the end cap. The picture demonstrates one of the challenges in the design and assembly of such a detector with the high signal density inside the cold part of the cryostat. Furthermore, the signal-to-noise ratio is minimal when operating the FETs close to liquid nitrogen temperature. The FETs are hidden behind the aluminum colored plane, between the capsules and the signal wires. These signals of the FETs are fed out into the warm part of the cryostat. One triple cryostat comprises 111 individual high resolution spectroscopy channels. Details on the cryostat and its properties can be found in [27].

3.3 The AGATA preamplifiers

A tiny amount of charge carriers is produced inside the Ge crystal after interactions of incident γ-ray events and then collected on the two different detector electrodes. The purpose of the preamplifier is to convert these small signals into voltage pulses that are large enough to be handled by the subsequent electronics. The preamplifiers for the AGATA detectors require, besides the traditional good energy and timing properties, also fast and clean transfer functions to register unperturbed signal traces for the pulse shape analysis. In addition, a high counting rate capability is demanded in order to fully exploit the high geometrical efficiency.

New preamplifiers have been developed for AGATA by a collaboration of GANIL, the University of Milan, and the University of Cologne which fulfill these requirements [28, 29, 30]. The segment and the core signals of the AGATA detectors are read out simultaneously through advanced charge-sensitive, resistive feedback preamplifiers employing a new fast reset technology for dead time and dynamic range optimization as well as an original circuit structure for maximizing the open-loop gain of the charge-sensing stage.

The preamplifier structure is divided into a cold and a warm part as the signal to noise ratio is improved by operating the field effect transistors (FET) at about $130 \pm 20\mathrm{K}$ in close proximity to the detector electrodes using the cryogenic cooling of the crystal with liquid nitrogen. This FET, together with an RC component ($1.0\,\mathrm{pF}$ feedback capacitance and $1\,\mathrm{G}\Omega$ feedback resistance), composes the cold part of the preamplifier. These signals of the FETs are connected and sent via feed-throughs into the warm part of the cryostat for each signal individually. Additionally, the feedback

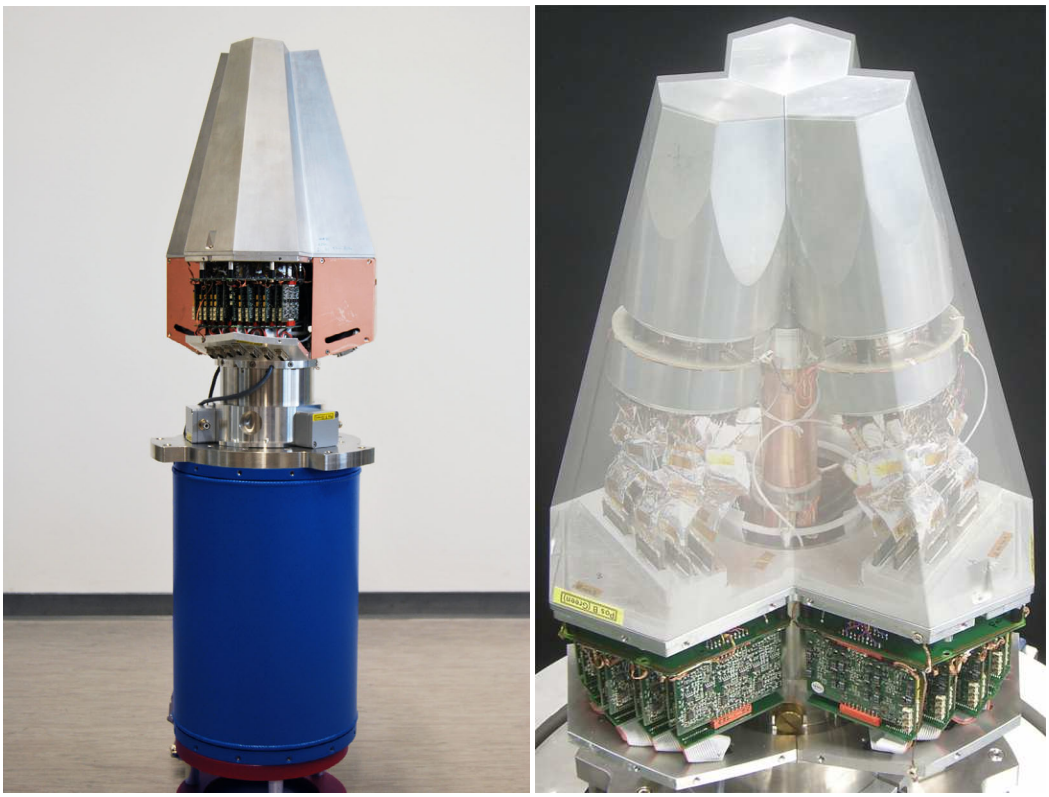

Figure 3.4: Pictures of the ATC detector. (a) The copper shielding is partially removed to reveal the preamplifier housing. (b) ATC with transparent end cap. The picture was graphically edited to show the alignment of the detectors relative to the end cap and the high signal density inside the cold part of the cryostat.

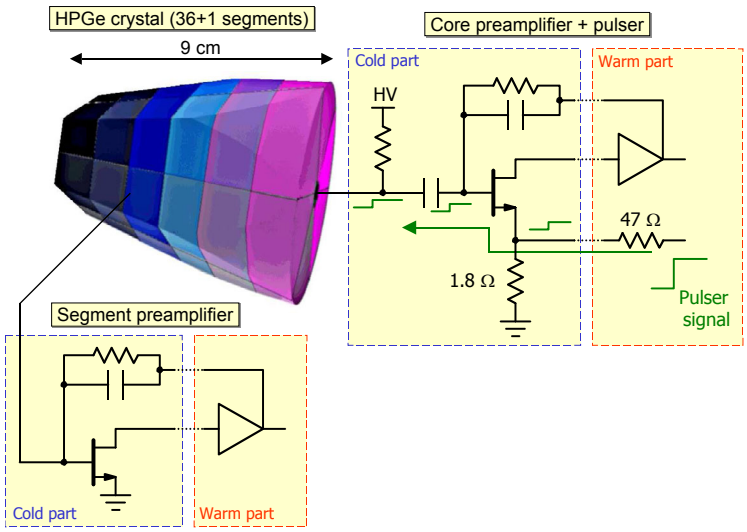

Figure 3.5: Schematic of detector and electronics compound.The core signal is AC coupled while the segments are DC coupled. The signal path from the built-in pulser to the segments passes by a $1.8\,\Omega$ resistor installed in the cryostat, the source of the FET of the core preamplifier, the high voltage decoupling capacitor, and the detector bulk capacitance.

signals are connected via feed-throughs and the feedback RC-circuit in the cold part is connected to the gates of the FETs. The warm part is operated at room temperature and is located close to the cold part of the cryostat. It comprises a low noise transimpedance amplifier, a pole-zero stage, a differential output buffer, and a fast-reset circuitry (see Fig. 3.5 and 3.6 for photographs of the preamplifiers). The purpose of a preamplifier's second stage, the passive pole-zero cancellation network, is to reduce the decay time of the signal to approximately $50\,\mu$s. A relatively short restoration time of the baseline allows for high counting rates of up to $30k$ counts per second in the detector. A differential signal output of the preamplifiers is chosen for an advanced rejection of noise and of disturbances that are picked up along the output cable.

The core preamplifier board also comprises a programmable high-precision pulser, which is used to inject calibration pulses to the core electrode itself as well as to all segment electrodes through the detector bulk capacitance. A detailed description of the newly developed segment preamplifiers is found in references [28, 29, 30]. The main properties are listed in table 3.1. The preamplifiers are the only remaining analog electronics part in the whole electronic instrumentation of the AGATA array. The preamplifier signals are converted into digitial information as soon as possible in order to preserve precision and nativeness of the signal and to have a high flexibility for the signal analysis.

Property	Value	Tolerance
Conversion gain for segments and single core	$100\,\mathrm{mV/MeV}$ (terminated)	$\pm 10\%$
Conversion gain for dual core	$175\,\mathrm{mV/MeV}$ (Core Ch. 1)	$\pm 20\%$
	$50\,\mathrm{mV/MeV}$ (Core Ch. 2)	$\pm 5\%$
Noise	$0.6\,\mathrm{keV}$ FWHM for $0\,\mathrm{pF}$	
Noise slope	$< 10\mathrm{eV/pF}$	
Rise time	$13\mathrm{ns}$ (0pF)	$\pm 2\mathrm{ns}$
Rise time slope	$\sim 0.2\mathrm{ns/pF}$	
Decay time	$45\,\mu\mathrm{s}$	$\pm 2\%$
Output polarity	Differential, $Z = 100\Omega$	
Fast reset speed	$\sim 10\mathrm{MeV}/\mu\mathrm{s}$	
Power supply	$\pm 6\mathrm{V}$, $\pm 12\mathrm{V}$	
Power consumption of input FET	$< 20\mathrm{mW}$	
Power consumption	$< 350\mathrm{mW}$single core & segments	
	($\leq 840\mathrm{mW}$ dual core)	
Mechanical dimension	$< 70\mathrm{mm} \times 50\mathrm{mm} \times 7\mathrm{mm}$	

Table 3.1: Specifications of the AGATA preamplifiers.

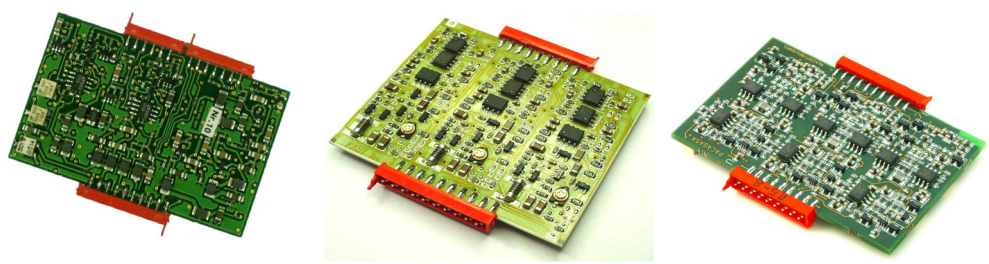

(a) Dual gain core preamplifier (b) Milan triple segment preamplifier (c) GANIL triple segment preamplifier

Figure 3.6: Photographs of AGATA preamplifiers: (a) Cologne core preamplifier with two different gains and a built-in pulser, (b) Milano segment preamplifier for three detector signals and (c) GANIL triple segment preamplifier.

3.4 Assembly and adjustment of the ATC detector

The AGATA Triple Cluster detector combines for the first time highly segmented HPGe detectors and highly integrated, high bandwidth preamplifiers for pulse shape analysis. The cryostat technology is designed to cope with the high signal integration and the cooling of about $6\,\mathrm{kg}$ of germanium. The newly developed preamplifiers have to provide fast signals with a clean transfer function and a large dynamic range. These new detector components were assembled for the first time as part of the research for the present thesis in collaboration with H. Hess. Several problems with the analog electronic part were subject of detailed investigations.

Electronic noise is to a certain level unpreventable in a HPGe detector. All measures have to be taken in order to avoid any additional noise components. Beside noise also periodic disturbances in every frequency range from acoustic frequencies up to GHz high frequency oscillations affect the energy resolution and the position resolution. Therefore, the major tasks during the ATC detector assembly were to acquire a proper understanding of electronic properties, low noise conditions and the elimination of unwanted and spurious electronic high frequency disturbances.

A large bandwidth of the AGATA preamplifier is required for a good position resolution by the pulse shape analysis. Signal rise times of about $30\,\mathrm{ns}$ are related to a bandwidth of $10\,\mathrm{MHz}$. But the large bandwidth allows for a large range of noise frequencies to disturb the system. Furthermore, if the rise time is faster than the settling-time of the signal, the preamplifier is at risk of producing high frequency oscillations. This effect is demonstrated in subsection 3.4.4.

The cryostat technology limits the diameter of grounding wires which are needed to assure a solid ground connection between the cold and the warm part due to thermal conductivity. A solid ground connection is needed for a good signal integrity, especially for the high amount of channels. Variations of the electric potential have to be as small as possible, even for highest occurring currents. Therefore, a compromise solution has to be found between a good enough electrical conductivity with high thermal losses and a small thermal conductivity from the cold to the warm part of the cryostat which provides enough conductivity for a proper electrical grounding.

A precise analytical description of the whole electronic network of the detector could not be provided by the electronic engineers due to the hundreds of contacts and electrical connections with limited wire cross-section in the cold part of the cryostat. Therefore, a phenomenological approach is chosen to identify the sources of oscillations and of potential weaknesses. The aim of this study was to ensure reproducible immunity to high frequency oscillations in the new AGATA detectors.

3.4.1 Fast Fourier Transformation

The Fast Fourier Transformation (FFT) has shown to be a very useful tool. It reveals the relative strengths of any frequency component of the signal in the frequency domain. The FFT is an efficient algorithm using the Discrete Fourier Transformation

(DFT) to transform a continuous signal in the time domain into a discrete spectrum in the frequency domain. The DFT is expressed by

$$F_m = \Sigma_{n=0}^{N-1} f_n \cdot e^{-j \cdot 2\pi mn/N}$$

with the time domain sequence f_n in the range of N elements resulting in the frequency domain sequence F_m. The redundance of the DFT sum elements allows for the reduction of the number of computations needed for N points from $2N^2$ to $2N \log N$ [31].

The Fast Fourier Transform spectra were measured with different analyzers at different laboratories where the measurement took place. At IKP, an analog Hewlett Packard spectrum analyzer 8590L with a wide sensitive region between $9\,\mathrm{kHz}$ and $1.8\,\mathrm{GHz}$ is used to analyze the Fourier spectra. Furthermore, the above-mentioned LeCroy oscilloscope is also used for calculating the FFT with its $400\,\mathrm{MHz}$ sampling rate. The FFT spectra in Legnaro were recorded with $100\,\mathrm{MHz}$ sampling rate digitizers, which were developed by the AGATA community. A detailed description of the digitizers is found in the technical design report [11].

3.4.2 Noise and high frequency effects

The noise of high frequency (HF) disturbances corrupts the energy resolution and the position resolution of HPGe detectors. Depending on the HF level and on the frequency range, the resulting detector noise level mainly affects either the energy resolution or the PSA. While frequencies $< 1\,\mathrm{MHz}$ are deteriorating the energy resolution, higher frequencies make PSA more difficult and decrease the position resolution.

The effect of the noise on the energy resolution can be seen in the frequency domain. The core signals of detector B003 in ATC2 were recorded with a digital $400\,\mathrm{MHz}$ LeCroy oscilloscope [32]. The Fast Fourier spectra in the frequency domain were calculated with the same device for the detector signals acquired at different bias voltages. Figure 3.7 illustrates how the noise plateau, which influences the energy resolution, in the frequency spectrum is changing with the applied bias voltage. The bulk capacitance of the detector changes with the applied bias voltage. The detector capacitance is decreased with increasing high voltage until the full depletion of the crystal is reached. The noise of the charge-sensitive preamplifier is proportional to the capacitance at the input of the preamplifier. The figure 3.7 shows the noise reduction in the noise plateau in the frequency region of 10^5 up to 10^6Hz, responsible for the energy resolution. This frequency also corresponds to the shaping times of analog amplifiers or digital trapezoidal filters between 1 and $10\,\mu\mathrm{s}$, where the signals are not filtered at all. The signal-to-noise ratio is clearly improved, while the high voltage is increased. Also the rise time depends on the preamplifier input capacitance. Therefore, a change in the bandwidth is observed for the various bias voltages. As the descending slope at high frequencies is shifted to a lower frequency for the smallest bias voltage of $500\,\mathrm{V}$, the rise time is obviously decreased with an increasing preamplifier input capacitance.

The large bandwidth of the preamplifier allows not only for fast net and transient signals to remain unfiltered, but also for unfiltered high frequency disturbances. The

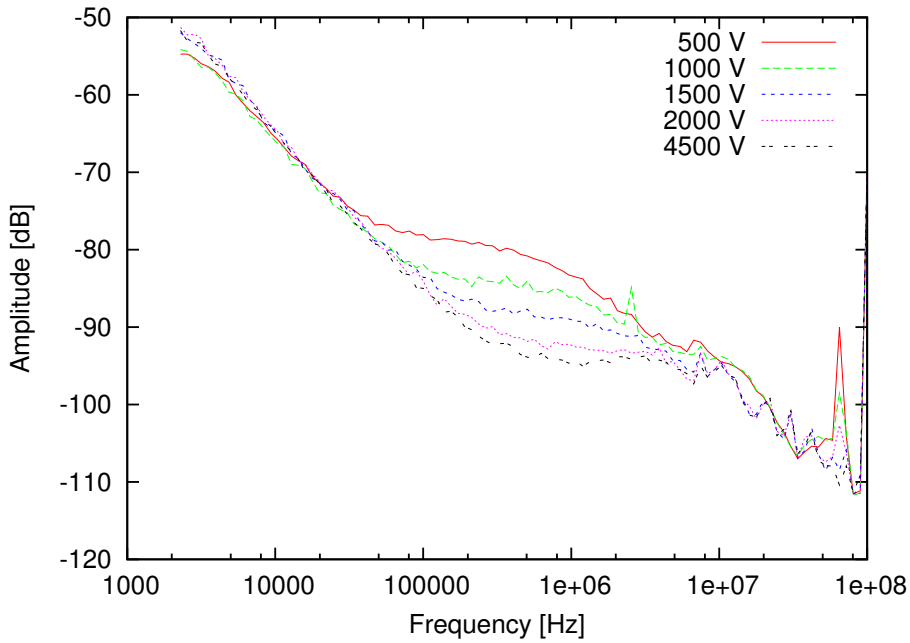

Figure 3.7: The relative strength of the frequency components is shown in the FFT spectra for different bias voltages on the core signal of detector B003 in ATC2.

spurious spikes above $5\mathrm{MHz}$ affect the position resolution. A superposition of the signals and the noise takes place if they occur at the same time. This effect is even more relevant for the superposition of the tiny transient signals with the noise because of the smaller signal-to-noise ratio of the transients. The equivalent frequency of the signal rise times between about 100 and $300\,\mathrm{ns}$ is in the low MHz-region. The similarity of the frequencies of the signals and the disturbances is the reason for the decline of the position resolution due to MHz-disturbances.

3.4.3 Baseline oscillations

The study of the oscillations and the disturbances was first performed at IKP on the second ATC detector. Some detectors showed instability against HF oscillation which deteriorated the energy and the position resolution. These oscillations appeared at various frequencies which are listed below, sometimes with peak-to-peak amplitudes of a few V in the time domain.

HF disturbances are best investigated in the frequency domain. FFT spectra are shown in figure 3.7 for different bias voltages. The x-axis is displayed logarithmically to show the entire frequency region in a Bode-like diagram. Linear x scaling can be used to study the highest frequencies in the bandwidth of the preamplifier. An example is shown in figure 3.8, where a screen shot of the digital LeCroy oscilloscope is presented. The top of the plot shows the signal in the time domain. The corresponding frequency domain spectrum is presented below with a linear display of the x-axis.

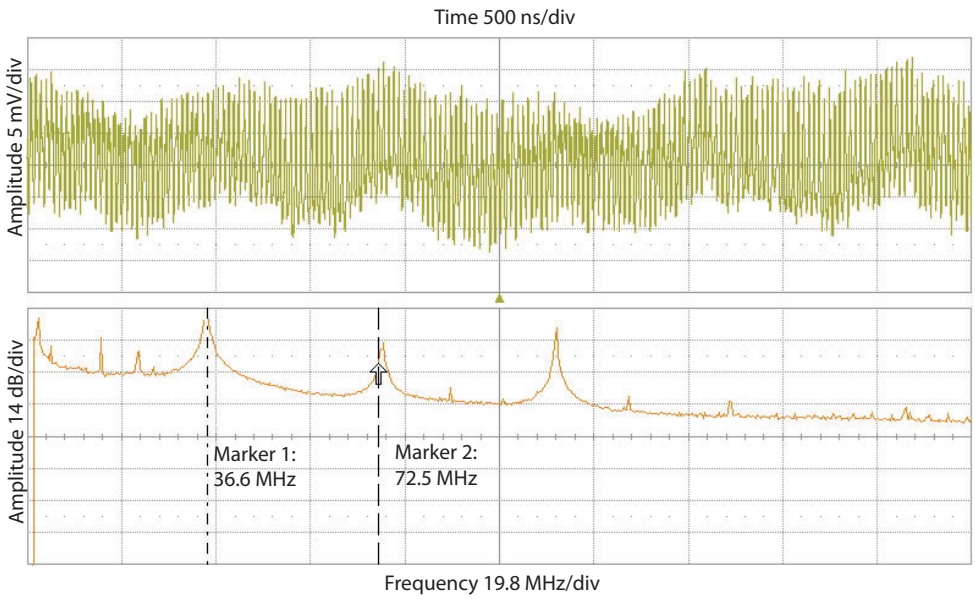

Figure 3.8: Oscillations of 20, 36.5, 73, 110 MHz shown in time (top) and frequency domain (bottom). In the time base the peak to peak noise amounts to $25\mathrm{mV}$ instead of $4\mathrm{mV}$ with a clean signal.

A spectrum was measured with the DGF 4C Rev. E digital electronics, where the signal was clean at the beginning of the measurement. During the measurement an oscillation with a frequency of $40\,\mathrm{MHz}$ appeared. Figure 3.9 shows the corresponding detector signal γ-ray spectrum for an energy of $1.33\mathrm{MeV}$. A shift of the measured energy to lower values is observed as well as a broadening of the peak due to the oscillation. This behavior demonstrates the harmful effect of the HF on the detector spectra. This effect is not acceptable and needs to be avoided by assuring stability against HF oscillations.

The observed oscillations can be divided into 4 categories:

- Low frequency oscillations $< 10\mathrm{kHz}$: Microphonic baseline oscillation with a frequency of around $1\,\mathrm{Hz}$ worsens the energy resolution (see Fig. 3.10),
- 1 - $20\mathrm{MHz}$ oscillation usually caused by the grounding in the cold part,
- 20 - $80\mathrm{MHz}$ (see figure 3.8),
- $> 80\mathrm{MHz}$.

Low frequency baseline oscillation is caused by the microphonic effect, which is related to change in capacitance between high voltage and the ground level. The

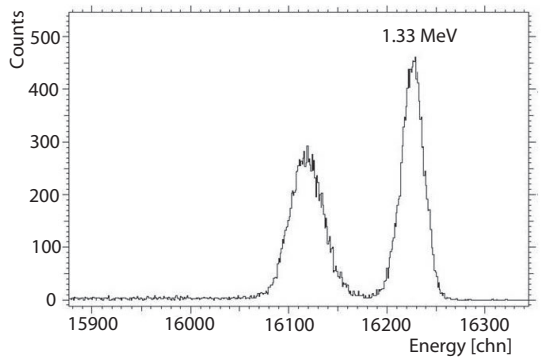

Figure 3.9: The spectrum shows the $1.33\,\mathrm{MeV}$ line recorded without oscillation (right peak) and the peak that was shifted to lower energy after the oscillation of $40\,\mathrm{MHz}$ occurred. The peak is not only shifted but also broadened due to the oscillation. This behavior demonstrates the harmful effect of the HF on the detector spectra.

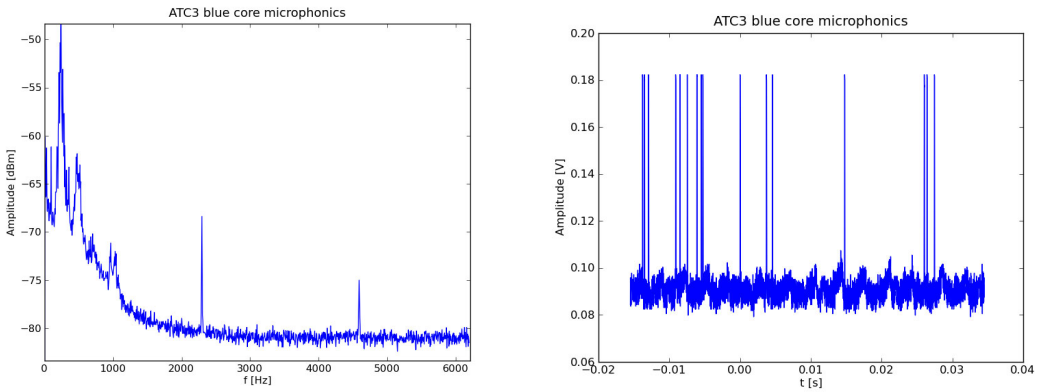

Figure 3.10: Microphonic oscillation of baseline in frequency (left) and time domain (right) on the analog main amplifier (ORTEC 572) signal.

lowest of the three high frequency oscillation areas, between 1 - $20\mathrm{MHz}$, is caused by insufficient grounding in the cold part of the cryostat and was removed by optimizing this part of the detector. This part will be described in [27].

Furthermore, frequency oscillations of 80 - $120\mathrm{MHz}$ were observed. These oscillations in the FM broadcasting frequency region are picked up by the ribbon MDR cable connecting the detector preamplifiers with the converter of the differential signals to single ended signals. Frequencies in this region are not crucial for the detector performance due to the Nyquist filter of the digital electronics. For the AGATA digitizer with a $100\,\mathrm{MHz}$ sampling rate, the Nyquist frequency is $50\,\mathrm{MHz}$. According to the Nyquist theorem, the sampling rate has to be twice as large as the highest frequency in the frequency domain. Only lower frequencies than half of the sampling rate were fully reconstructed and remained relevant for the energy resolution. Moreover, the high frequencies above the Nyquist frequency of the AGATA digitizers were not very dominant and could only be observed with the Hewlett Packard spectrum analyzer 8590L and the digital LeCroy oscilloscope. An improved MDR cable is needed to remove this HF contribution.

3.4.4 Preamplifier rise times

Preamplifiers are prone to oscillations at high bandwidth. The rise time is an important quantity to check the bandwidth of the new preamplifiers after delivery. Milan preamplifiers are specified for rise times higher than $28\,\mathrm{ns}$ and GANIL preamplifiers for more than $30\,\mathrm{ns}$. After delivery and prior to installation, preamplifiers with rise times of down to $15\,\mathrm{ns}$ were measured. The rise time of the preamplifiers is a strong indicator for potential HF problems and for distortion of the signal. Therefore, the rise times for all 111 preamplifier channels were checked and often corrected. Preamplifiers which are too fast show an overshoot (see Fig. 3.12 (a)). On the other hand, a short rise time is desirable for unperturbed signals for the pulse shape analysis.

A special capacitance network was built to simulate detector capacitances, and to test preamplifier properties without a detector by injecting a fast rectangular pulser signal with a rise time of $1\,\mathrm{ns}$. The capacitance arising from the geometry of the electrodes and the bulk material as dielectrics for the six segments was replaced by a capacitance of $1\,\mathrm{pF}$ (red capacitors in Fig. 3.11), while the crystal to aluminum capsule was represented by $20\,\mathrm{pF}$ capacitors (yellow). Additionally, a $50\,\Omega$ terminal resistance was used. The rise time of the preamplifier and the rise time of the pulser add quadratically. Therefore, a relatively fast pulser, compared to the rise time of the preamplifier, was used. As a solution of the problem, additional capacitors between 4.0 and $18.0 \pm 0.5\,\mathrm{pF}$ were added on the preamplifiers to slow down their rise time. To achieve this, the collector and the emitter of an inverting transistor on the preamplifier board were connected via a capacitance for a negative feedback [33]. In this way the rise time was effectively reduced. In figure 3.12, the effect of the correction procedure is demonstrated. In (a), a signal with $20\,\mathrm{ns}$ $10-90\%$ rise time and a 5.9% overshoot is shown, while in (b), an ideal signal with $38\,\mathrm{ns}$ and no overshoot is displayed. More

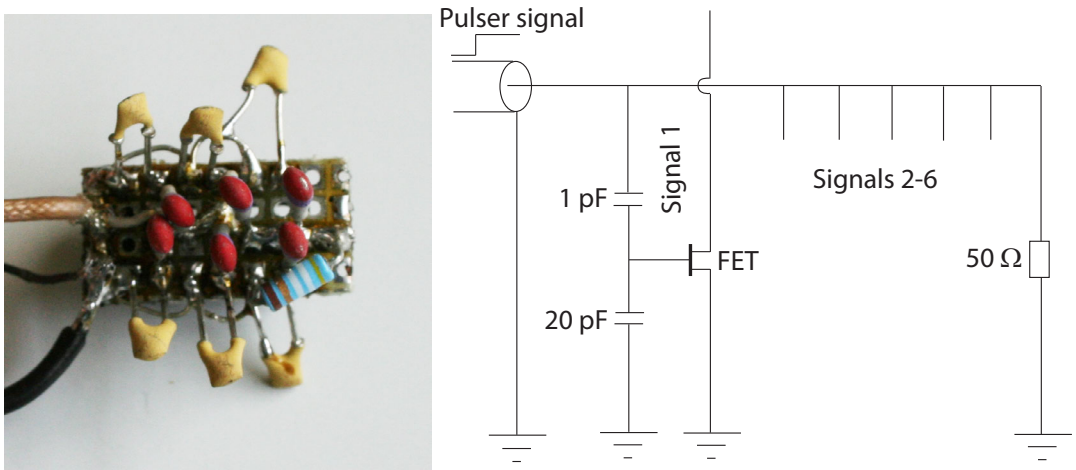

Figure 3.11: Capacitance network simulating detector capacitors for tests of preamplifier rise times.

overshoot may appear as ringing at the beginning and at the top of the pulse. The so-called settling-time is longer than the rise time of the signal. This behavior has to be avoided. The settling-time is the time before the signal reaches the final value and stays there [34].

Increasing the rise time, respectively reducing the bandwidth of the preamplifier with an increased integration capacitor improves the signal-to-noise ratio, assures a flat amplitude response, and damps the oscillation. The actual configuration of the Milan segment preamplifiers with at least $28\,\mathrm{ns}$ rise time and the GANIL segment preamplifiers as well as the Cologne core preamplifiers with at least $30\,\mathrm{ns}$ rise time turned out to be a feasible solution without signal distortions and with minimum loss in bandwidth. For the detector ATC2, rise times between 18 and $28\,\mathrm{ns}$ were found for the GANIL and 20 to $29\,\mathrm{ns}$ for the Milan preamplifiers at room temperature. The real values at liquid nitrogen temperature are even $20\,\%$ lower because the FETs are not operated at liquid nitrogen temperature in these tests. Cold FETs show a $20\,\%$ lower rise time, which needs to be taken into account during tuning of the rise times. The signals were acquired with a digital $400\,\mathrm{MHz}$ LeCroy oscilloscope. Adding $6.8 \pm 0.5\,\mathrm{pF}$ capacitors increased the rise times to $36 - 46\,\mathrm{ns}$ for the GANIL, respectively to $36 - 45\,\mathrm{ns}$ for the Milan preamplifiers. A good signal-to-noise ratio is provided after the rise time adjustment together with sufficient rise time for unperturbed detector signals, consistent with the pulse response requirement.

Several preamplifiers showed high frequency oscillations only related to the first of the three channels between 4 and $18\,\mathrm{MHz}$ when mounted with at least one adjacent preamplifier. The FFT spectrum is shown as an example for one channel in figure 3.13. The source for the problem was the voltage regulator resistance of the $-12\,\mathrm{V}$ power supply. The regulated voltage of $-11.6\mathrm{V}$ is too close to the voltage of the power supply. Setting the regulated voltage at $-10.8\mathrm{V}$ solved the problem [35]. The

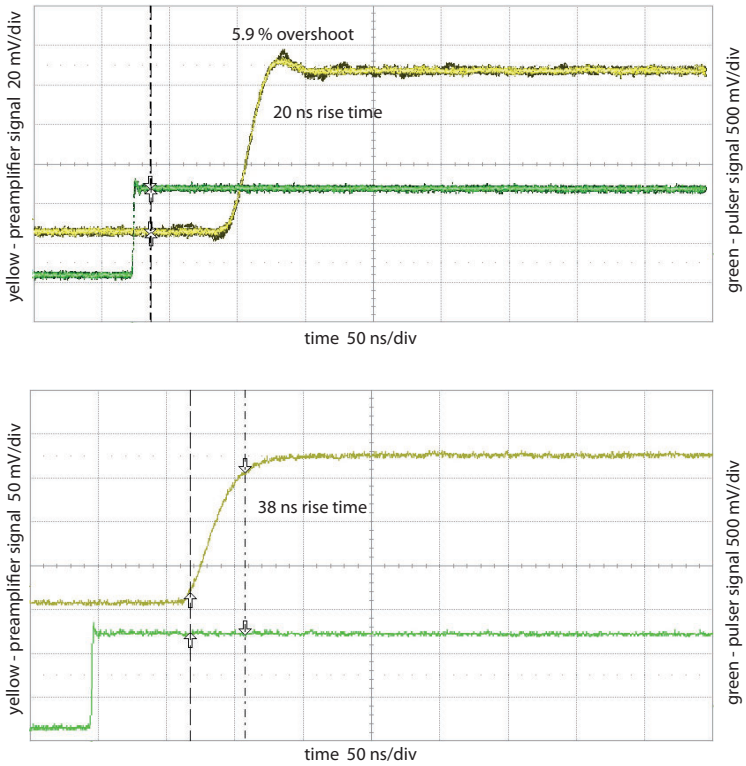

Figure 3.12: Preamplifier response with too fast rise time of a preamplifier (a) and a rise time in agreement with specification (b) in yellow. The pulser signal is represented by the green signal.

tests were performed on the symmetric prototype detector S001 in a single cryostat. After this correction all preamplifiers showed clean FFT spectra (like in figure 3.13 (b)) afterwards.

3.4.5 High frequencies 20 - 80 MHz

High frequency oscillations between 20 and $80\mathrm{MHz}$ with very strong and pronounced sine waves caused the most severe and persistent HF challenge during the assembly phase. The peak-to-peak amplitude of the oscillation on the core preamplifier signals amounted to unacceptable amplitudes of $200\mathrm{mV}$ to $500\mathrm{mV}$. High frequency oscillations in this frequency region deteriorate the pulse shape analysis and the large amplitudes affect the energy resolution.

The oscillation also appeared on all segments but with half the amplitude of the core oscillation. The frequency changed between 34, 40, 52, and $73\mathrm{MHz}$ for no obvious reason. A phase shift between the core signals of the three detectors was observed: A & C show a phase shift of $180°$ relative to the core signal of detector B. Another observation showed that the oscillation was independent of the applied high voltage. The

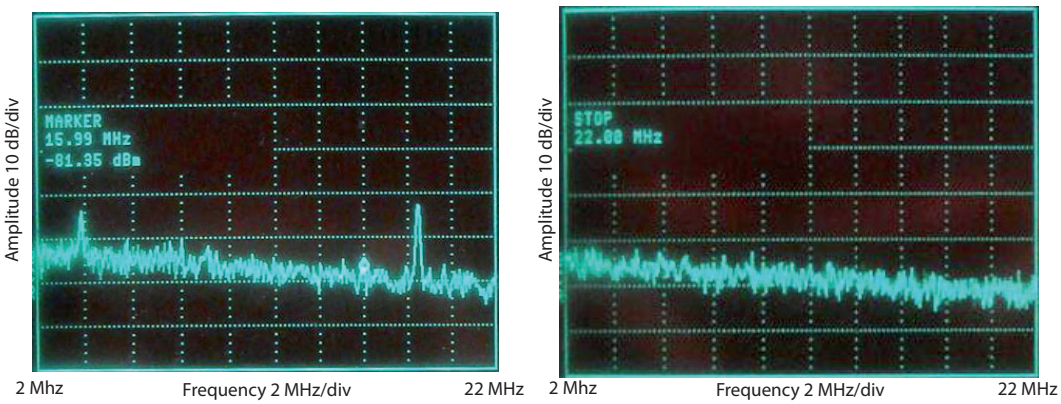

Figure 3.13: FFT spectrum of first the channel of a segment preamplifier before and after modification. The oscillation (left) was removed (right) by modification of the regulation voltage for the $-12\,\mathrm{V}$ power supply.

amount of connected respectively powered detectors was crucial for the stability of the detector. When only two detectors were connected, the HF disappeared independently of the disconnected detector.

Several adjustments and modifications could partly reduce the amplitude of the HF oscillations: (i) the preamplifier rise time was enlarged, (ii) grounding cables in the warm part of the cryostat was enforced, (iii) axial ferrite beads around the cables were applied. A reduction of the observed amplitude was obtained. However, it turned out that the source of the oscillation was not located and removed. The amplitudes could be reduced to a range between $30\mathrm{mV}$ and $60\mathrm{mV}$.

After a longer investigation the source for the high frequency oscillation between 20 and $80\mathrm{MHz}$ could be located in the micro match connector which is attached to the top and to the bottom side of the preamplifier (see Fig. 3.6). The micro match connector connects all incoming or outgoing signals, ground lines, and low voltage power supplies.

This connector was chosen because of the high integration of pins and for the comfortable handling due to the small size of the connector. Unfortunately the tin plated contacts show wear out effects (see Fig. 3.14 (a)). The specification for the connector allows 20 insertions and withdrawals. But the surface tin is removed after only one mating cycle (see figure 3.14 (c)). Additionally, the results of micro-motion are resistance spikes during motion as well as a gradual increase of the contact resistance with an increasing number of motion cycles. The motion at the electrical contact interface causes fretting corrosion which results in a formation of insulating films, such as oxides and organic polymers, on the contact surface [36, 37].

Ten pins per preamplifier, i.e. per micro match connector, are foreseen for the grounding lines of the preamplifier. After fretting corrosion, the individual pins show different contact resistances which create potential differences and hence ground loops.

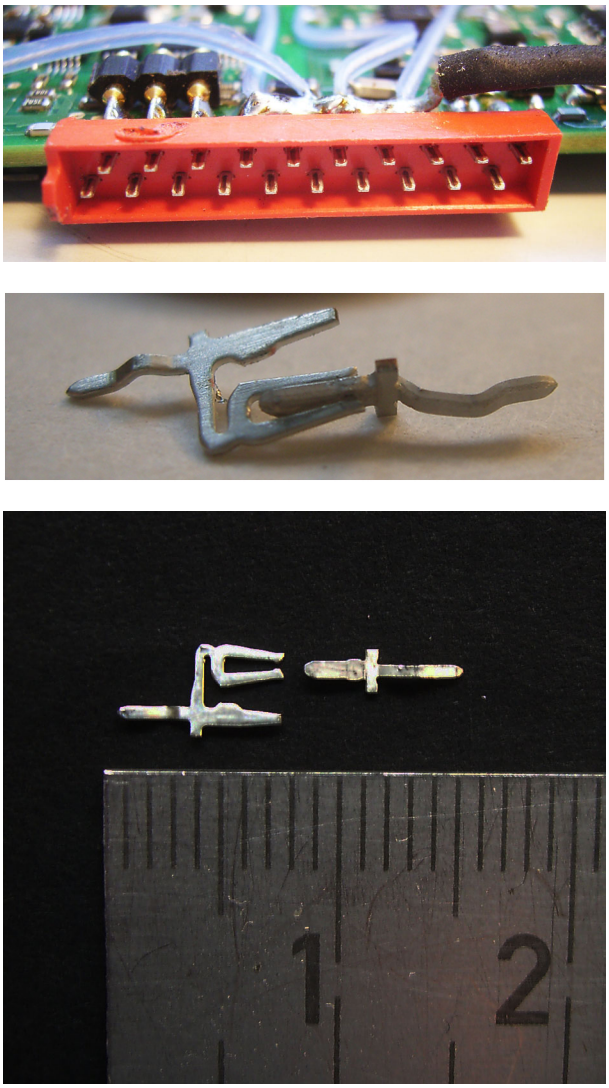

Figure 3.14: Micro match connector showing fretting corrosion on the pins (a), one pin of the connector with the female counterpart connected (b) and after withdrawal the male and the female part after one cycle with graphically increased contrast showing trace of mating (c).

These ground loops cause the observed oscillations. Reducing the system from a multipoint to a singlepoint ground by short-connecting the individual pins with copper braids to one common ground solves the problem (see Fig 3.15 (a)) [38]. After applying the short-connection of the grounding pins, the oscillations between 20 and $80\mathrm{MHz}$ were removed from all the first four ATC detectors and the peak-to-peak noise was reduced to 3 to $4\mathrm{mV}$. The oscillations have not appeared since the four detectors were modified.

A good contact is not only important for the grounding but also for the signal

connections. The female connector part does not enclose the male part, but it only makes contact in two points on both sides of the flat pin (see Fig. 3.14 (b)). Insufficient contacts for segments were observed and identified the micro match connector as the weak point and reason for this persistent HF problem. As a consequence, the PCBs carrying all preamplifiers were redesigned and equipped with Fischer MK 221 Z high-precision sockets which resolved this problem.

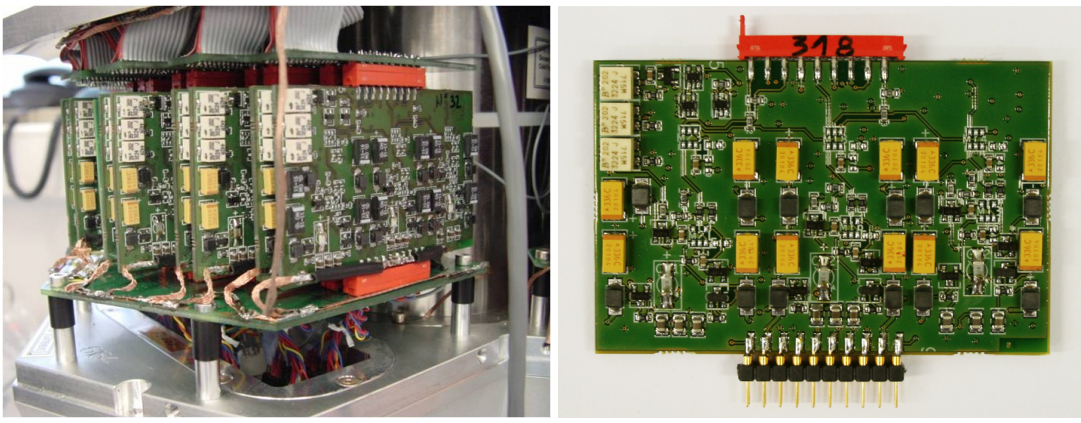

Figure 3.15: Preamplifier housing with micro match connectors short connected (left) and micro match connector replaced by Fischer connector (right).

Modification of PCB for preamplifiers and replacement of connector

The micro match connector on the preamplifiers was replaced by the new Fischer connectors with high-precision contacts of the type MK LP 240 G [39] (see Fig. 3.15 (b)) with gold-plated contacts with a diameter of $0.5\mathrm{mm}$ of the round pins. The female counterpart encloses the pins completely. The exchange of the connector enforced a redesign of the four layer printed circuit board. This modification also gave the opportunity for further improvements on the EMC susceptibility and grounding of the carrier printed circuit board (PCB) for the preamplifiers [40]. In collaboration with the electronics engineers N. Karkour and M. Tripon, several modifications were introduced:

- Increased thickness of the ground layers
- Additional interlayer connections (vias) around the edge of the board
- Removed thermal relief around vias
- Additional copper for electrical contact between screws and grounding
- Additional copper traces between ground pins of all preamplifiers
- Increased thermal relief width to $0.4\,\mathrm{mm}$ for power supply pads

- Additional vias to increase copper connections between the layers for the power supply. A via can act as a fuse in case of high current consumption
- Optimized paths for the power supply inside the PCB

All these points were implemented. As an example the modified top layer of the PCB is shown in figure 3.16 next to the layout with the dimensions of the board and the distribution of the important vias is shown in grey.

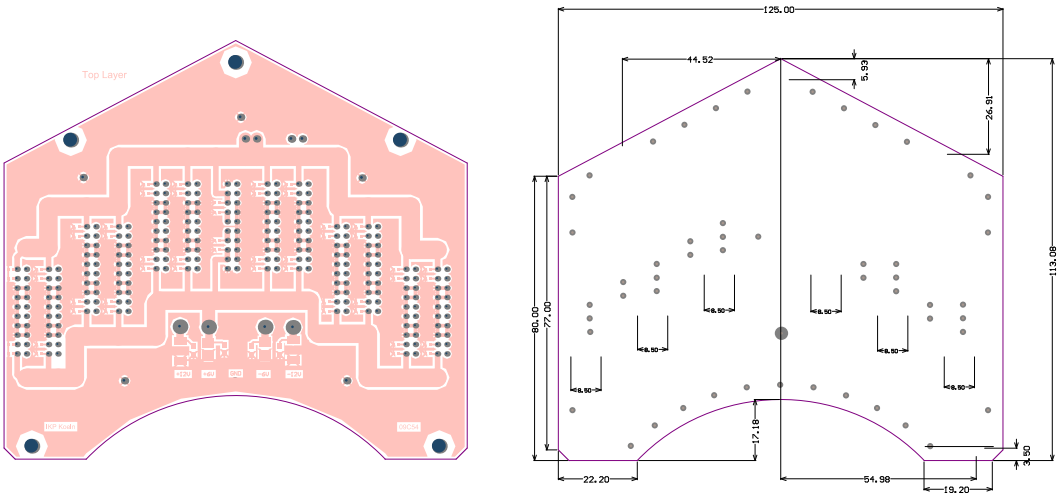

Figure 3.16: Modified carrier PCB for preamplifiers. Top layer of the PCB (left) and dimensions (right).

3.4.6 Test of the detector signal quality

The modified PCB carrying the preamplifiers with Fischer connectors was tested for susceptibility to electromagnetic disturbances at different frequencies together with the electronics engineers N. Karkour and M. Tripon at IKP. The test was performed by directly injecting fast pulses to the grounding or capacitively to the signal cables of the detector. A fast transient burst generator "Schaffner NSG 1025" was used to induce the fast pulses. The response of the signals was analyzed. For direct injection the output of the fast transient pulse generator (FTPG) was connected via a long braid to a ground plane (see Fig. 3.17). Secondly, the output of the FTPG was connected to an aluminum foil surrounding the MDR cable in order to inject the noise charge through a capacitance into the cable shield and hence the ground. The fast transient δ pulse had an amplitude of $1\mathrm{kV}$ and a frequency of $50\mathrm{Hz}$. The response of the signal baseline stayed below the specified value of $10\mathrm{mV}$ (see figure 3.18). With these tests a significant improvement of the performance and the signal integrity was confirmed. The stability and the overall performance of the ATC detector was increased significantly. After the described modifications, the following FWHM values on the cores

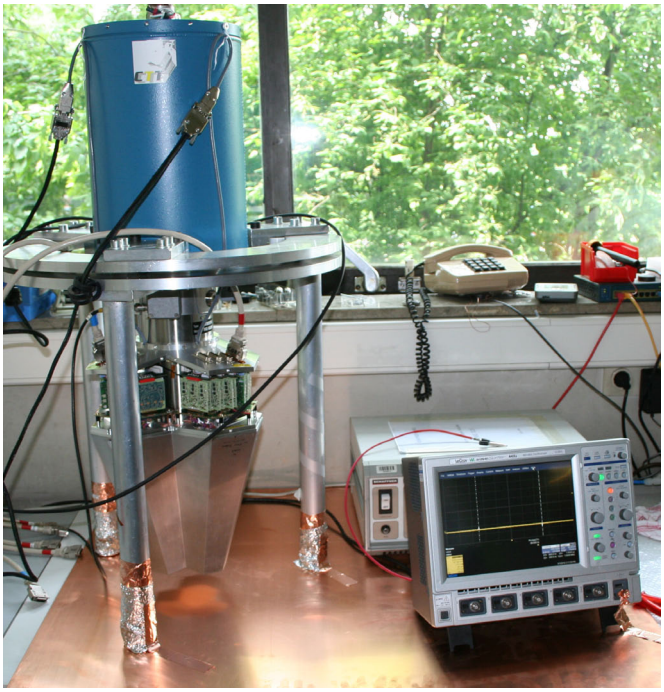

Figure 3.17: Test of susceptibility to electromagnetic disturbances at different frequencies with a fast pulser.

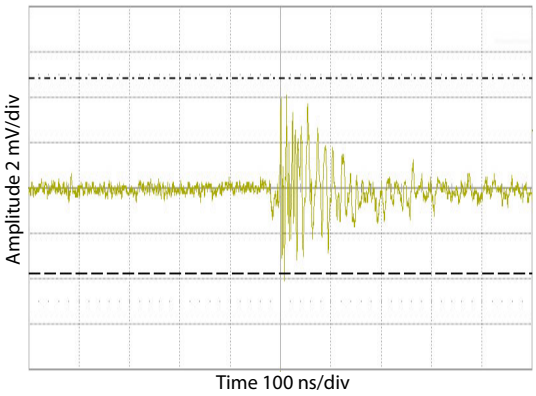

Figure 3.18: Core noise after injection of a fast pulser signal of $1\mathrm{kV}$ amplitude stays well within expected amplitude of $< 10\mathrm{mV}$.

and average values of the segments were measured for the second ATC detector in Cologne before the transport to Legnaro:

Crystal	FWHM [keV] @60keV	FWHM [keV] @ 1.33MeV
Red core	1.16	2.35
Green core	1.26	2.28
Blue core	1.2	2.35
Segment average FWHM [keV] with standard deviation (σ) values		
Red	1.14 $\pm$0.08	2.10 $\pm$0.13
Green	1.06 $\pm$0.07	2.08 $\pm$0.11
Blue	0.97 $\pm$0.06	2.04 $\pm$0.12

Table 3.2: Core FWHM [keV] and segment average FWHM [keV] after modifications.

3.4.7 Mounting the ATC detectors into the final AGATA demonstrator in Legnaro

After the installation of the first ATC detector and the successful modifications of the second ATC in Cologne, the already mounted detector was also modified in the same way as ATC2. All modifications were applied at the same time together. This made a direct comparison of the performance of the unmodified and the improved detector possible. The quality of the detector before and after the modification was compared and is displayed with FFT spectra and energy resolution values. The FFT spectra for the first detector ATC1 in Legnaro were recorded with the $100\,\mathrm{MHz}$ AGATA digitizers and the final data acquisition chain. The FFT spectra were measured right before and after the modifications. The measurement on ATC1 clearly demonstrates the improvement that was reached through the applied modifications (see Fig. 3.19).

The first example shows a frequency spectrum with many HF spikes. Such a spectrum affects the position resolution. The improvement in the energy resolution of $150\mathrm{eV}$ (see Tab. 3.4.7) is also obvious. It is even more strongly pronounced in the second FFT spectrum, where it amounts to $310\mathrm{eV}$. The continuous noise component was significantly reduced. Additionally, the spurious spikes were removed. The only remaining disturbance is the spike at $10\mathrm{MHz}$. The sharp line at $10\mathrm{MHz}$ arises from the beam chopper frequency of the Legnaro accelerator, which is used to create a pulsed beam structure. Similar results were obtained for all four ATC detectors which were assembled as part of this research.

A comparison between the measured energy resolutions before and after the modifications illustrates the final improvements:

A clear improvement of the signal integrity as well as the stability of the performance with immunity to HF oscillations of all ATC detectors was achieved. The modifications in the grounding concept and the exchange of the micro match connector, which were applied to the first detectors, showed reproducible results also with the

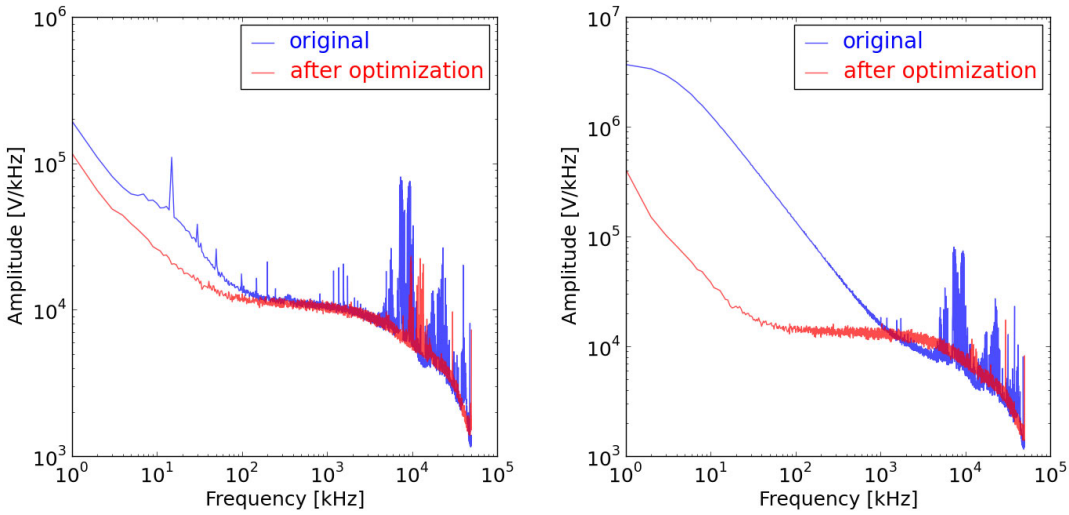

Figure 3.19: FFT spectra of the two crystals A and B in the detector ATC1 measured in Legnaro before and after applying the necessary modifications. On the y axis the amplitude in $\mathrm{V/kHz}$ is plotted for a kHz binning. These FFT spectra represent the performance of all detectors.

Crystal	FWHM [keV] before	FWHM [keV] after modifications
A	2.55	2.4
B	2.59	2.28
C	2.34	2.2

Table 3.3: Core FWHM [keV] before and after applying the modifications.

next two ATC detectors.

Chapter 4

Properties of the ATC detector

In the following chapter, measurements and results with the first four ATC detectors are described. In addition, the results of the customer acceptance tests, which were performed with individual crystals in single cryostats, are included in a comparison between measurements in a single test cryostat and the full ATC detector. The extensive results comprise energy resolution values at different energies and crosstalk contributions for 12 HPGe detectors with 444 individual signals obtained at IKP, Universität zu Köln and at INFN, Legnaro, Italy.

4.1 The single detector test

Before delivery to the AGATA collaboration, each detector is subject to a factory acceptance test carried out by the manufacturer Canberra, France. Upon delivery to the AGATA collaboration, these results and other detector specifications (see table 4.1) had to be verified in a single detector test. These measurements were performed for the first AGATA detectors described in this thesis by the AGATA detector working group at IKP. Several newly developed single test cryostats were put into operation for this purpose. A picture of one single test cryostat is shown in picture 4.1 as an example. The AGATA cryostats are manufactured by the company CTT in Montabaur, Germany [41]. Single cryostats are employed for the single acceptance tests of the crystals and for characterisation of the position-dependent detector pulses within an elaborated scanning program. The cryostats are equipped with 37 cold preamplifier input stages, the same as in the final ATC detectors. These preamplifiers are described in the previous chapter.

The most relevant numbers of the AGATA specifications are given in table 4.1. They are related to core and segment energy resolution values at $E_\gamma = 60\,\mathrm{keV}$ for the segments and at $E_\gamma = 122\,\mathrm{keV}$ for the core at low energy. The performance is also tested at a higher energy of $E_\gamma = 1.33\,\mathrm{MeV}$ on the core and the segments, where an energy resolution below ≤ 2.35 respectively ≤ 2.3 is claimed. The results of the single detector tests are plotted in figures 4.7 and 4.8 with the red dots. They are compared to

Core:		
Source	FWHM	FWTM/FWHM
FWHM for $122\,\mathrm{keV}$ (^{57}Co)	≤ 1.35	≤ 2
FWHM for $1.33\,\mathrm{MeV}$ (^{60}Co)	≤ 2.35	≤ 2
Measurement conditions: The source is positioned in front of the detector. Count rate $\leq$ 1000 counts per second, Gaussian shaping time $6\,\mu\mathrm{s}$		
Segments:		
FWHM for $60\,\mathrm{keV}$ (^{241}Am)	≤ 1.3	≤ 1.2
FWHM for $1.33\,\mathrm{MeV}$ (^{60}Co)	≤ 2.3	≤ 2.1
Measurement conditions: The source is positioned in front of each segment. Count rate $\leq$ 1000 counts per second, Gaussian shaping time $6\,\mu\mathrm{s}$		
Efficiency: The efficiency of the detector at $1.33\,\mathrm{MeV}$ is measured with a ^{60}Co source at $25\,\mathrm{cm}$ distance from the Ge front end.		
Crosstalk: The crosstalk is extracted from a measurement of coincidences between the 36 segments using digital electronics. After adding the coincident signals of any pair of segments, the variation of the position of the $1332.5\,\mathrm{keV}$ full energy peak will not exceed $\pm 0.65\,\mathrm{keV}$.		

Table 4.1: The AGATA detector specifications which are subject to the acceptance test.

the tests in the triple clusters measured in Cologne (green $\times$) and the tests of the triple clusters performed in Legnaro (blue squares). For the segment energy resolution, it can be observed that most of the segments are well within the specifications. Only front segments (ring 1) are closer to the specification limit due to inhomogeneous and weaker electric field in this part of the detector.

4.2 Energy resolution of the first ATC detectors

The first triple cluster detector ATC1 was equipped with the following accepted crystals: A001, B002 and C002. Each detector was equipped with a core preamplifier and 12 triple AGATA segment preamplifiers. At first, analog energy resolutions were measured with a standard ORTEC 572 spectroscopy amplifier with $6\,\mu\mathrm{s}$ shaping time and a PC based MCA system and compared to the results of the tests in the single cryostat. Secondly, digital data were taken with 10 XIA DGF modules rev. E employing differential to single end converter boxes.

The crosstalk properties are determined by a 37 channel coincidence electronics system based on digital electronics. The core and the 36 segment energy signals were

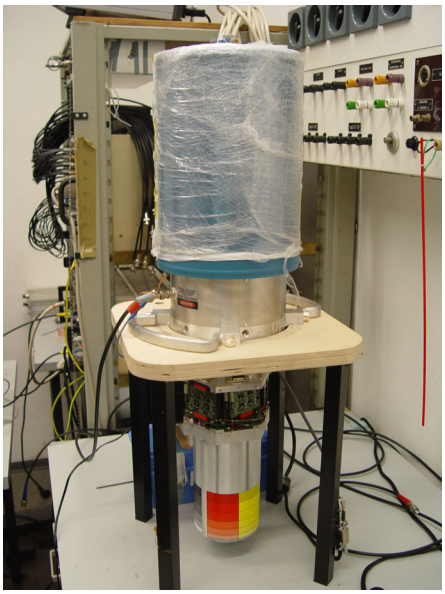

Figure 4.1: A single test cryostat for detector tests and characterization measurements.

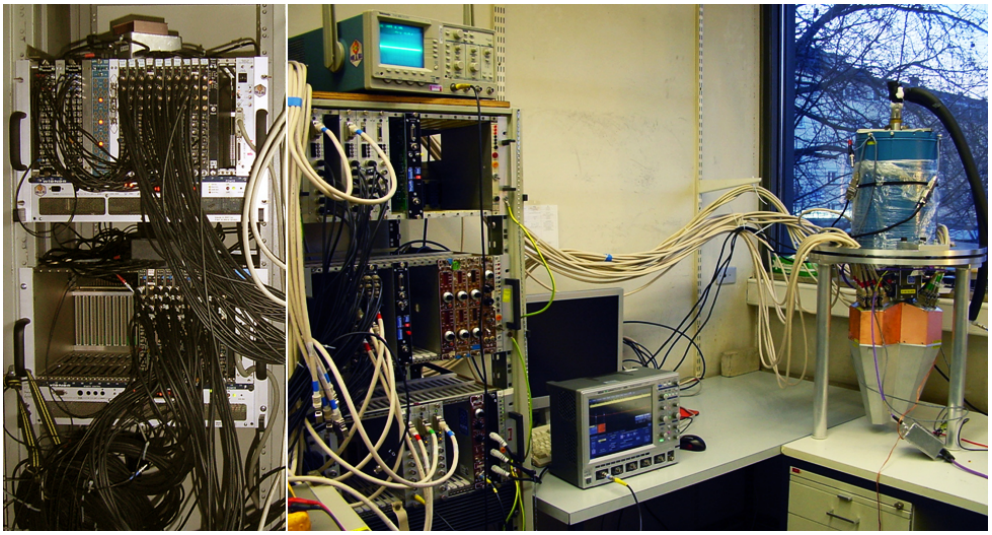

Figure 4.2: The triple cluster detector test setup at IKP. On the left, a CAMAC crate is shown, which contains the DGF digitizer modules. The right crate contains NIM electronics for analog measurements and conversion of the differential signal outputs to single ended signals.

digitized using 10 DGF-4C modules Revision E (Digital Gamma Finder with four channels by XIA LLC [42]). The analog part of the ADC contains a gain adjustment via a 12 bit DAC and a Nyquist filter to limit the bandwidth for high frequencies. The signal is digitized by a $14\,\mathrm{bit}$, $40\,\mathrm{MHz}$ ADC. Events are identified in the digitized signals by real time processing units (RTPUs) implemented in the FPGAs and then passed on to an on-board DSP, together with digitized signal traces captured in First-In-First-Out (FIFO) memories. A multiplicity bus and a readout with an adjustable threshold, busy and synchronization lines, and inputs for first-level triggers are used to incorporate the modules in a coincidence system. The DGF module for the core energy signal was configured as the master and provided a trigger signal for the readout of the nine DGF modules for all 36 segment signals. The FPGA extracts the γ-ray energy in real time by a software filter and produces $32\mathrm{k}$ γ spectra. The energy resolution obtained by digital pulse processing compares well with the resolution measured with analog spectroscopy amplifiers.

The energy resolution values in the triple cluster detectors have to meet the same specifications as those in the single test cryostats (see table 4.1). At higher energies of $1.33\,\mathrm{MeV}$ (^{60}Co), where the measurement is more time-consuming due to lower efficiency, the measurements were done with digital electronics. When the segments showed energy resolution values above $2.3\,\mathrm{keV}$, the signals were cross-checked and measured again using analog electronics. The results are shown in figures 4.7 and 4.8 with the green $\times$ symbols.

The most important measurements were performed after delivery of the ATC detectors to the AGATA demonstrator host laboratory at Legnaro after installation into the spectrometer. These measurements were performed with the final AGATA data acquisition chain starting with the new AGATA digitizers and the following signal processing chain. The demonstrator hardware is described in subsection 4.4.1. The first measurements concentrated on the high energy γ-ray of $1.33\,\mathrm{MeV}$. Measurements with all segments at low energies of $60\,\mathrm{keV}$ or $122\,\mathrm{keV}$ were not feasible because of the high absorption efficiency at low energies in the front parts of the detectors. The low energy γ-rays are fully absorbed within a few millimeters of germanium. Therefore, the resolution at very low energies turned out to be hardly measurable for all segments in the spectrometer array.

The final energy spectra are shown in 4.3 and 4.4 for the 36 segments measured with ATC1 detector B002 in Legnaro. The six figures in the first column show the six spectra for sector A, the front segment on top, followed by the higher rings, with the back segment in the figure on the bottom. The peak height is maximal in the front and going to lower values in the back rings due to absorption of the γ-rays in the front rings. Figure 4.5 (a) shows a spectrum for the core measured with ^{241}Am ($59.5\mathrm{keV}$) and ^{57}Co ($122\mathrm{keV}$) simultaneously. From the low energy spectrum in figure 4.5, it is obvious that the threshold can be set to only a few keV and resolve clearly low x-ray energies. The two high energy lines of ^{60}Co are displayed in figure 4.5 (b).

The peak-to-total values are shown in figure 4.6. The segments show a large Compton background due to the small volume. Especially the back segments suffer from the

Compton scattering happening in the front segments. The arriving γ-rays have a reduced energy after single or multiple Compton scattering. Creating add-back spectra for higher segment hit multiplicities increases the peak-to-total value. The core has a better peak-to-total ratio.

The results of the final Legnaro energy resolution values are summarized in Fig. 4.8 by the blue squares. The specifications for the measured energies are drawn as blue lines. The corresponding average values of all the data of the first four triple cluster detectors are given in table 4.2. All 444 signal channels of the 4 ATCs are working. At low γ-ray energies, the energy resolution of the ATCs measured at IKP is well within the specification values for almost all segments. Only a few segments show slightly higher resolution values. The values obtained in the triple cluster detector are on average even better than in the single test cryostat. Since the low energy resolution values are dominated by electronic noise, the obtained results demonstrate the successful design and integration of the new AGATA triple cluster detector. Especially the electronic properties comprising the cold and warm parts of the new preamplifier assembly are characterized by low noise in the triple cryostat despite the unprecedented integration density of 111 analog high resolution channels. The following reasons are attributed to the improvements in the final assembly with regard to the single test cryostat: (i) The test cryostat was partially equipped with older PSC823 preamplifiers in the beginning which were replaced by new AGATA preamplifiers at a later stage. (ii) An improved grounding scheme was applied in the ATC detector which reduces unwanted perturbing high frequency noise contributions (discussed in the previous chapter). (iii) A potential source for the microphonic effect was located at the core contact and removed.

The resolution of the $1.33\,\mathrm{MeV}$ line is dominated by statistical charge carrier fluctuations and detector properties. The direct comparison of the three different measurements is shown for each signal individually in Fig. 4.8 for the ATC1 as an example. The values illustrate the achieved high energy resolution of the ATC detectors. In addition, all core energy resolution values and the segment average energy resolution values are displayed in table 4.2 for $122\,\mathrm{keV}$ for the core, respectively $60\,\mathrm{keV}$ on the segments. The results are consistent within the one σ range. However, most of the values are better in the final detector arrangement in the AGATA demonstrator array in Legnaro.

Detector	Core FWHM [keV]		Segment average FWHM [keV]	
	Single cryostat	ATC @ IKP	Single cryostat	ATC @ IKP
ATC1:				
A001	1.34	1.44	1.079 ± 0.072	1.012 ± 0.053
B002	1.29	1.41	1.094 ± 0.086	1.039 ± 0.07
C002	1.275	1.21	1.034 ± 0.079	0.965 ± 0.063
ATC2:				
A003	1.22	1.42	1.142 ± 0.08	1.053 ± 0.065
B003	1.28	1.36	1.062 ± 0.068	0.995 ± 0.073
C005	1.24	1.49	1.163 ± 0.073	1.14 ± 0.107
ATC3:				
A002	1.26	1.44	1.033 ± 0.075	0.931 ± 0.11
B005	1.08	1.43	1.053 ± 0.078	1.045 ± 0.076
C006	1.09	1.42	1.153 ± 0.099	1.144 ± 0.106
ATC4:				
A005	1.23	1.28	1.039 ± 0.087	1.108 ± 0.171
B001	1.29	1.27	1.021 ± 0.071	1.029 ± 0.098
C003	1.16	1.33	0.998 ± 0.092	1.11 ± 0.378

Table 4.2: Energy resolution values for the first four ATCs. Core FWHM [keV] for $122\,\mathrm{keV}$ and average segment FWHM [keV] for $60\,\mathrm{keV}$ (^{241}Am) are given with their standard deviation (σ) values.

Detector	Core FWHM [keV]			Segment average FWHM [keV]		
	Single cryostat	ATC @ IKP	ATC @ INFN	Single cryostat	ATC @ IKP	ATC @ INFN
ATC1 :						
A001	2.33	2.46	2.4	2.092 ±0.156	2.194 ± 0.099	2.007 ± 0.129
B002	2.27	2.33	2.28	2.131 ± 0.105	2.099 ± 0.142	1.985 ± 0.085
C002	2.25	2.33	2.2	2.027 ± 0.115	2.108 ± 0.117	1.943 ± 0.114
ATC2:						
A003	2.280	2.41	2.56	2.098 ± 0.128	2.064 ± 0.078	2.057 ± 0.095
B003	2.23	2.52	2.42	2.081 ± 0.106	2.024 ± 0.086	1.937 ± 0.078
C005	2.2	2.21	2.39	2.207 ± 0.088	2.207 ± 0.077	2.077 ± 0.106
ATC3:						
A002	2.31	2.4	2.52	2.067 ± 0.108	2.019 ± 0.088	1.978 ± 0.087
B005	2.29	2.42	2.485	2.093 ± 0.139	2.132 ± 0.111	2.039 ± 0.127
C006	2.16	2.27	2.58	2.121 ± 0.087	2.085 ± 0.089	2.131 ± 0.148
ATC4:						
A005	2.230	2.400	2.190	2.033 ± 0.102	2.082 ± 0.127	1.914 ± 0.108
B001	2.170	2.500	2.300	2.055 ± 0.113	2.041 ± 0.105	1.906 ± 0.110
C003	2.340	2.350	2.400	2.084 ± 0.110	2.081 ± 0.092	2.042 ± 0.207

Table 4.3: Energy resolution values for the first four ATC detectors. Core FWHM [keV] and average segment FWHM [keV] for $1.33\,\mathrm{MeV}$ (^{60}Co) are given with their standard deviation (σ) values.

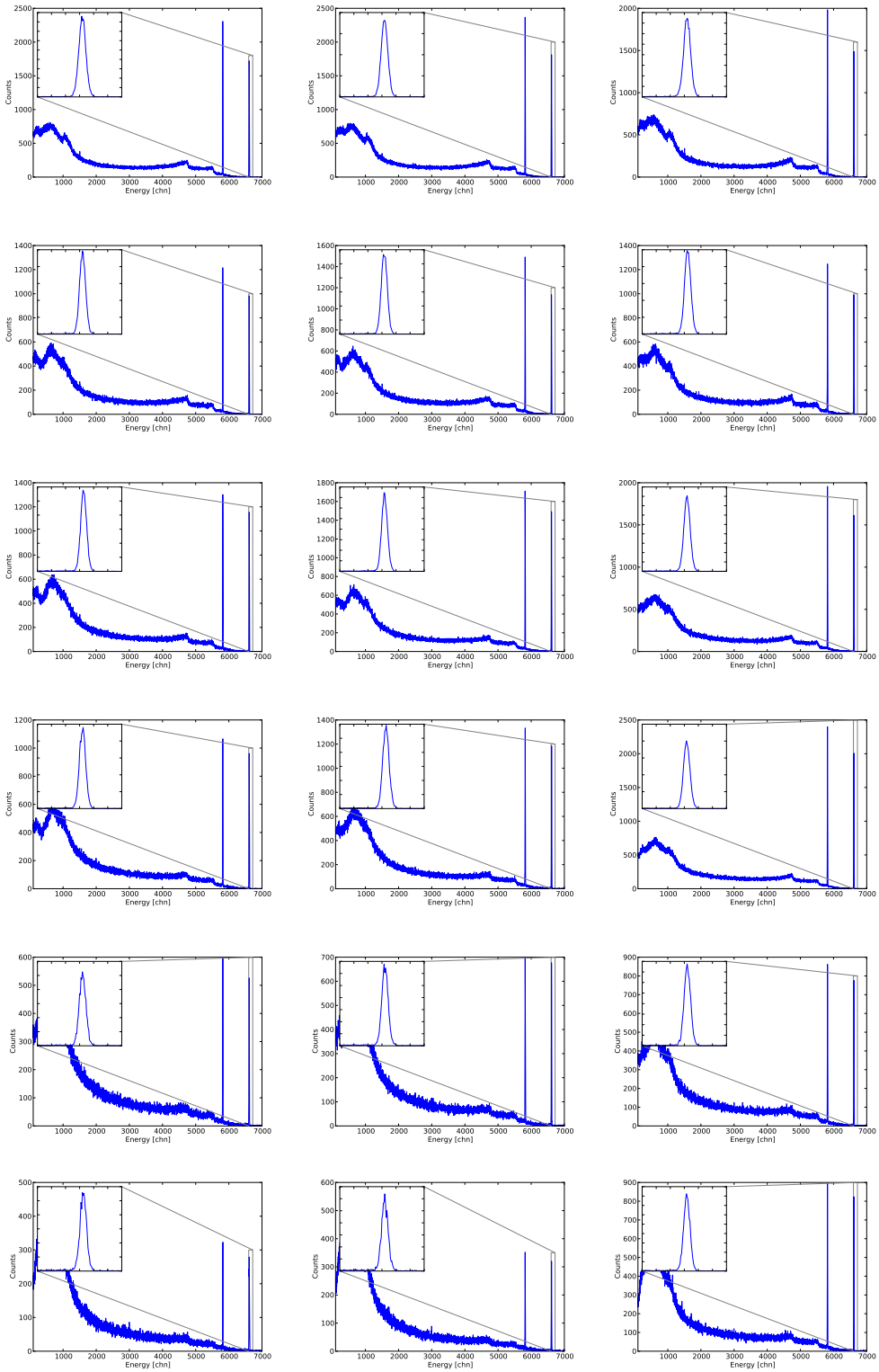

(a) Sector A (b) Sector B (c) Sector C

Figure 4.3: The 18 segment spectra of the three sectors A, B, and C measured with ATC1 detector B002 in Legnaro. The segments of the first ring are shown in the top figure, followed by one ring after the other until the back ring shown in the bottom figure. The ^{60}Co source was placed in front of the detector. Obviously, the back segments show a large Compton background due to scattering in the front rings. An inset of the zoomed $1332.5\,\mathrm{keV}$ ^{60}Co peaks displays the peak shapes.

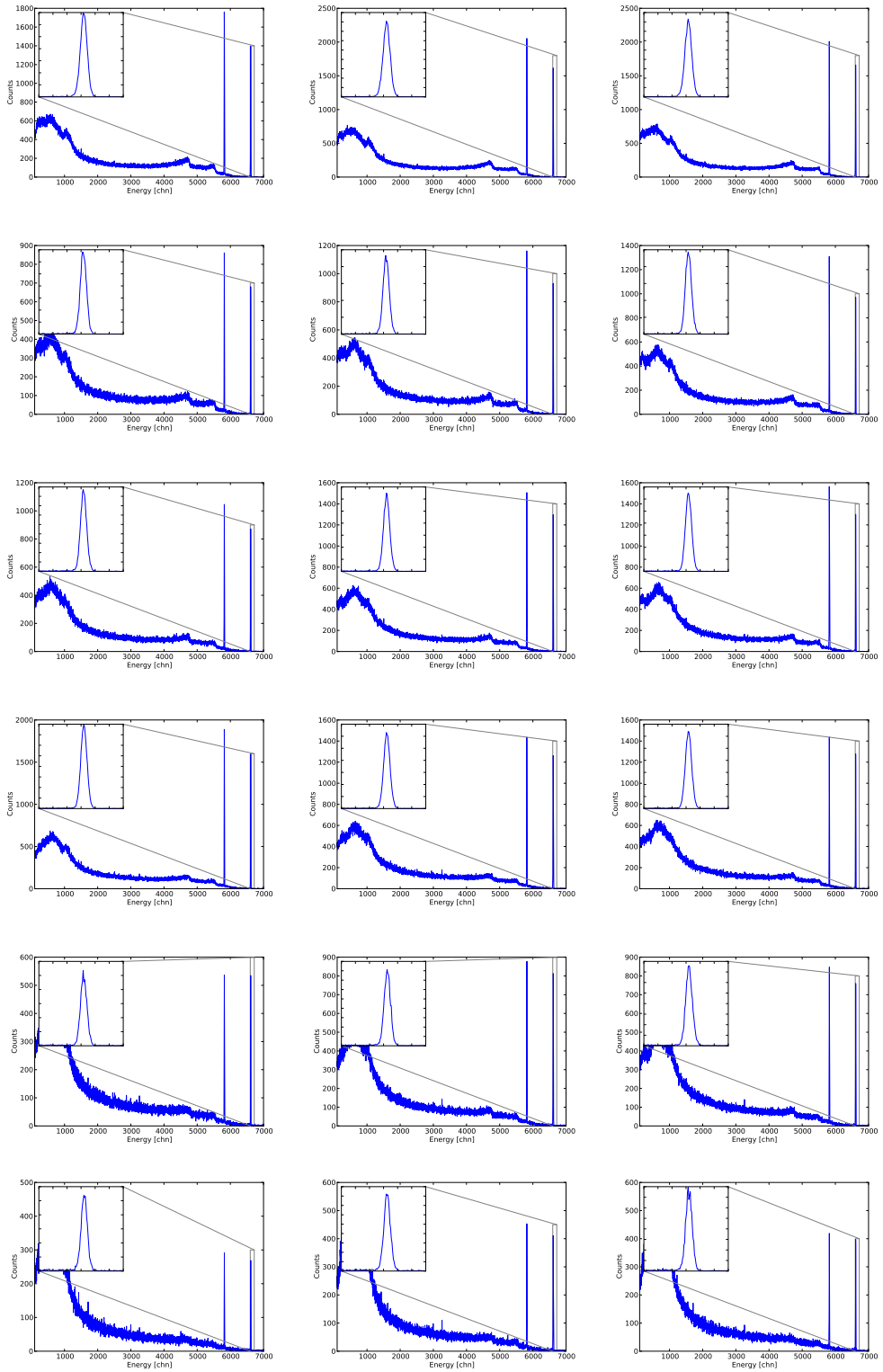

(a) Sector D (b) Sector E (c) Sector F

Figure 4.4: The 18 segment spectra of the three sectors D, E, and F measured with ATC1 detector B002 in Legnaro. The other three sectors are shown in figure 4.3, where a more detailed figure description is given.

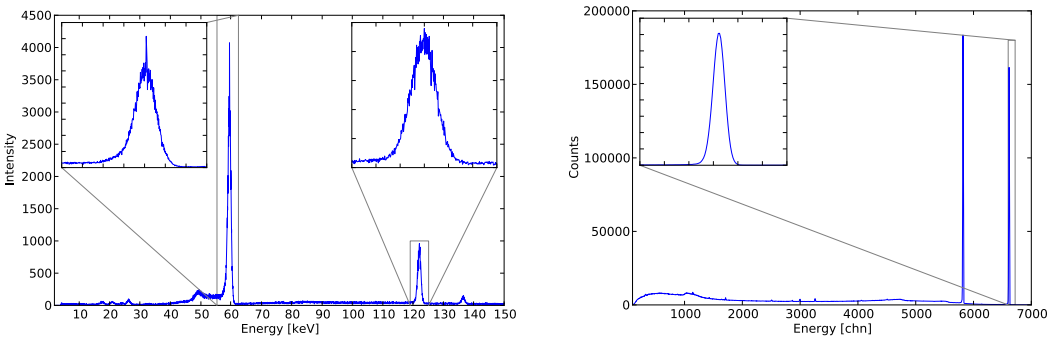

Figure 4.5: The left spectrum measured with detector C002 in ATC1 shows the peak shapes of the core at low energies of ^{241}Am (59.5keV) and ^{57}Co (122keV) simultaneously. The FWHM values of the two peaks amount to 1.2 and 1.28keV. The low threshold of only a few keV and the thin end cap and capsule of the detector facilitates the detection of x-rays. In spectrum (b), the core with the zoomed inset of the 1332.5 keV (^{60}Co) peak shows the high energy performance.

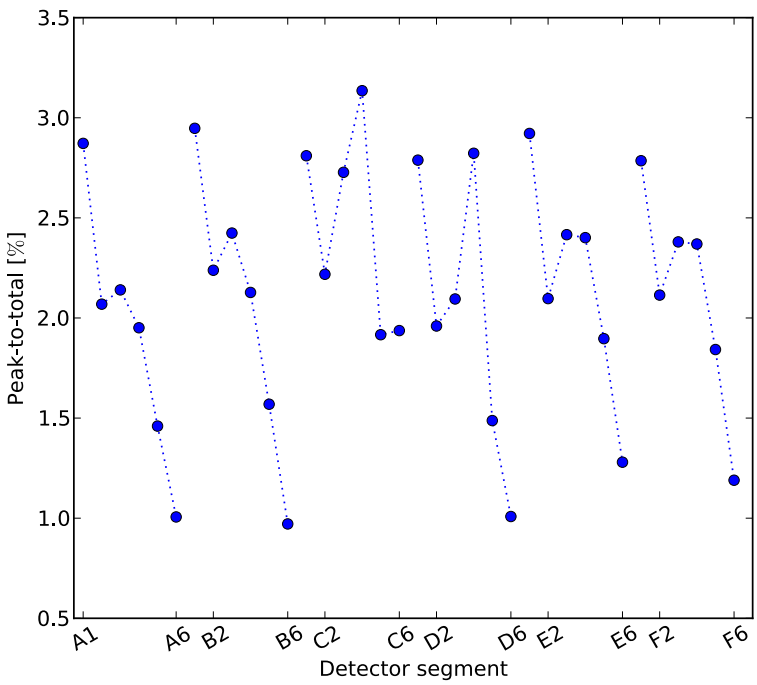

Figure 4.6: The peak-to-total ratio is shown for the 36 segments for ATC1 detector B002. The ^{60}Co source was placed in the target position. The back segments show a lower peak-to-total ratio due to Compton scattering. The peak-to-total for the core signal amounts to 16.43%.

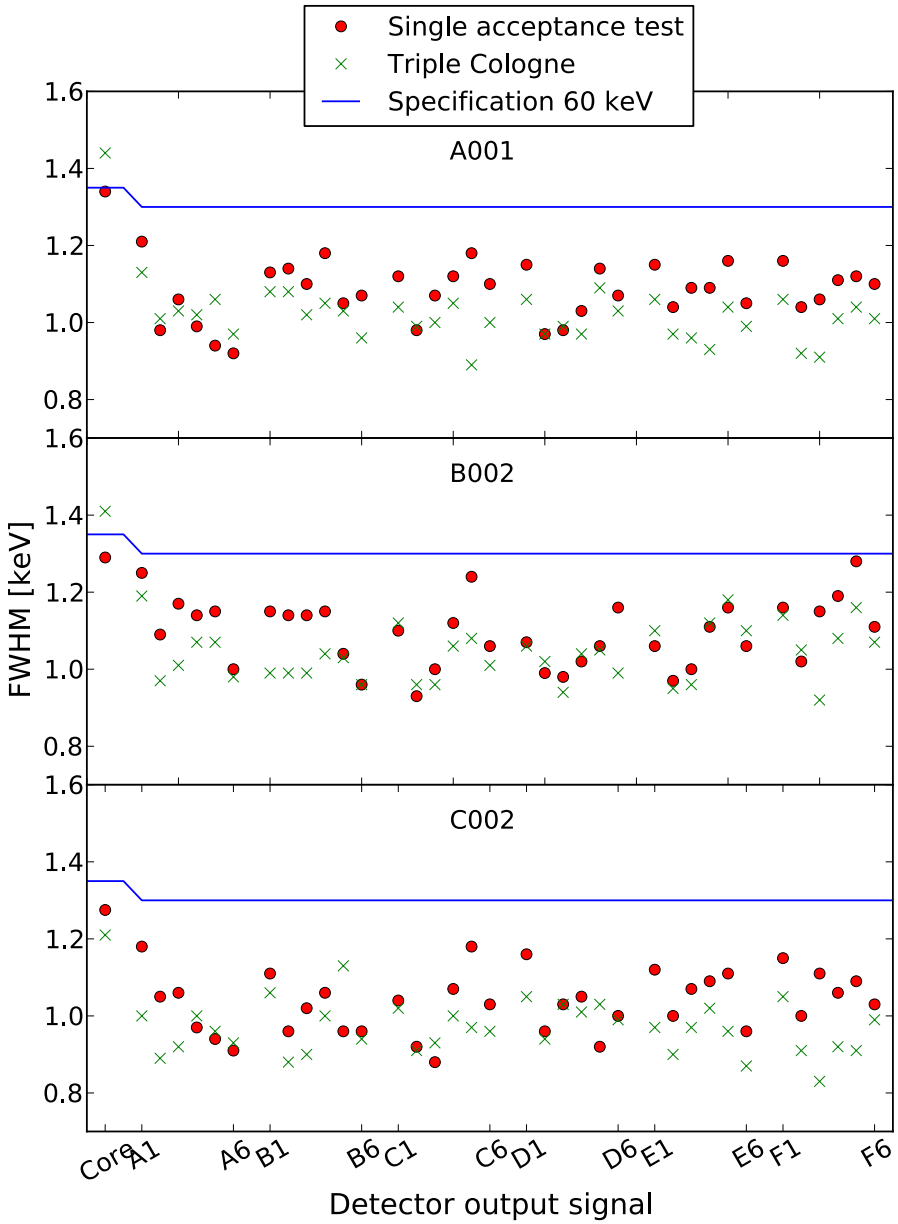

Figure 4.7: Energy resolution values for $E_\gamma = 122\,\mathrm{keV}$ for the core signal and $E_\gamma = 60\,\mathrm{keV}$ (^{241}Am) for the segment signals. The resolution of the three detectors A001, B002 and C002 at these low energies can be compared between measurements performed in the single test cryostat and in the ATC detector at IKP in Cologne. The values of the triple cryostat measurements are represented by the green $\times$ symbols and the single test cryostat results by the red dots. The specification limit for low γ-ray energies is displayed by the blue line.

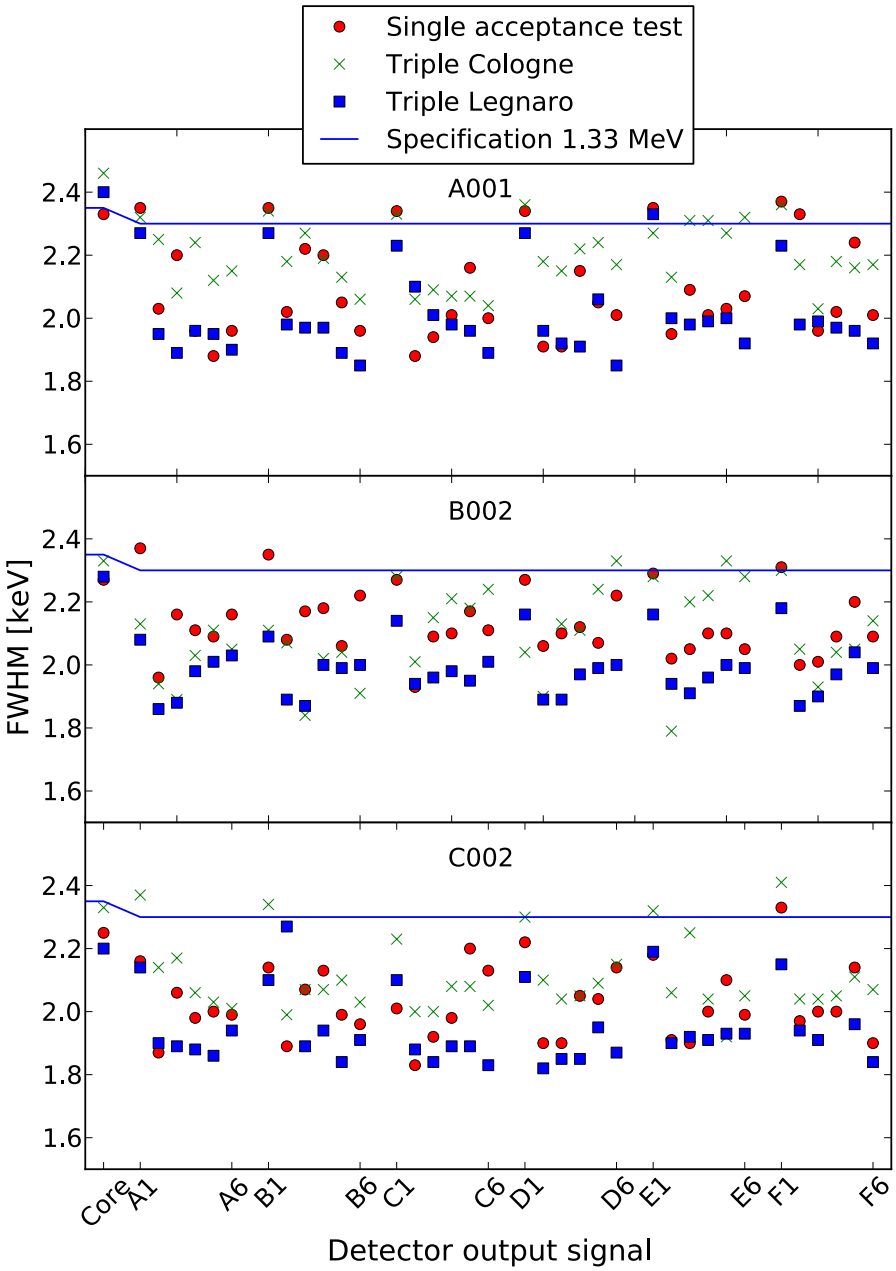

Figure 4.8: Energy resolution values for the core signal and the segments for $E_\gamma = 1.33\,\mathrm{MeV}$ (^{60}Co) for the segment signals. The resolution of the three detectors A001, B002 and C002 at these low energies can be compared between measurements done in the single test cryostat and the ATC detector at IKP and in Legnaro. The values of the triple cryostat in Legnaro are displayed by the blue squares while ATC values from Cologne measurements are represented by the green $\times$ symbols and the single test cryostat results by the red dots. The specification limit for high γ-ray energies is displayed by the blue line.

4.3 Crosstalk properties

4.3.1 Crosstalk within individual crystals

Segmented detectors show mutual capacitive coupling of the segments which appears as crosstalk contribution in the signal pulses and cause reduced energy resolution values. This crosstalk had to be measured experimentally with high qualtity and to be corrected. Results of the crosstalk measurement with the three asymmetric AGATA detectors A001, B002 and C002 are shown in figure 4.9. The data points in this figure show peak energy shifts of the $1332.5\,\mathrm{keV}$ line of ^{60}Co as a function of all possible twofold segment combinations. These values are obtained for the core energy and for the segment sum energy under the condition that the full energy deposition is divided into exactly two segments. The major crosstalk effect of the segmented Ge detector is the reduced segment sum peak energy. The energy difference of typically $2.0\,\mathrm{keV}$ is related to the coupling of the core signal to the segments. A refined inspection of the peak position of the twofold events from figure 4.9 reveals a regular pattern as a function of pairwise segment combinations. The energies are shown for the core energy signal (+, red symbol) and for the sum of the two segment energy signals ($\times$, green symbol). All twofold data obtained on three similar asymmetric AGATA crystals are shown in figure 4.9. A detailed description of the underlying detector physics and a quantitative analysis of the observed peak shifts within a linear electronic model of the new AGATA detectors are described in [43].

Energy variations around the calibration reference are observed for the core signal as a function of the twofold segment combinations. The variation of the core signal data points cannot be explained in a satisfying way with the linear electronic model of the detector and its preamplification stage used for the segment sum energy fluctuations. Much stronger additional effects are needed to explain the red data points from the core in figure 4.9. Electron trapping occurs also in new and not neutron damaged HPGe detectors. This effect can explain the major effect of shifted energy values observed in the core signals. The energy differences vary systematically as a function of the radius in the Ge crystal. This result is presented and worked out in detail in chapter 6.

4.3.2 Crosstalk between different detectors

The crosstalk properties of the complete asymmetric triple cluster detectors are investigated by a second method, which is based on events of source measurements with only one detector segment collecting a real energy deposition in the detector volume. In coincidence with the energy information of the triggering segment, the baseline shifts in all other segments are recorded as a function of the energy deposition in the hit segment. The equivalent energy ratio corresponding to these baseline shifts gives directly the crosstalk contribution in the untriggered segments. The measured crosstalk ratios are of the order $\approx 10^{-3}$ and linearly follow the energy deposition.

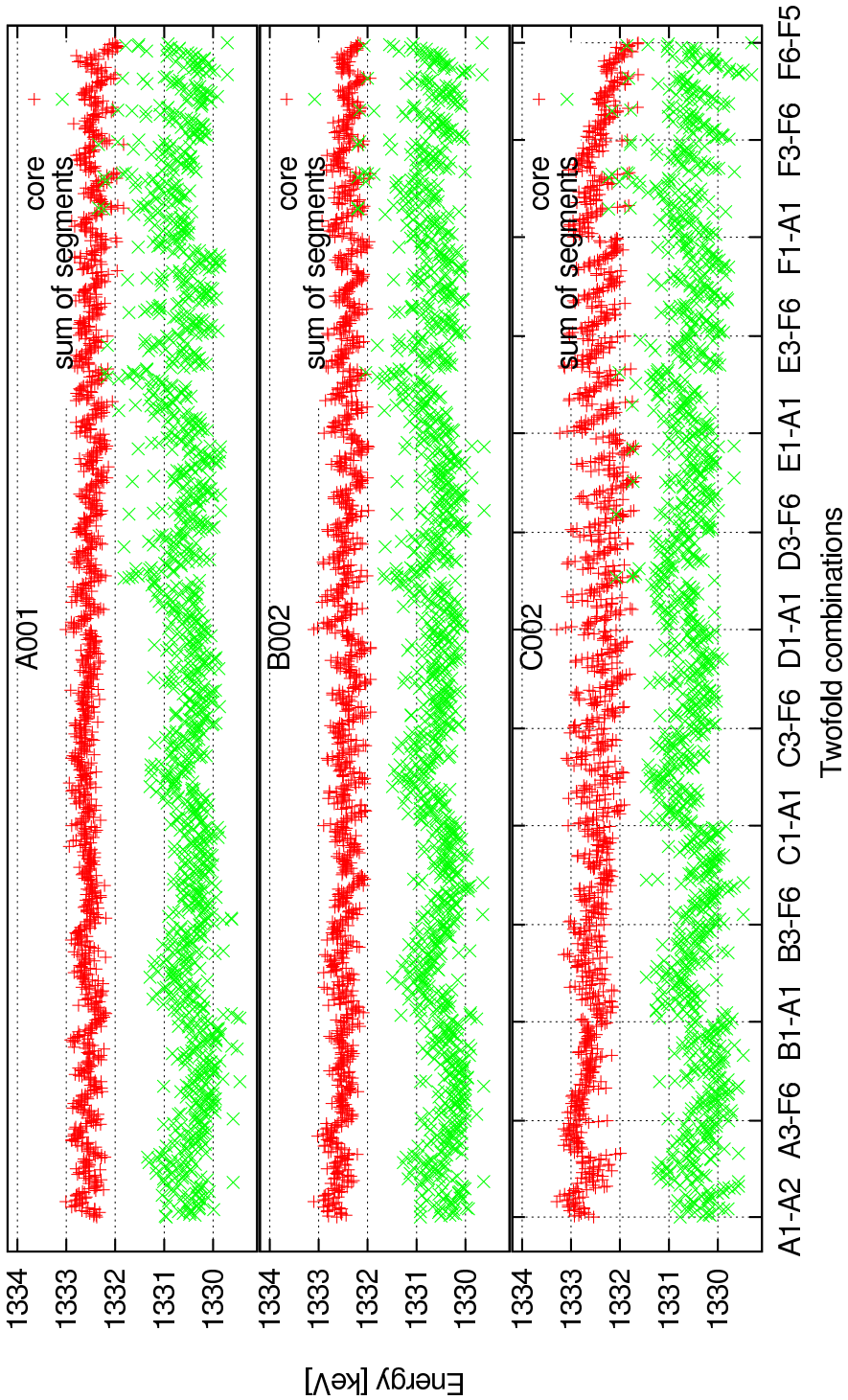

Figure 4.9: Results of the crosstalk measurements of the detectors A001, B002 and C002 in single test cryostats. The crosstalk contributions are observed through energy shifts in the centroids of the $1332.5\,\mathrm{keV}$ line by gating on all 35×36 possible twofold combinations. The energies are shown for the core energy signal (+, red symbol) and for the sum of the two segment energy signals ($\times$, green symbol). On the x-axis first all combinations with segment A1, then all combinations with A2, etc. are shown.

The measurements were performed with the three AGATA detectors analyzing the coincident traces over a $7\,\mu\mathrm{s}$ long time period using the digital acquisition system. Only one triggering segment with its full energy deposition in this segment was required for taking data. The pulses of all remaining segments without any trigger condition are recorded and analyzed simultaneously requiring only the pulse from the hit segment. The coincident core signal is used to create a trigger condition to read out the untriggered segments. The inverted negative signals of the untriggered segments are measured with digital electronics using the trapezoidal filter technique. After the identification of the true energy deposition in exactly one segment, the simultaneous baseline shifts are recorded, which occur in all remaining 35 non-hit segments. This method allows for the determination of precise and absolute crosstalk matrix elements. The method applied to quantify this result in the triple cluster detector is based on an extension of the 36×35 possible combinations to the full 111×110 possible crosstalk matrix elements within the full triple cryostat, where the core signals are treated as master trigger signals but also as slave signals. Parts of the matrix are shown in figure 4.10. Only subsets of the sectors A and F of each detector, which are facing each other in the triple cryostat arrangement, are shown. More details of these measurements are described in [44]. The crosstalk pattern within each single detector is on the level of $0.1\,\%$ as shown in the diagonal subplots in figure 4.10. The observed structure can be entirely attributed to the capacitive coupling between the core and the segments.

The main results of these investigations are: The crosstalk between the different three detectors is negligible for the new ATC detector, displayed in the off-diagonal graphs. No indication for crosstalk contributions appear between segments of different detectors at a level of $\leq 10^{-5}$. A small crosstalk component was observed between a firing detector and the core signal of a neighboring detector. These contributions at a level of $\leq 10^{-4}$ are well within the acceptable limits.

4.4 The AGATA demonstrator in Legnaro, Italy

The AGATA demonstrator is foreseen to prove the feasibility of the pulse shape analysis and of the γ-ray tracking concept in a subset of five triple cluster detectors of the whole array under real experimental conditions in real time. The total efficiency of this subset at a γ-ray energy of $E_\gamma = 1\mathrm{MeV}$ amounts to about 3% in the nominal position of the array with a distance of $23.5\,\mathrm{cm}$ between the detector front face and the target. The demonstrator is currently installed at INFN (National Institute of Nuclear Physics) in Legnaro, Italy, at the target position of the magnetic spectrometer PRISMA. A tandem accelerator delivers heavy-ion beams, which can be further accelerated with the use of the superconducting linear accelerator ALPI up to a velocity of $\beta \approx 10\%$ for the γ-emitting products [45, 46, 47]. The coupling of PRISMA and the AGATA demonstrator is used to measure nuclear reaction products in coincidence with PRISMA and the in-beam γ-rays with the ATC detectors, which are crucial for proper Doppler correction. Four AGATA triple cluster detectors were mounted in the array (see Fig. 4.11)

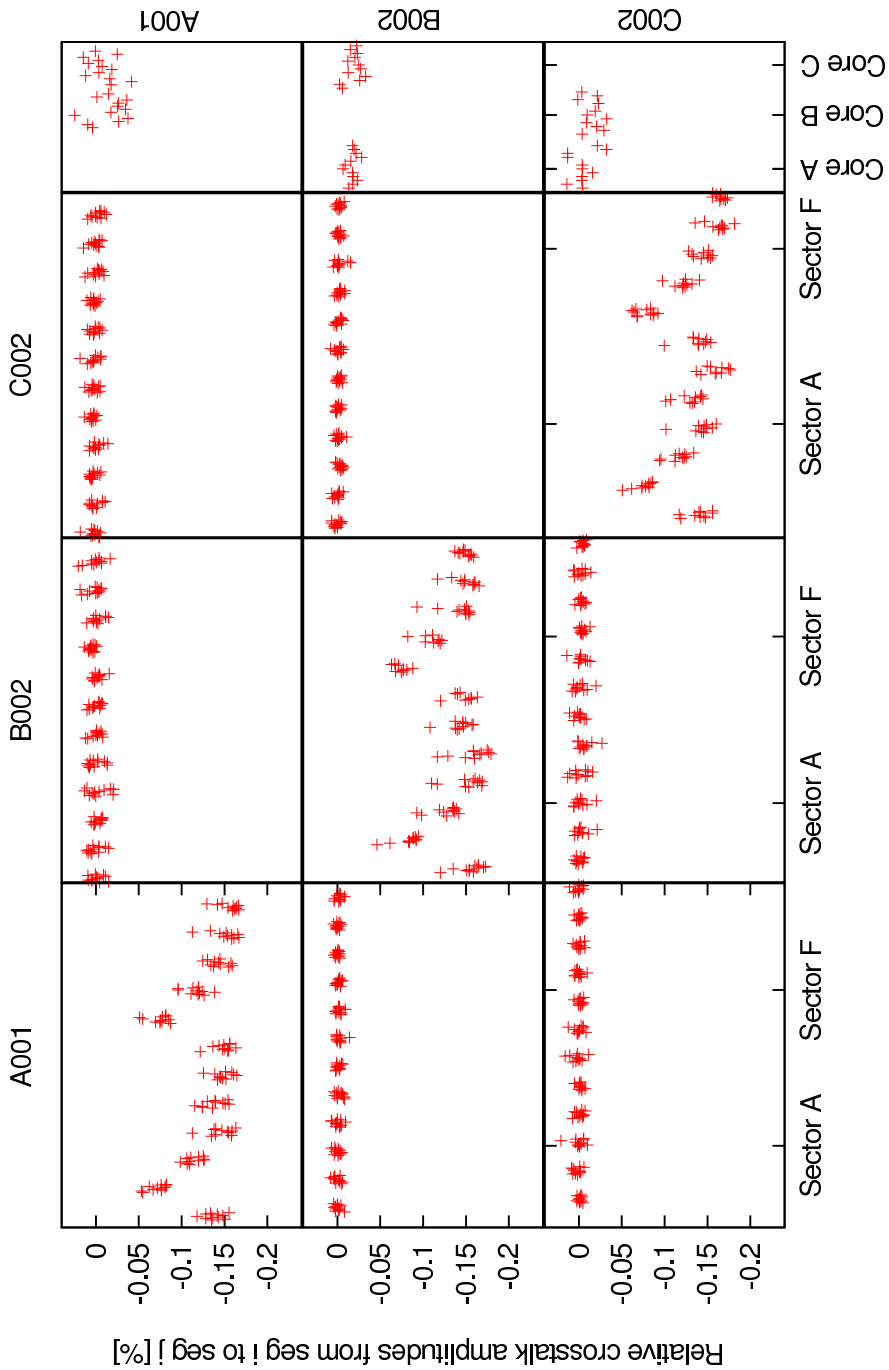

Figure 4.10: Relative crosstalk contributions for subsets of the sectors A and F of each detector and the cores are shown. The values were extracted from the observation of baseline shifts in onefold events. Diagonal subplots show crosstalk within each detector on the $0.1\,\%$ level. Segments of different detectors show no crosstalk ($\leq 10^{-5}$). Contributions between the cores are at a level of $\leq 10^{-4}$.

in 2010. The fifth triple cluster is represented by a set of three aluminum blocks due to missing crystals from the manufacturer.

All triple cluster detectors were successfully mounted and tested in the array. As an example, the energy resolution values are shown in figure 4.8 and in table 4.2 for the first four triple cluster detectors. The optimization of the detector performance is described in chapter 3. Since April 2010 all four triple cluster detectors are working reliably and well within the specifications for the first physics campaign at INFN, Legnaro.

4.4.1 The signal acquisition chain

The whole signal acquisition chain was developed within the AGATA collaboration. The analog, differential signal outputs from the detector preamplifiers are connected to the digitizers, which are mounted in racks close to the array, via $10\mathrm{m}$ video MDR (Mini Delta Ribbon) cables. Each digitizer module receives the signals from 1 crystal, (36 segments and 1 core). The $100\mathrm{MHz}$ digitizer based on $14\mathrm{bit}$ ADCs is used to convert the analog signals of the preamplifier signals into a digital bit stream. All the digital signals are transferred to the pre-processing electronics through $75\mathrm{m}$ long optical fibres, while a logic signal is also sent from the core signal to the Global Trigger System (GTS) and to the Clock system. The GTS has the same sampling rate as the digitizer, i.e. $10\,\mathrm{ns}$.

The pre-processing modules are responsible for extracting all useful data from the data stream of the digitizer for every channel in real time. The short traces with the leading edge of the signal triggered by the core contact of the crystal are sent to the computer farm where the pulse shape analysis is performed. The trigger condition may additionally be validated by the GTS. The pre-processing modules also determine parameters such as the energy of the absorbed γ-ray and the time of the interaction, time-stamped based on a common clock.

The pre-processor data for all detectors are combined with the Global Trigger System in a computer farm, where the pulse shape analysis, γ-ray tracking, event building, and the online analysis are performed. The data are stored on a large local disk array of the computer farm before being eventually transferred to the computing center Grid Tier1 [11].

This newly developed data acquisition system is in operation and capable of handling 555 individual signals. Its functionality has been demonstrated in various measurements and is described in [47].

4.4.2 Measurements in Legnaro

The data for the analyses described in chapters 5 and 6 were acquired in Legnaro from three triple cluster detectors in the demonstrator array. These measurements were performed with the three detectors ATC1, ATC2 and ATC4. The mounted crystals had the following labeling:

Triple cluster	Crystal		
ATC1	A001	B002	C002
ATC2	A003	B003	C005
ATC4	A005	B001	C003

A wide range of γ-ray energies was covered using the sources ^{60}Co,^{241}Am,^{137}Cs and ^{152}Eu from $60\,\mathrm{keV}$ to $1.4\,\mathrm{MeV}$. The sources were placed precisely in the target position, which is the focal point of the array, at a nominal distance of $23.5\mathrm{cm}$. The distance between the detector front face and the target position was also set individually with the flexible frame to control the count rate of the detectors.

Initially, an energy calibration for every signal was performed using the full-energy peak of $1.17\,\mathrm{MeV}$ and $1.33\,\mathrm{MeV}$ (^{60}Co), which was used for each acquired measurement. At first, only data with energy information were acquired without signal traces in order to check the detector properties. These data were also used for the combination of core and segment energies, depicted in chapter 5. For the study of electron trapping, the signal traces had to be recorded and stored. About 10 Terabyte of data were recorded in total. The analysis of local effects in small detector regions demands for the large amount of data because a sufficient amount of events is needed for a precise determination of the peak centroids and of the full width at half maximum. The analysis of coinciding hit segments also requires a large amount of data.

Furthermore, collimators were used to display the quality of the pulse shape analysis. The diameter of the collimator used for the result in figure 4.12 amounts to $2\,\mathrm{mm}$ and its length to $8\,\mathrm{cm}$. The ^{137}Cs source has one γ-energy of $662\,\mathrm{keV}$. The collimator was focused perpendicular to the front face of the detector close to the central contact of the detector B001 in ATC4. It was oriented towards sector B close to sector C. The FWHM of the peaks in the projections of $5\mathrm{mm}$, respectively $6\mathrm{mm}$ are consistent with [48], where a detailed analysis of the position resolution is given. The position resolution amounts to $4\mathrm{mm}$ for γ-ray energies of $1.5\,\mathrm{MeV}$. For lower energies the position resolution is reduced to approximately $6\mathrm{mm}$ for γ-ray energies of $660\,\mathrm{keV}$.

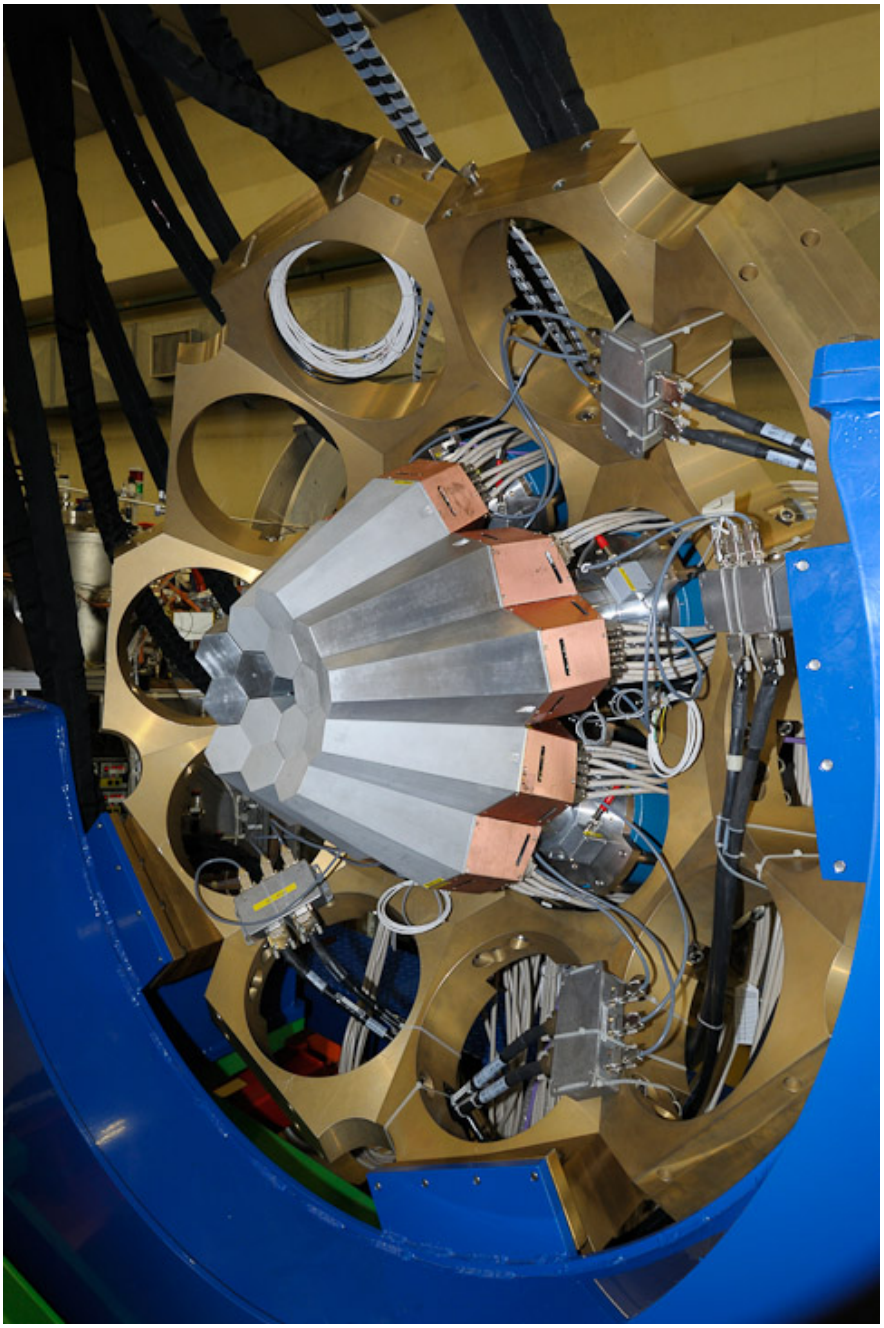

Figure 4.11: The AGATA demonstrator with four ATC detectors at INFN, Legnaro in summer 2010.

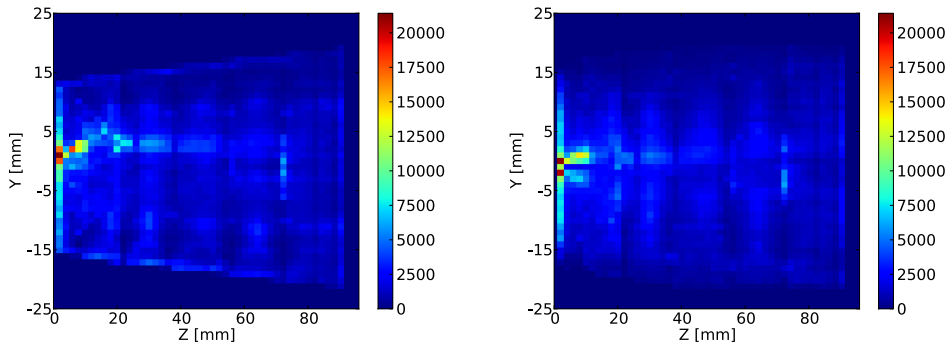

(a) x-z projection

(b) y-z projection

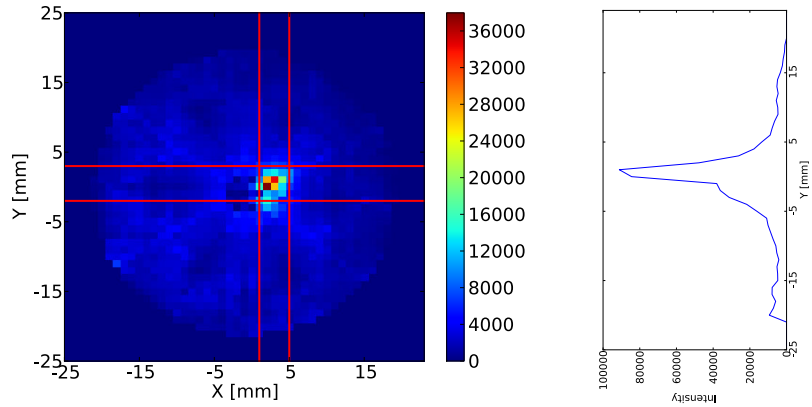

(c) x-y projection

(d) y projection

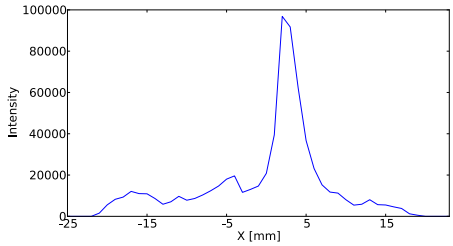

(e) x projection

Figure 4.12: Position information of the interaction points from the PSA result are shown. A collimated ^{137}Cs source with one γ-energy at $662\,\mathrm{keV}$ provided a focused γ-ray beam perpendicular to the front face of the detector close to the central contact in sector B. The diameter of the collimator was $2\,\mathrm{mm}$. The x-z (a) and y-z (b) projections show the interaction positions in depth. Additionally, a projection on the x-y plane, the front face of the detector, is shown in (c). The spot close to the center clearly shows the functionality of the pulse shape analysis. The contour plot in (c) is projected on the x and the y axes and shown in (e), respectively (d) with FWHM values of the peaks of $5\mathrm{mm}$ on the x and $6\mathrm{mm}$ on the y projection.

Chapter 5

Increased energy resolution through averaging of the core and the segment signals

A new option for improved γ-ray spectroscopy of highly segmented HPGe detectors like the ATC detector is the possibility to analyze the signals of the cathode and the anode simultaneously and to utilize the redundant information of two electronically decoupled independent measurements. This new approach improves the signal-to-noise ratio significantly in addition to the newly developed low noise preamplifiers. The compound of detector and electronics is described in chapter 3 and shown in figure 3.5. While the 36 segments are DC coupled, AC coupling is used for the core to read out the signal on the biased electrode. The purpose of this chapter is to show that the signals which are generated by the influenced charges on the core and segment electrodes can be combined for an improved energy resolution. The combination of the individually measured signals on an event-by-event basis can be done on- or off-line through averaging of the measured energies, which applies not only to the energy signal but also to the noise contribution of through signals. Through averaging the information of the cathode and the anode a better signal-to-noise ratio

$$\frac{E}{\Delta E} \sim \frac{S}{N} \tag{5.1}$$

is achieved with the known noise contributions from equation 2.3.

For statistically independent noise, the following expression is valid

$$\overline{N_C^2 + N_S^2} = \overline{N_C^2} + \overline{N_S^2}$$

with the noise on the core signal N_C and on the segments N_S [49]. Due to the averaging procedure the amplitude of the signal and of the noise is reduced by a factor of $\frac{1}{2}$. The noise of both signals is added quadratically with the approximation $\overline{\left(\frac{N_C}{2}\right)^2} \simeq \overline{\left(\frac{N_S}{2}\right)^2}$

to calculate the average noise N_A:

$$\begin{aligned}\sqrt{\overline{N_A^2}} &= \sqrt{\overline{\left(\frac{N_C}{2}\right)^2 + \left(\frac{N_S}{2}\right)^2}} \\ &= \sqrt{\overline{\left(\frac{N_C}{2}\right)^2} + \overline{\left(\frac{N_S}{2}\right)^2}} \\ &= \frac{1}{\sqrt{2}}\sqrt{\overline{N_C^2}}\end{aligned} \tag{5.2}$$

Averaging the signals of the core and the hit-segment sum gives the same signal amplitude as in the individual signals and a noise width that is reduced by $\frac{1}{\sqrt{2}}$. Using equation 2.3, the FWHM for the peak of the averaged signal looks as follows

$$W_T = \sqrt{W_D^2 + W_X^2 + \left(\frac{1}{\sqrt{2}}W_E\right)^2} \tag{5.3}$$

where W_E describes the noise of the individual signal. One can achieve the best energy resolution if both, the core and the segment resolution, are as similar as possible and W_D and W_X are negligible.

5.1 Averaging at low energies

A first measurement at a very low energy $60\,\mathrm{keV}$ from ^{241}Am was performed in Cologne, and the signals of the core and the segments were averaged on an event-by-event basis. A single cryostat was used with a symmetric 36-fold segmented AGATA detector. At low energies, the electronic noise is the main contribution to the FWHM and the improvement is expected to be the largest. The low energies are absorbed in the first millimeters of the material so that the inner segments see hardly any counts in a fully equipped triple cluster detector. Special care was put into minimizing the electronic noise of the core electrode by using a quad amplifier which multiplies each signal by four and thus reduces the energy range in the acquired spectra. Two ^{241}Am sources were located facing the sides of the detector (see Fig. 5.1) so that the segments counted with a low rate of about $100\,\mathrm{Hz}$ and the core electrode of $2\,\mathrm{kHz}$. An additional ^{60}Co source was used for calibration purpose as Am shows only one peak in the spectrum. The gains of the detector output signals were adjusted to the same amplitude of all signals.

The data (traces and energies) were recorded with digital electronics which is described in section 4.3.2. The ideal filter settings for the digital trapezoidal filter are listed in table 5.1.

The energy spectra were analyzed and the following energy resolution at $60\,\mathrm{keV}$ are given in figure 5.3 (a): (i) energy resolution of 36 segments, (ii) core energy resolution divided and gated by the 36 segments and (iii) the average of the segment and of

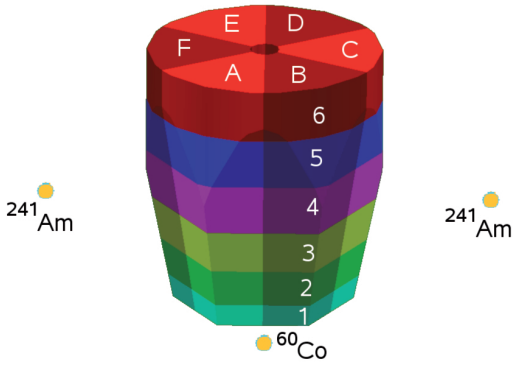

Figure 5.1: Source positions in the measurement.

Slow filter rise time	$9.5\,\mu$s
Slow filter gap	$4\,\mu$s
Fast filter	$225\,$ns
Fast filter	$100\,$ns

the core signals which are gated by individual segments. The average FWHM of the 36 segments is $1.2\,$keV for the core, $1.1\,$keV for the segments and the averaged signals show the expected improved resolution value of $0.87\,$keV. An example spectrum is shown for segment A1, for which the core and the average spectrum are compared. The improvement is obvious as the averaged peak is narrower and significantly higher.

A correlation between the core and the segment signals is expected to exist especially at higher energies, where statistical fluctuations in the charge carrier production process are clearly correlated for electrons and holes. The trapped charge carriers should have similar effects on both electrodes.

In practice the detector noise may not be totally uncorrelated and the assumption of uncorrelated electronic noise of different signals needs experimental inspection. Electronic noise can be characterized by means of a multivariate normal distribution. A covariance matrix is used to check for the correlation of the noise between the signals of all the outputs. The covariance matrix for the detector signals $\vec{X}$ can be described by

$$M(\vec{X}^k, \vec{X}^l) = \sum_{k,l=1}^{37} \sum_{i=1}^{N} \frac{(x_i^k - \bar{x}^k)(x_i^l - \bar{x}^l)}{N}$$

where the matrix elements M^{kl} gives the correlation between $\vec{X}^k = (x_1^k, ..., x_N^k)$ and $\vec{X}^l = (x_1^l, ..., y_N^l)$. N represents the length of the discrete signal, i.e. the number of signal trace elements. For the AGATA detectors, this matrix expresses the correlation of all 37 signals. A set of untriggered noise samples of $292 \times 25\,$ns ticks from this measurement is used for all 37 signals. The result of the 37×37 covariance matrix is

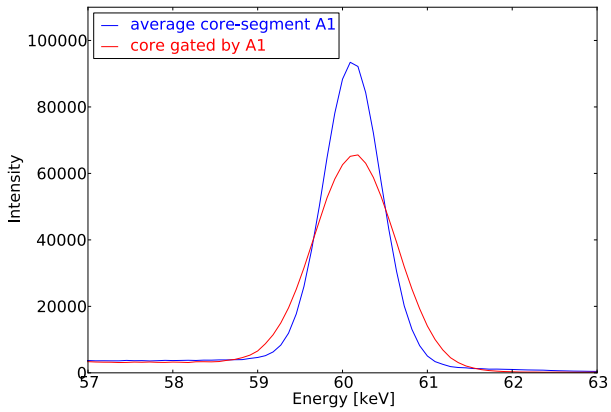

Figure 5.2: Spectra for the core gated by A1 and the average signal of A1 measured with ^{241}Am, exemplary of all signals.

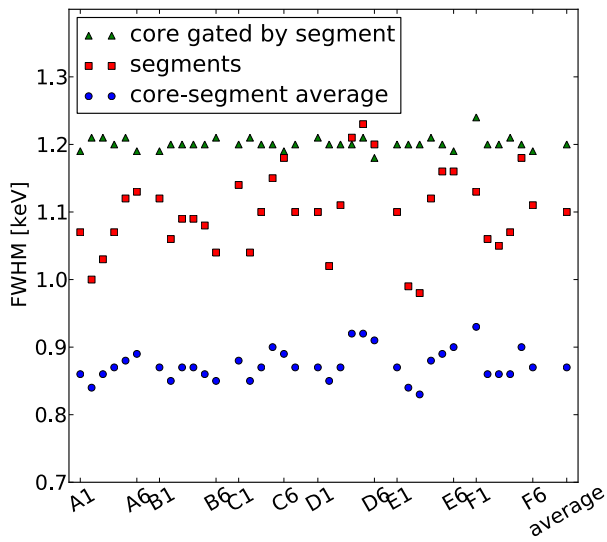

Figure 5.3: Energy resolution values for core signals gated by the individual segments displayed by the green triangles, the segments FWHM (red squares) and the FWHM of the core-segment average gated by individual segments (blue dots). The measurement was performed at IKP with a symmetric AGATA detector in a single cryostat with a γ-ray energy of $60\,\mathrm{keV}$ (^{241}Am).

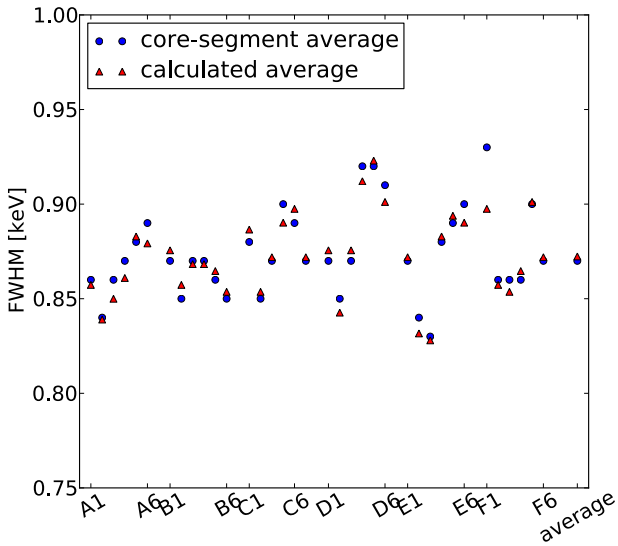

Figure 5.4: Energy resolution values for the core-segment average gated by individual segments (blue dots) compared to the calculated expected values (red triangles) using equation 5.3. (Details on the calculation are given in the text). The measurement was performed at IKP with the symmetric AGATA detector S002 in a single cryostat with a γ-ray energy of $60\,\mathrm{keV}$ (^{241}Am).

plotted in figure 5.5.

For uncorrelated variates, the entries of the matrix will be 0. While $M^{kl} > 0$ means a positive correlation between $\vec{X}^k$ and $\vec{X}^l$, $M^{kl} < 0$ means that $\vec{X}^l$ decreases for increasing $\vec{X}^k$. The diagonal elements are described by σ^2 [50]. Of interest is the correlation between the core and the segment signals. Therefore, the first-row elements are analyzed in more detail. The off-diagonal elements of the first row show a distribution around zero with a small shift to positive values of $0.046\,\mathrm{keV}$. The shift shows the average correlation between the core and the segments in this measurement. From the covariance matrix, the correlated electronic noise from the noise samples is estimated to be $0.046\,\mathrm{keV}$ and can be used to calculate the expected improvement.

The noise due to charge collection and trapping is correlated. Therefore, there is no improvement expected for this type of noise. At a γ-ray energy of $60\,\mathrm{keV}$, the contribution of charge carrier statistics is almost negligible. With a Fano factor of 0.1, the noise contribution of the statistics of charge creation $2.35^2\epsilon FE$ equals $0.098\mathrm{keV}$. Trapping effects on the segment signals are negligible and low for the core as the γ-rays are absorbed very close to the outer electrode. The equation 5.3 is used to calculate the expected improvement. Dividing only the uncorrelated noise by $\sqrt{2}$ and adding the correlated noise and the charge carrier statistics quadratically gives the values shown in figure 5.3 (b). The calculated values are in good agreement with the FWHM of the measured spectra. The error in the calculation arises from the estimation of the

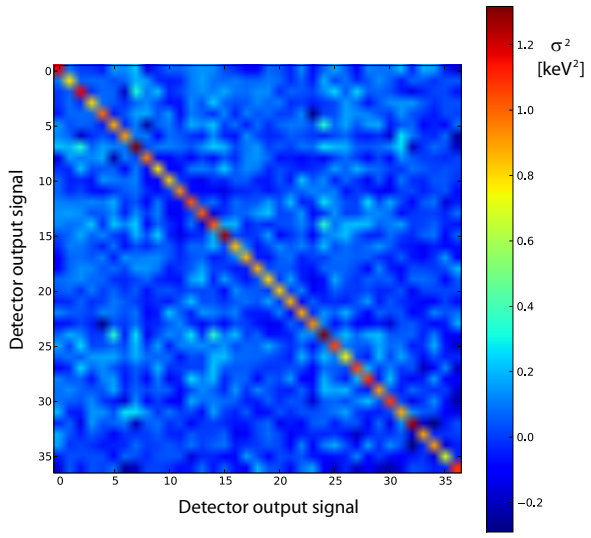

Figure 5.5: 37 × 37 covariance matrix for all 37 detector signals in S002 from $7.3\,\mu\mathrm{s}$ of noise samples.

correlated noise and from the Fano-factor and is estimated to be $0.04\,\mathrm{keV}$.

The correlation of the core and the segment signal is shown in the 2-dimensional distribution for segment A1 in figure 5.6(a), which is very low for $60\,\mathrm{keV}$ of γ-ray energy. Gating on a certain region of the peak (figure 5.6(b)) in the core demonstrates that the coincident segment spectrum is almost unshifted compared to the ungated case with the same energy resolution within an error of $50\,\mathrm{eV}$ in the FWHM.

At higher energies (shown in figure 5.7 for $1.3\,\mathrm{MeV}$), a pronounced correlation between the segment and the core energy is visible arising from correlated statistical fluctuations in the charge carrier production and in trapping.

The improvement in energy resolution due to the averaging of two signals is most pronounced for low energies but also works over the whole energy range. From measurements in the demonstrator array in Legnaro (described in chapter 4.4.2), onefold events from prominent ^{152}Eu source energies are used to determine the FWHM for energies from $122\,\mathrm{keV}$ to $1408\,\mathrm{keV}$. Spectra for the averaged signal of segment A1 are shown for the energies $122\,\mathrm{keV}$, $344\,\mathrm{keV}$, $964\,\mathrm{keV}$, and $1408\,\mathrm{keV}$ in figure 5.8. The results are shown in table 5.1 for detector B002 and in table 5.2 for detector C002. The average values of the three types of the 36 signals are given. Again a clear improvement of the energy resolution is obtained at the lowest energy of $122\,\mathrm{keV}$. The equation 5.3 is used to calculate the expected improvement. Dividing only the uncorrelated noise by $\sqrt{2}$ and adding the correlated noise and the charge carrier statistics quadratically results in the values $1.0\,\mathrm{keV}$ respectively $0.99\,\mathrm{keV}$. For increasing ener-

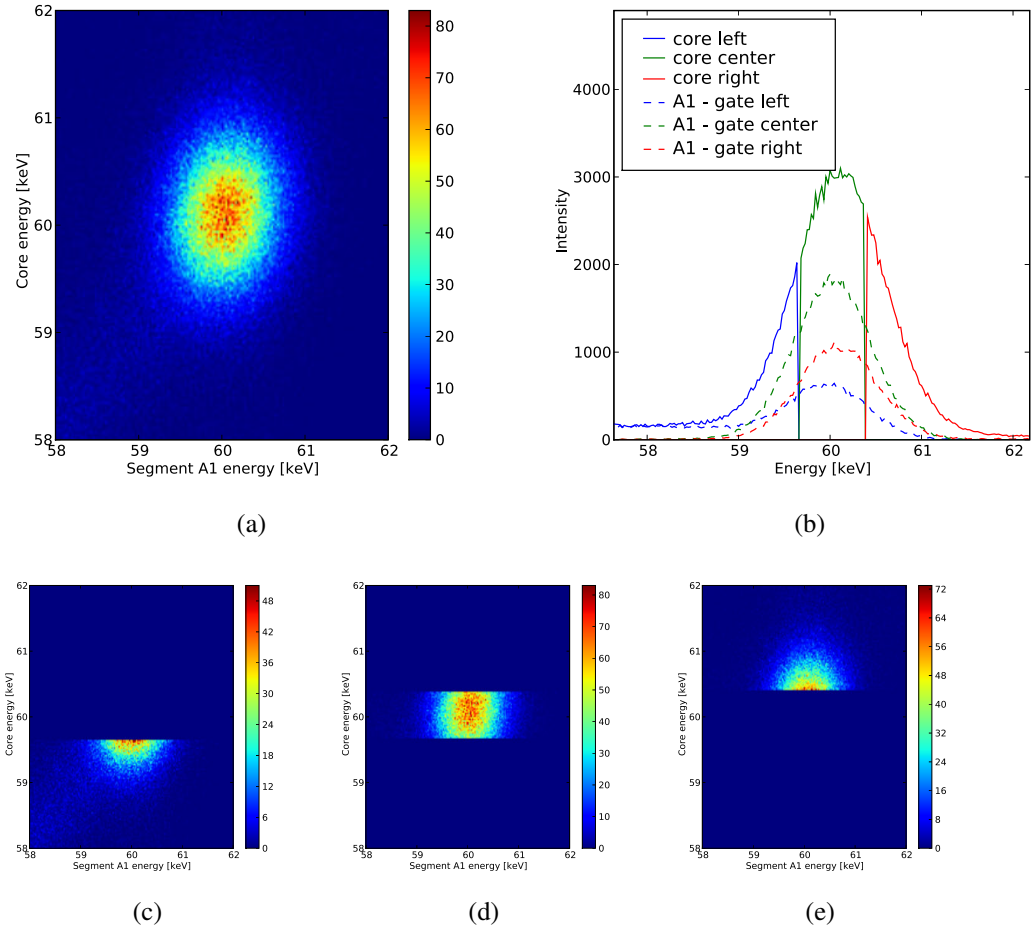

Figure 5.6: Core energy vs. segment energy matrix for segment A1 in detector S002 at 60 keV (a) and gated spectra for core and segments at 60 keV (b). The core peak is divided into three regions. The low energy part of the peak is shown by the blue solid line and the contour plot (c). The center peak region is represented by the green line and the contour plot (d) and the high energy part by the red line and by figure (e). The peaks for the corresponding segment events are displayed by the dashed lines in the same colors. Only a small correlation between the core and the segment signals is observed at low energies.

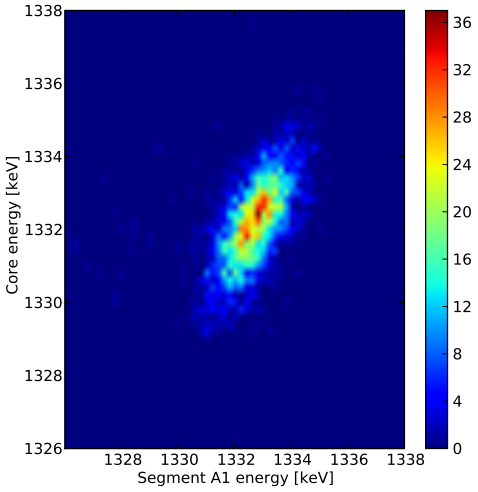

Figure 5.7: Core energy vs. segment energy matrix for segment A1 in detector C002 at $1.3\,\mathrm{MeV}$ showing the correlation between core and segment signals at a high γ-ray energy.

Energy [keV]	Core FWHM	Segments FWHM	Average FWHM
122	1.394	1.208	1.0
344	1.608	1.388	1.221
964	2.091	1.893	1.774
1408	2.457	2.259	2.174

Table 5.1: Energy resolution at different energies of ^{152}Eu measured for core, segments and average of core and segments with detector B002.

gies up to $1408\,\mathrm{keV}$, a less pronounced improvement of the FWHM is consistent with the smaller fraction of electronic noise at higher energies. A good agreement is found for the comparison between the measured and calculated energy resolutions shown in figure 5.9 (a) for the detector B002 and in (b) for the detector C002. For the calculation of the expected energy resolution, equation 5.3 is consulted. The relative importance of the three noise contributions is described in the following subsection.

Further improvement of the electronic noise, especially on the core signal, would lead to an additional advance in energy resolution.

Noise contributions

The relative importance of the noise contributions of equation 2.3 to the measured energy resolution for the averaged signal of the core and the segments is shown in figure 5.10. Three measurements are combined in this plot, namely one with ^{152}Eu, one with ^{137}Cs, and one with ^{60}Co so that a wide range of energies is covered.

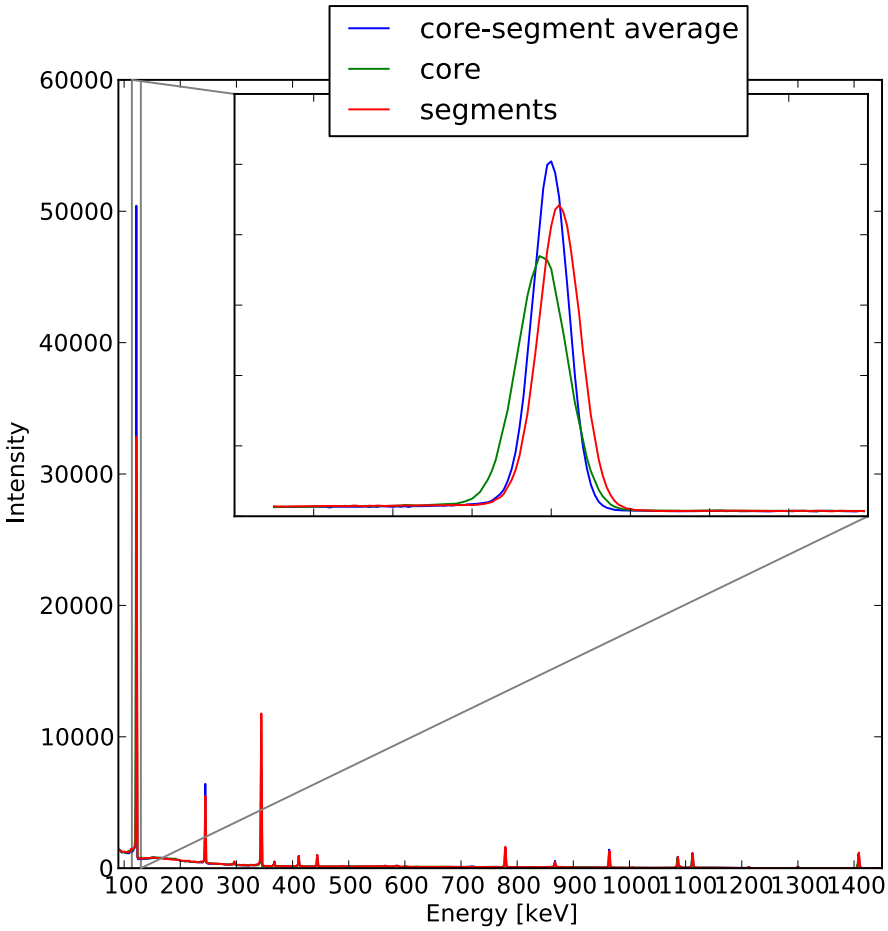

Figure 5.8: ^{152}Eu spectrum with 122 keV inset measured with detector B002 in ATC1. The core, the segment, and the core-segment average spectra are shown. The gain in energy resolution is the largest at low energies. At higher energies, the FWHM of the average signals is slightly better than the segment-energy resolution. The energy resolutions for prominent peaks are given in Tab. 5.1.

Energy [keV]	Core FWHM	Segments FWHM	Average FWHM
122	1.448	1.139	0.989
344	1.603	1.308	1.189
964	1.986	1.729	1.640
1408	2.315	2.027	2.013

Table 5.2: Energy resolution at different energies of ^{152}Eu measured for core, segments, and average of core and segments for detector C002.

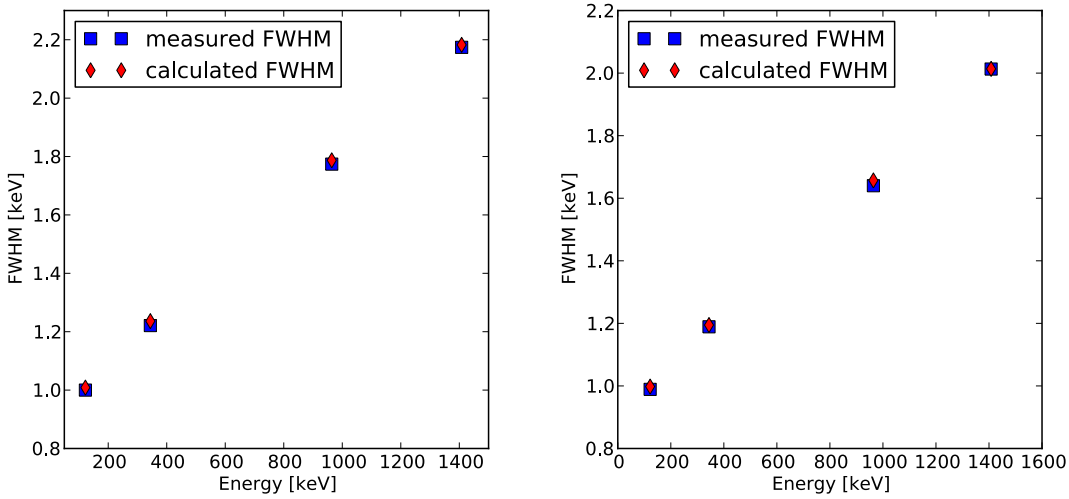

(a) B002 (b) C002

Figure 5.9: Energy resolution at different energies of ^{152}Eu measured and calculated using equation 5.3 and the relative importance of the three noise contributions shown in figure 5.10. The comparison is shown for the detectors B002 and C002.

The electronic noise was determined by means of a precision pulser. The electronic resolution does not depend on signals from the detector, but only on the electronic response to the injected pulse. For the core electronics, the FWHM of the pulser in detector B002 amounts to $1.47\,\mathrm{keV}$. The average FWHM for the segments was calculated based on the individual FWHMs and results in $0.95\,\mathrm{keV}$. This value has an estimated error less than $50\,\mathrm{eV}$. Therefore, the calculated width of the electronic noise of the average signal amounts to $0.86\,\mathrm{keV}$ and is displayed by the green line in the plot. The Fano factor calculated in chapter 6 equals $F = 0.095 \pm 0.005$ and is used to describe the $\sqrt{E}$ summand in the equation. It is shown as the blue line in figure 5.10. The remaining noise is assumed to arise from charge trapping, and it is obtained by subtracting the other two contributions from the measured FWHM. The yellow points in figure 5.10 display this contribution and are fitted with the yellow line $(0.006 \cdot x + 0.162)$. The error bars are due to the uncertainty of the Fano factor. The linear fit agrees well with the estimated trapping contribution as well as with the expected linear behavior. All three components are added quadratically and result in the red line in the plot which gives a consistent picture of the measured FWHM over the whole energy range.

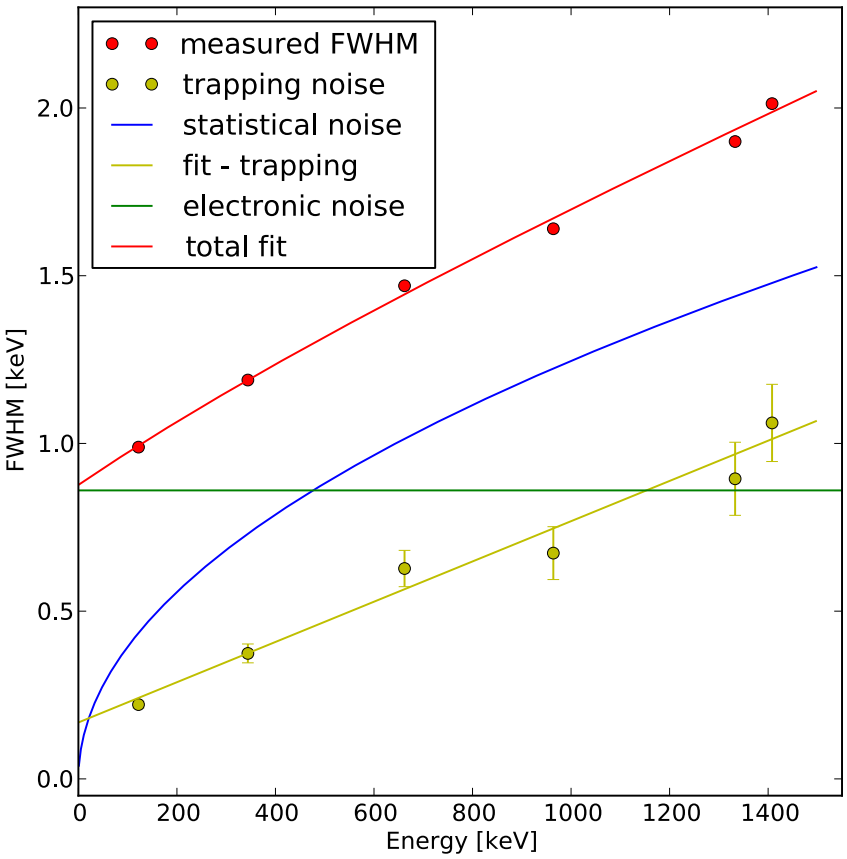

Figure 5.10: Energy dependence on the absolute energy resolution (given in FWHM) of the averaged signal of core and segments in the AGATA detector B002. The total FWHM and three noise contributions are compared in the plot.

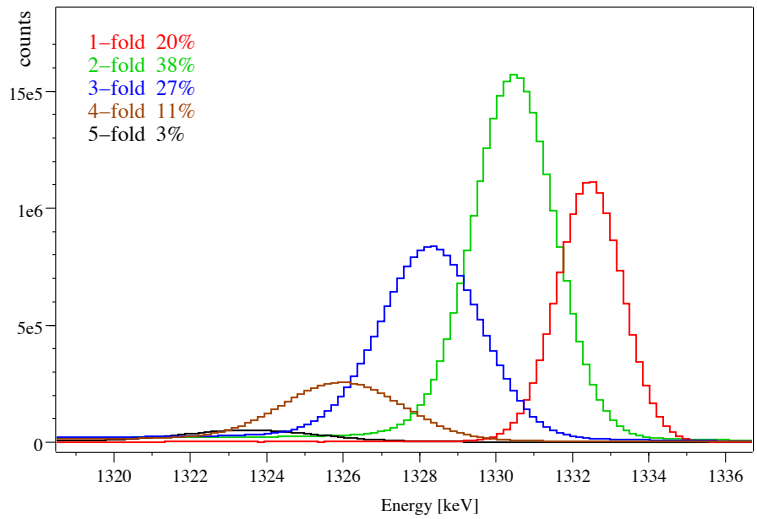

Figure 5.11: The segment sum energies for $E_\gamma = 1332.5$ keV plotted for different segment multiplicities. The centroids of the energy peaks are lowered as a function of the segment fold.

5.2 Crosstalk correction

For energy deposition at higher energies than e.g. $60\,\mathrm{keV}$, the interaction points are distributed over several segments. For these higher segment multiplicities or segment folds, the effect of crosstalk strongly influences the segment-sum signals. A fold-dependent energy loss is observed (see figure 5.11). The highly segmented detector represents an electronic network, where a mutual capacitive coupling of the segments involved in the absorption of the γ-ray and the central electrode lowers the measured energy. This systematic shift of energies impairs the energy resolution. The understanding of the systematic behavior enables the correction, which can be applied on an event-by-event basis.

The systematic crosstalk pattern is analyzed in the easiest case of twofold combinations ($36 \times 35 = 1260$ combinations). The measured energies relate linearly to the true energies:

$$\vec{E}_{meas} = \mathbf{B} \cdot \vec{E}_{true} \tag{5.4}$$

The matrix $\mathbf{B}$ includes the core-to-segment crosstalk in the first row and the crosstalk between segments in the 1260 off diagonal matrix elements:

$$\mathbf{B} = \begin{pmatrix} 1+\delta_{0,1} & 1+\delta_{0,2} & 1+\delta_{0,3} & \cdots & 1+\delta_{0,36} \\ \hline 1 & \delta_{1,2} & \delta_{1,3} & \cdots & \delta_{1,36} \\ \delta_{2,1} & 1 & \delta_{2,3} & \cdots & \delta_{2,36} \\ \delta_{3,1} & \delta_{3,2} & 1 & \cdots & \delta_{3,36} \\ \vdots & \vdots & \vdots & \ddots & \vdots \\ \delta_{36,1} & \delta_{36,2} & \delta_{36,3} & \cdots & 1 \end{pmatrix} \tag{5.5}$$

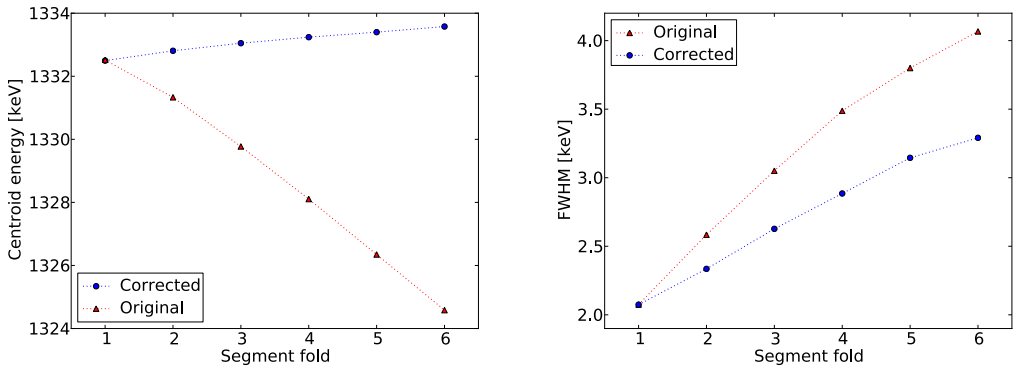

Figure 5.12: Energy shift of the $1.3\,\mathrm{MeV}$ γ ray energy versus number of hit segments for uncorrected and corrected spectra (a) and FWHM for the same spectra (b).

The matrix elements δ_{ij} are derived experimentally either from the onefolds or from the twofolds. In the first case, segment j absorbs the γ-ray, while the baseline shift of all segments i as a function of the energy provides the crosstalk parameters. Alternatively, the matrix elements are extracted from energy spectra recorded for all the $1260/2$ segment-sum combinations. Matrix elements are derived from twofold spectra for the following correction. A full description of the applied correction procedures is given in [44].

Unperturbed onefolds cover about 20% and twofolds 38% of the events at $1.3\,\mathrm{MeV}$ (figure 5.11). For higher folds, the same parameters are used by linear superposition of the parameter of the involved segments for the crosstalk correction [51].

The result of the crosstalk correction is demonstrated by the shift of the peak position (see figure 5.12 (a)) and by the improvement in energy resolution (see figure 5.12 (b)). While the peak centroid shifts to lower energies with a higher fold in the original spectra, this behavior is compensated in the corrected spectra. Also, the segment-sum energy resolution is improved considerably by crosstalk correction.

Unfortunately, crosstalk correction does not completely compensate for the decline in energy resolution at higher folds. The signal-to-noise ratio is reduced in the individual segments as the energy is split on more than one segment, but the electronic noise contribution remains the same. In contrast to the $\sqrt{2}$ reduction of the noise of the averaged signal for the sum of the segments, the uncorrelated electronic noise is multiplied by $\sqrt{2}$ in a twofold interaction with a similar noise from the segments as an extra preamplifier is involved.

Finally, all events from each fold are combined like in a real experiment. The original add-back spectrum for the segment sum is compared to the one which is crosstalk corrected in figure 5.13. The peak shape is improved drastically and the FWHM decreases from $4.05\,\mathrm{keV}$ to $2.52\,\mathrm{keV}$ after correction.

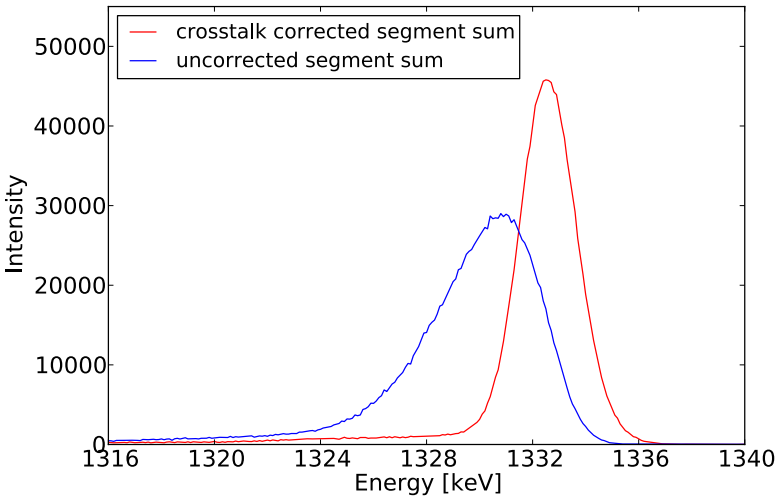

Figure 5.13: The add-back segment-sum spectrum of the $1.33\,\mathrm{MeV}$ γ ray energy uncorrected (energy resolution $4.05\,\mathrm{keV}$) and crosstalk corrected (energy resolution $2.52\,\mathrm{keV}$).

5.3 Averaging of multifold events

The crosstalk corrected add-back segment spectra were used to average the core and the segment signals in higher folds, i.e. $80\,\%$ of the events. Crosstalk correction and the averaging of the core and the segment-sum are applied on an event-by-event basis. Energy resolution values for a γ-ray energy of $1.33\,\mathrm{MeV}$ are given as a function of fold in table 5.3. A comparison of the core, the segment-sum, and the corrected and averaged core-segment-sum FWHM for up to segment fold six is given. For all measurements, the statistics of counts in the peaks result in errors below $50\,\mathrm{eV}$ for the FWHM value.The ^{60}Co $1.3\,\mathrm{MeV}$ energy in detector C002 was used to demonstrate the final improvement of the energy resolution.

For all segment multiplicities, the energy resolution is improved and the energy positions are significantly better aligned. A combination of all hit-segment folds gives an increased spectrum quality with a FWHM of $2.15\,\mathrm{keV}$ at $1.3\,\mathrm{MeV}$.

	core [keV]	corrected segment sum [keV]	corrected & averaged [keV]
1-fold	2.296	2.074	1.96
2-fold	2.257	2.335	2.059
3-fold	2.241	2.627	2.149
4-fold	2.219	2.885	2.238
5-fold	2.223	3.145	2.342
6-fold	2.218	3.291	2.409

Table 5.3: Energy resolution for the first six segment multiplicities measured with ^{60}Co for the core, the corrected segment-sum, and the average of the core and the corrected segment-sum for detector C002.

Chapter 6

Charge carrier trapping and its correction

Charge carrier trapping is observed in n-type high purity germanium detectors. The large volume of the detectors favors a loss in the collected charge due to the long drift length of the charges. The trapping of charge carriers influences the peak shape in the γ-spectra. Trapping is mostly associated with neutron damage, which creates hole traps. In the original state, before neutron damage takes place, mainly electron trapping is observed. Highly segmented detectors and pulse shape analysis bring up new possibilities to study these trapping effects. Having the signals of both, core and hit segment electrodes simultaneously, allows for a deeper investigation of electron and hole trapping. The PSA enables the determination of the interaction position inside the crystal. The position sensitivity can be used to understand position-dependent effects. A correlation between trapping and detector region can be observed and is used for the correction on an event-by-event basis.

6.1 The origin of trapping

The general properties of germanium and the special configuration of segmented AGATA detectors are described in chapters 2.1 and 3. In undamaged n-type high purity germanium, one observes mainly electron trapping. Either deep impurities (level in the middle of the band gap) or shallow impurities (levels near the conducting band) may cause the charge carriers to get trapped during migration to the electrodes. The charge carriers do not contribute to the influenced signal on the electrodes as long as they are trapped. Levels of various impurities are shown in figure 6.1 according to [14]. Fast detrapping is very unlikely in case of deep impurities, while shallow donor levels can show fast detrapping. Other types of deep impurities can act as recombination centers. These impurities are capable of capturing both, majority and minority carriers, causing them to annihilate. Both trapping and recombination contribute to a loss of charge carriers.

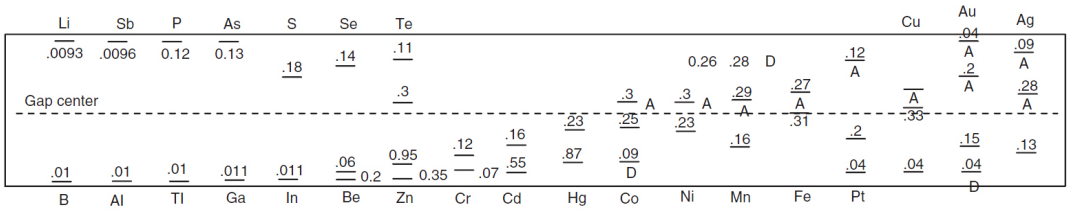

Figure 6.1: Levels of impurities in Ge band gap according to [14].

Furthermore, dislocations in the crystal lattice can cause charge trapping. Dislocation-free material can be grown nowadays, but it is not appropriate as detector material. A certain amount of dislocations serves as a sink for vacancies so that the divacancy-hydrogen complex, which introduces additional acceptor levels, i.e. charge traps, can be avoided. Therefore, the dislocation density is controlled during crystal growth and lies between 500 and $5000\,\mathrm{cm}^{-2}$ [52], providing material, which can be operated as detector material and does not suffer from severe trapping.

Other sources of trapping may be point defects like Shottky defects where oppositely charged ions are missing in the lattice. Frenkel pairs, where an atom is not in its foreseen place in the lattice, are creating vacancies and appear in interstitial positions instead. Irradiation with electrons above $1\,\mathrm{MeV}$ creates Frenkel-pairs in germanium [53]. Unfortunately electron trapping can not be excluded completely as a certain amount of dopant impurities and dislocations is intentionally introduced in the fabrication procedure and is needed to operate the crystal as a detector.

On the contrary, fast neutron bombardment of the germanium crystal with energies of more than $1\,\mathrm{MeV}$ produces displacements or even displacement cascades and leads to hole trapping exclusively. The mechanism of neutron damage is well understood [54]. After experiments with a high neutron flux, the segment energy resolution is deteriorated where the holes are collected. The core signal is also affected because hole migration also influences a signal on the core electrode.

Moreover, the geometrical configuration is essential for the influence of the trapping effects. The longer the traveled distance in the detector is, the larger the probability for trapping will be as the charges can find more traps to interact with. One can define a mean free drift time or drift length in the first instance. The energy deficit will scale with the collection path, which allows for correction using PSA. The drift velocity depends on the electric field, which is determined by the geometry of the electrodes. In a germanium detector with a distance of about $35\,\mathrm{mm}$ between the electrodes, a large travel length is found. The variance in the drift length is responsible for the observed left tailing and line broadening. For the perfect Gaussian peak shape, the full width at tenth maximum relative to the half maximum is $\frac{FWTM}{FWHM} = 1.82$. Trapping causes a tail on the low energy side of the peak due to charge carrier loss and increases the ratio $\frac{FWTM}{FWHM}$. As an agreement with the manufacturer, this ratio must not exceed 2. The segment peak shape is close to the Gaussian curve, but in the core electrode, where the electrons are collected, tailing is observed, i.e. a larger ratio $\frac{FWTM}{FWHM}$. The

observed tailing due to incomplete charge collection, for example, causes a deviation from the pure gaussian shape.

To begin with, the effect of trapping on the expected pulse shape is shown for a special case. All electron-hole-pairs are created near one boundary of the active volume. The signal pulse then corresponds to the motion only of the carrier species which is collected at the opposite boundary. It is assumed that the mean free path is constant and that only electron trapping is observed in a planar configuration. Some of the charge will be lost, at least temporarily, from the signal pulse. If no detrapping takes place, the loss is permanent and the resulting pulse takes the form

$$Q(t) = \{ \begin{array}{ll} \frac{Q_0 \tau_T}{t_e}(1 - e^{-t/\tau_T}) & (t \leqslant t_e) \\ \frac{Q_0 \tau_T}{t_e}(1 - e^{-t_e/\tau_T}) & (t \geqslant t_e) \end{array}$$

where τ_T is the mean free drift time of the electrons before trapping occurs and t_e the collection time for the electrons. Permanent trapping attenuates the amplitude of the pulse and bends the curve of the rise of the pulse sub-linearly. In shallow traps, the electrons can be released by thermal excitation and can be collected slightly delayed. Detrapping is temperature-dependent. Electrons are excited thermally proportional to $\exp(\frac{-E_T}{kT})$ [16].

There is another geometrical effect on trapping. In coaxial detectors made from a crystal with preferential trapping of one charge carrier type, one observes less trapping if the trapped charge carrier moves radially outward from the high electric field close to the central electrode towards the lower field at higher radii. This effect is disadvantageous concerning undamaged detectors which show electron trapping. In case of neutron damaged detectors, where severe degradation due to hole trapping is observed, the geometry becomes advantageous.

6.2 Model for trapping correction

Hole trapping is consulted to model trapping behavior. Darken et al. [55] developed a model which takes disordered regions and simple defect structures into account. According to this model, disordered regions contribute dominantly to trapping although point defects are causing hole trapping as well. Fast neutrons induce a defect cascade, which presents a cluster of defects with a macroscopic dimension of around $200\,\text{Å}$ in the crystal. The disordered region, i.e. the defect cluster, causes the electric field to be distorted in the μm region. These regions are negatively charged, attractive for holes, and repulsive for electrons. A simplified model with only disordered regions is satisfactory due to the higher cross-section of the defect clusters compared to simple defects [55]. Translating these results to electrons enabled the correction for electron trapping.

Some crucial relations and quantities are displayed in this section under the assumption of no detrapping. The drift velocity of the charge carriers depends on the field strength [22]. The electric field strength varies across the detector volumes. The

velocity rises linearly with the electric field strength, followed by a sub-linear increase until it saturates [22]. There are two components of the velocity, the statistical root mean square velocity v_{rms} and the more prominent drift velocity $\vec{v}_d$ following the field lines as a result of the externally applied electric field. Cross-sections for trapping are velocity-dependent. The field-dependent trapping rate for electrons or holes at a specific position in the detector is proportional to $< \sigma v >$ with the trapping cross-section σ for a particular free charge state and the "microscopic" velocity v, averaged over all populated states. With the macroscopic disordered regions and the mentioned drift velocity, the following expression is valid

$$< \sigma v > \propto Q \frac{v_d}{E}$$

with the charge state of the trapping center Q, the local field strength E and the local drift velocity v_d. The trapping rate for electrons and holes is given by

$$\frac{dq}{dt} = - < \sigma v > N_t q \leftrightarrow q(t) = q_0 \cdot e^{-\int_0^t <\sigma v> N_{e,h} dt'} \tag{6.1}$$

with the density of trapping centers N_t.

Trapping leads to a loss in the collected charge. The charge dQ_i induced on electrode i during the migration of one carrier type in a time interval can be derived from the Ramo theorem (see section 2.1)

$$\frac{dQ_i}{dt} = -\frac{q_{e,h}(t)}{q_0} \cdot (\vec{\nabla}\phi_i \cdot \vec{v}_{e,h})$$

with ϕ_i as the weighting potential of electrode i and the drift velocity $v_{e,h}$ of electrons or holes and drift time $t_{e,h}$. By evaluating the time integral along the drift path of the electrons and holes, the collection efficiencies $\eta_{e,h}$ are given by

$$\eta^i_{e,h}(\vec{x}_0) = -\int_{t_0}^{t_e} (\vec{\nabla}\phi_i \cdot \vec{v}_{e,h}) \cdot \frac{q(t)}{q_0} dt$$

for a unit of charge created at the interaction position in the detector $\vec{x}_0 = \vec{x}(t_0)$ with the collection time for the charge carriers [56]. These partial collection efficiencies mainly reflect the weighting potential arising from the geometry and calculated with SIMION. The integral over the current to segment i per unit charge gives the total recorded charge after collection. In case of negligible trapping of electrons and holes, the total collection efficiency is $\eta_{tot} = \eta_e + \eta_h = 1$.

In practice, one finds individual charge collection efficiencies for both carriers in each detector position. The total collection efficiency can be approximated with a Taylor expansion, which can be stopped after the first order term and results in

$$\eta^i_{tot}(\vec{x}_0) = 1 + (N_e s^i_e(\vec{x}_0) + N_h s^i_h(\vec{x}_0)) \tag{6.2}$$

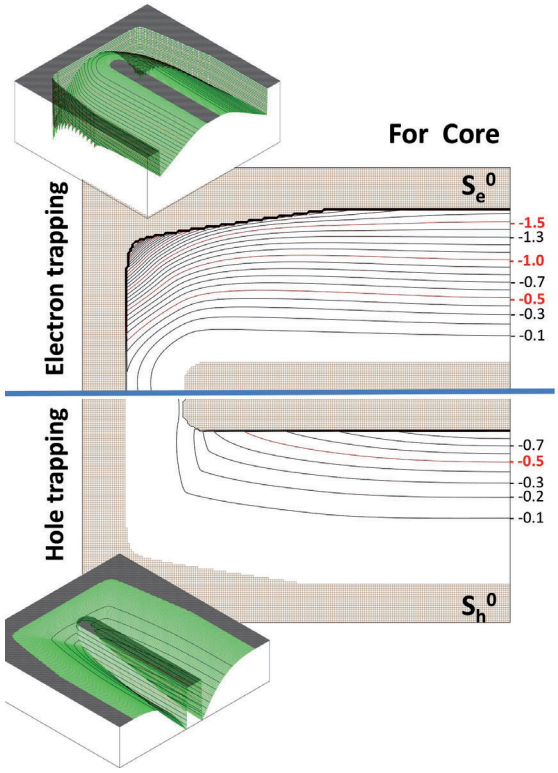

Figure 6.2: Trapping sensitivities plots for a cut through the center of the detector. Relative sensitivities to electron and hole trapping are shown for the core [57].

with the sensitivities for both carriers s_e^i and s_h^i and the densities of electron traps N_e and hole traps N_h describing the partial collection efficiencies for electrons and holes. The trapping sensitivity

$$\begin{aligned} s_{e,h}^i = \frac{d\eta_{e,h}^i}{dN_{e,h}}|_{N_{e,h}=0} &= -\int_0^{t_e} (\vec{\nabla}\phi_i \cdot \vec{v}_{e,h}) \cdot \frac{d}{dN_{e,h}} \frac{q_{e,h}(t)}{q_{e,h}(0)}|_{N_{e,h}=0} dt \\ &= -\int_0^{t_e} (\vec{\nabla}\phi_i \cdot \vec{v}_{e,h}) \int_0^t < \sigma v > dt' dt \end{aligned} \tag{6.3}$$

depends on the interaction position and is calculated for any position in the detector on a grid of $2\,\mathrm{mm}$ in three dimensions. The results are shown in figure 6.2 and are provided as libraries which can be used online during data acquisition [57, 58].

The collection efficiency is used to correct for the energy deficit arising from trapping and is calculated with

$$E_{corr} = E/(1 + s_e^i \cdot N_e + s_h^i \cdot N_h) = \frac{E}{\eta_{tot}} \tag{6.4}$$

This model is not used exclusively for hole trapping, although it is derived from hole trapping in neutron damaged detectors. The trapping sensitivities have shown to be

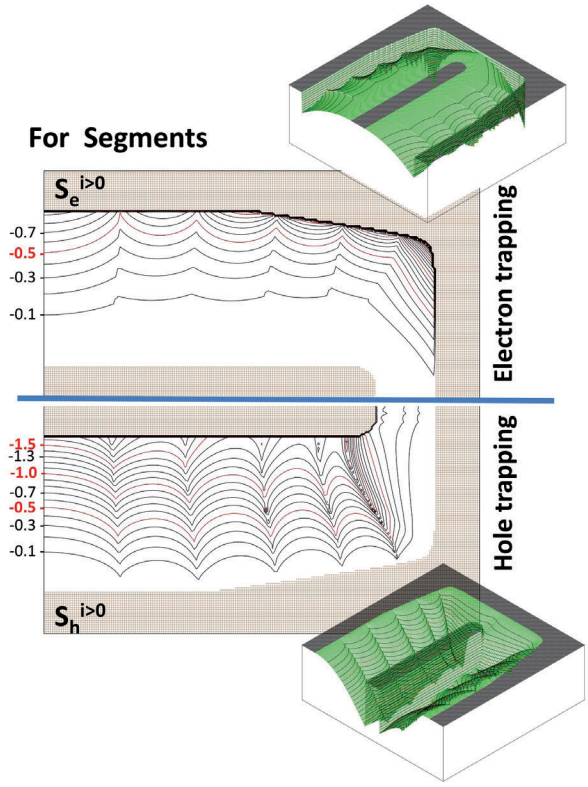

Figure 6.3: Trapping sensitivities plots for a cut through the center of the detector. Relative sensitivities to electron and hole trapping are shown for the segments [57].

applicable to correct for electron and for hole trapping in neutron damaged but also undamaged detectors.

6.3 Experimental analysis of electron trapping

By means of PSA, the effect of electron trapping can be demonstrated in a two-dimensional plot, where the centroids of the measured energies for radius intervals $\Delta r = 4\,\mathrm{mm}$ are plotted versus the radius. The centroid of the full energy peak is shifted due to trapping depending on the radial position of the interaction. Larger radii lead to a longer travel distance for electrons, i.e. a larger charge loss or a lower peak centroid. In the coaxial part of the crystal, the distribution of the centroids can be fitted with

$$E(r) = \frac{r^2 \cdot \ln(r_i/r)}{b \cdot \ln(r_o/r_i)} + a. \tag{6.5}$$

This equation reflects the electric field in a coaxial symmetry and matches the measured values for radial dependency with the interaction position at radius r, the inner

r_i and the outer radius r_o and the fit parameters $a = 1332.42$ and $b = 794$.

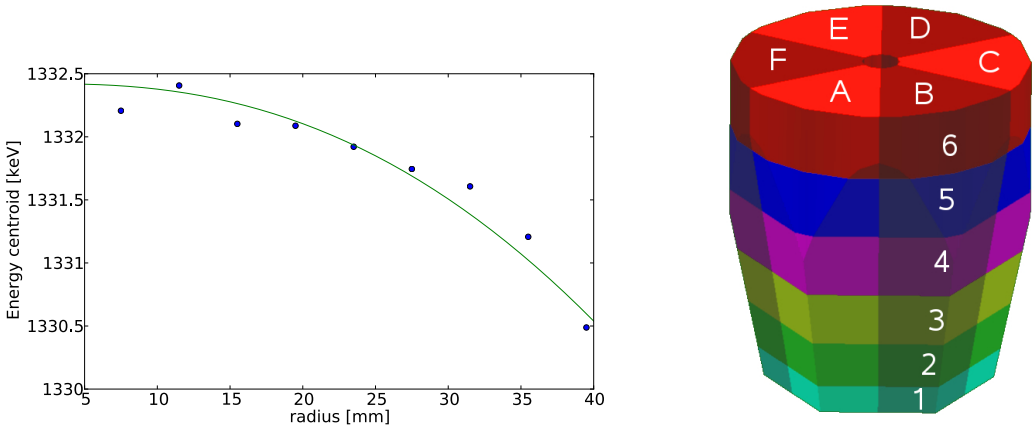

(a) Centroids vs. radius plot

(b) View of crystal

Figure 6.4: A clear energy deficit with rising radius is observed due to electron trapping as the electrons are collected at the core electrode.

The calculated trapping sensitivities from section 6.2 are mainly described by the weighting field of the electrodes. For each interaction position determined via PSA, the corresponding value for the trapping sensitivity is taken from the library. In figure 6.2, the equipotentials for the trapping sensitivities are plotted for a cut through the center of the detector. In figure 6.5 the relation between radius and trapping sensitivity is shown as an example at the detector depth of $z = 70\,\mathrm{mm}$ for the core and the segment electrodes for real events, where the position of the interaction was determined with the PSA. The electron sensitivity equals zero close to the central electrode and is largest at the outer electrode, i.e. at large radii. For the holes, the opposite behavior is observed. The core is more sensitive to electron trapping while the segments are more sensitive to hole trapping. The spread in the segment curves arises from the shape of the angular segmentation geometry, the anisotropic drift velocity, the collection time, and the weighting potentials.

Furthermore, a correlation between the measured energy deficit and the calculated sensitivity is observed. Higher sensitivities correspond to lower energies due to an energy loss caused by trapping. All measured energies from onefold events at $1.3\,\mathrm{MeV}$ are plotted versus the trapping sensitivity obtained from formula 6.3 shown in figure 6.2. The distribution of the points is shown individually for the six rings in figures 6.6 and 6.7 in the left plots for detector B002. A linear fit (blue line) has shown to agree with the contribution. The slope of a linear fit gives an information about the scaling of the trapping sensitivity for correction with N_e and N_h in equation 6.4. The standard deviation between the fit and the measured data $\sigma = \sqrt{\frac{1}{n-1}\Sigma_{i=1}^{n}(E_{meas} - fit)^2}$ is quite large with about $0.92 - 0.98\,\mathrm{keV}$ and corresponds to a FWHM of $\sigma \cdot 2.35 = 2.162 - 2.303\mathrm{keV}$. This deviation reflects the natural distribution of the events around

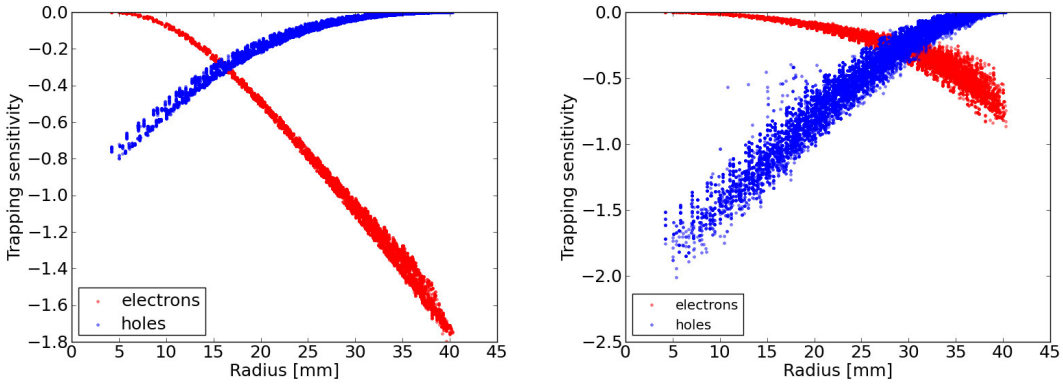

(a) Radius vs. trapping parameter core ring 4

(b) Radius vs. trapping parameter segments ring 4

Figure 6.5: Radius vs. trapping sensitivities at detector depth $z = 70\,\mathrm{mm}$ for interaction positions determined by the PSA for a measurement with detector B002.

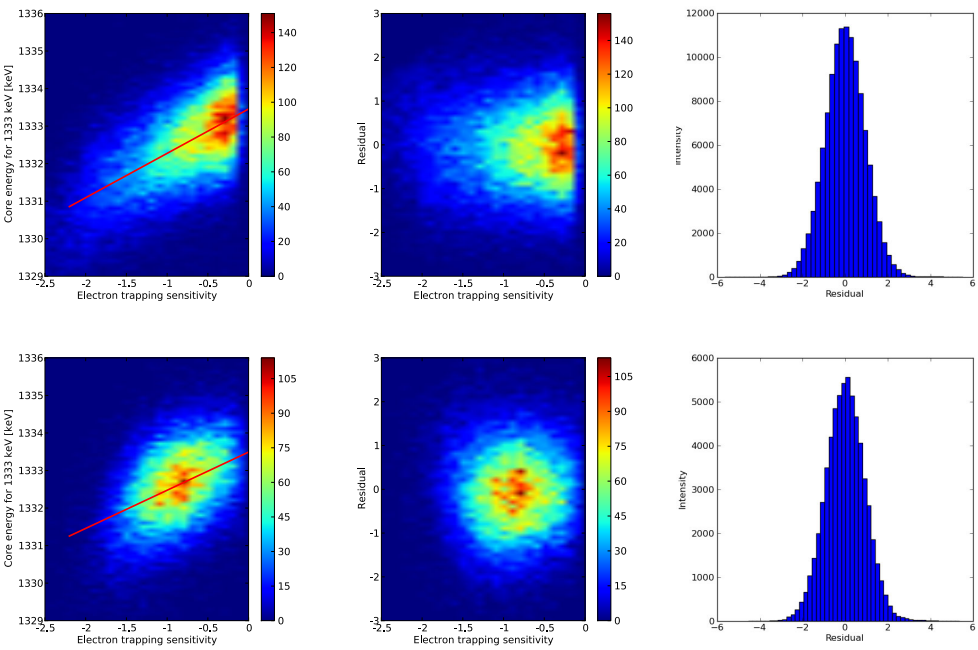

(a) Measured energy vs. calculated sensitivity with linear fit

(b) Residuals

(c) Histogram of residuals

Figure 6.6: (a) Measured peak energy vs. calculated sensitivity for the first two rings for onefolds at $1.33\,\mathrm{MeV}$. (b) Residuals comparing the measured energy values to the fit for each event and (c) a histogram of the residuals.

the centroids in the spectra, i.e. the FWHM for a small radius interval. To check the quality of the fit, the residuals are plotted versus the trapping sensitivity (center plots

in figures 6.6 and 6.7). The scattering around zero is approximately equal in the hole x range. The fit using the centroids would show a much smaller standard deviation but has the disadvantage of not taking into account the different intensities for the individual sensitivity intervals. The small nonlinear component at smallest sensitivities in the first ring results from the weak electric field in the front corners. Additionally, the residuals are plotted in a histogram and show a symmetric distribution around zero (right plots in figures 6.6 and 6.7).

This relation between energy and sensitivity is analyzed separately in different detector regions. A reasonable discrimination is a ring-wise comparison which arises from the segmentation of the detector. The trapping sensitivity differs across the crystal with depth z and therefore also the slope of the fit. There is a known quantity, which also changes with crystal depth, that is the impurity concentration. In turn, the impurity concentration correlates with the electric field (see equation 2.2). In a coaxial HPGe detector the electric field is determined not only by the applied voltage and the geometry but also by the concentration of donor impurities. At larger radii the electric field is mainly caused by the donor impurities (see Fig. 6.9)[17]. Therefore, a stronger electric field is found for higher impurity concentrations. The slopes of the linear fits are generated ring-wise for two detectors which show opposite impurity gradients along z (detectors B002 and C002). The slopes show inverse proportionality to the impurity concentration given by the manufacturer in the coaxial part of the crystal. The detector B002 shows a higher impurity concentration in the front and a smaller slope of sensitivities while C002 with lower concentration in the front gives a steeper slope. The leftmost point in plot (a) shows the slope of ring six, the rightmost point, the slope of ring one. Rings three to six show a linear dependence between the slope and the impurity concentration whereby ring six diverges a little due to the passivated back plane which acts as a dead layer. The higher impurity concentration shows less pronounced trapping due to a higher electric field which results in a higher carrier velocity. On the one hand, the points for ring one and two show a different trend with more trapping despite the higher concentration. In this front part of the detector, the electric field is non-uniform and differs significantly from the coaxial part.

In detector C002, the trend of shallower slope, respectively less observed trapping with rising impurity concentration, is observed as well as pushed-off slopes in the front part. This effect underscores the E^{-1} dependence on the trapping probability as the detector has more efficiency at larger radii and the drift velocities are not saturated so that a difference in the field strength has a larger impact than at lower radii.

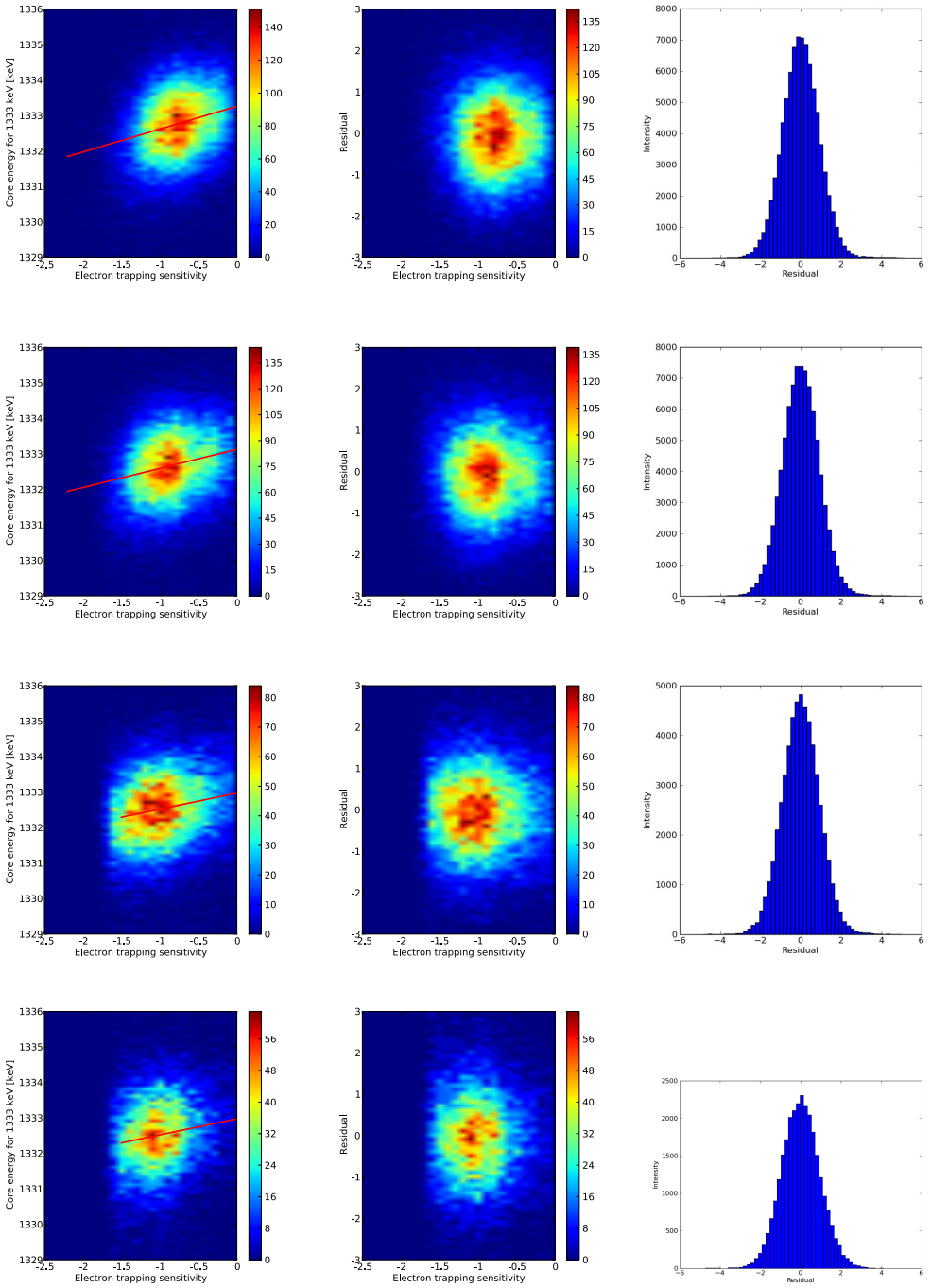

(a) Measured energy vs. calculated sensitivity with linear fit

(b) Residuals

(c) Histogram of residuals

Figure 6.7: Measured peak energy vs. the calculated sensitivity in common with figure 6.6 for rings 3 to 6 of the detector.

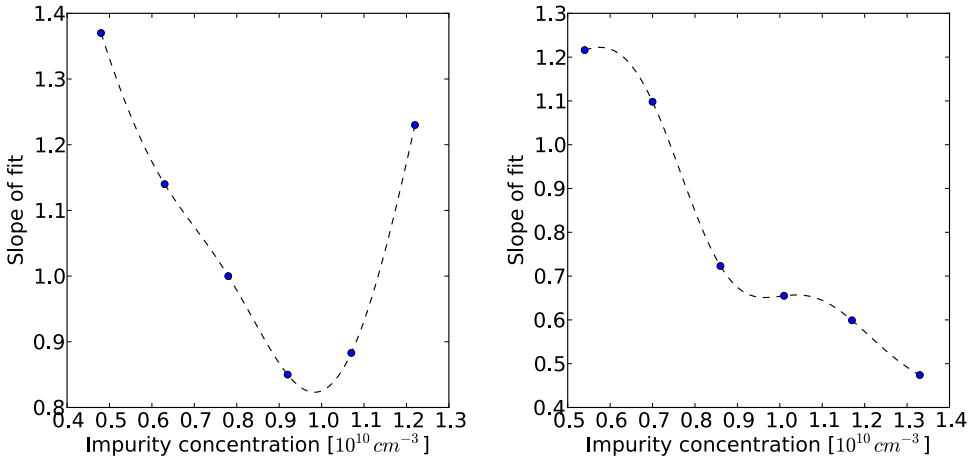

(a) B002 - low impurity concentration in the back; high impurity concentration in the front of the detector

(b) C002 - low impurity concentration in the front; high impurity concentration in the back of the detector

Figure 6.8: Impurity concentration vs. slope of fit from figures 6.6 and 6.7 for each ring derived from $1.33\,\mathrm{MeV}$ (^{60}Co).

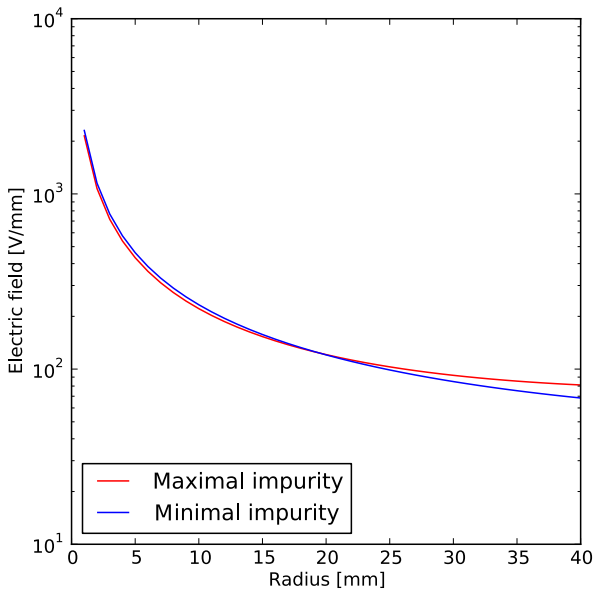

Figure 6.9: The radius dependence of the electric field is plotted for the minimal (blue - $4.8 \cdot 10^{9}\mathrm{cm}^{-3}$) and maximal (red - $1.22 \cdot 10^{10}\mathrm{cm}^{-3}$) impurity concentration in detector B002 at its operation voltage of 5000V according to equation 2.2.

Applied correction

Another way to show trapping is a contour plot where the energies and not only the centroids are drawn versus the radius for onefolds (see figure 6.10). The color code shows the intensity depending on the radius and on the measured energy. The energy deficit at larger radii displays electron trapping. In these contour plots the results for ring one in detector B002 are shown as the effect is strongest there but also the benefit coming from the correction. The uncorrected core spectrum (a) is compared with the one after correction (b) with an evident reduction of the radius dependence, thus smaller FWHM. Electron trapping is also visible in the segments (c), less pronounced though. The correction can also be applied here and results in figure 6.10 (d). The averaged signal of core and segments shows an improvement compared to the individual signal (chapter 5). Of course, these spectra suffer from trapping as well (e). The average of the corrected core and segment energies gives the best final result. The table 6.3 shows projections from these six figures to radius $= 0$. The projections of (a), (c) and (f) are shown as a two-dimensional plot in figure 6.11. A significant improvement of the energy resolution is achieved by trapping correction and by averaging of core and segment signals. Trapping is compensated by shifting the measured energies to higher values on an event-by-event basis and narrowing the total distribution down to a lower FWHM. The calculated trapping sensitivity displays the simulated electrical field in the detector. However, these values are applied in combination according to equation 6.4 by fitting the parameters N_e and N_h to the measured energy deficit. A scan varying the parameters is performed either for the whole detector or individually for certain detector regions. For the displayed example of the first ring in detector B002, the best correction is achieved with the parameters $N_e = 1/1000$ and $N_h = 1/10000$. The parameters were chosen to optimize the FWHM of the average of the corrected core and segment energies.

	FWHM [keV] at $1.33\,\mathrm{MeV}$					
	Core		Segments		Core and segment average	
	uncorrected	corrected	uncorrected	corrected	uncorrected	corrected
Ring 1	2.487	2.194	2.169	2.011	2.120	1.893
Ring 2	2.305	2.147	1.975	1.916	1.949	1.834
Ring 3	2.175	2.11	1.948	1.932	1.864	1.829
Ring 4	2.146	2.093	1.967	1.959	1.855	1.826
Ring 5	2.166	2.129	1.967	1.968	1.846	1.831
Ring 6	2.164	2.141	1.933	1.937	1.858	1.857

Table 6.1: FWHM at $1.33\,\mathrm{MeV}$ for onefold spectra for each ring of detector C002 individually. The values for the first ring correspond to the contour plots in Fig. 6.10

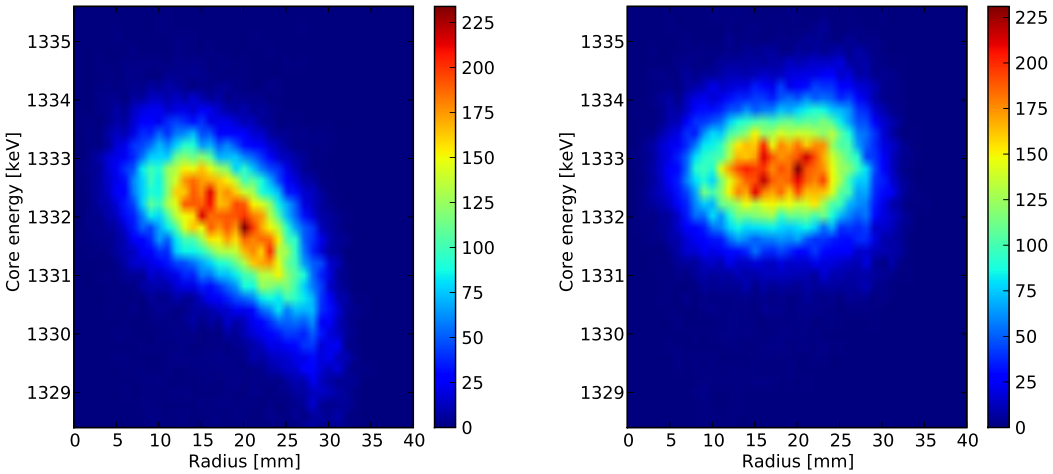

(a) Core

(b) Core corrected

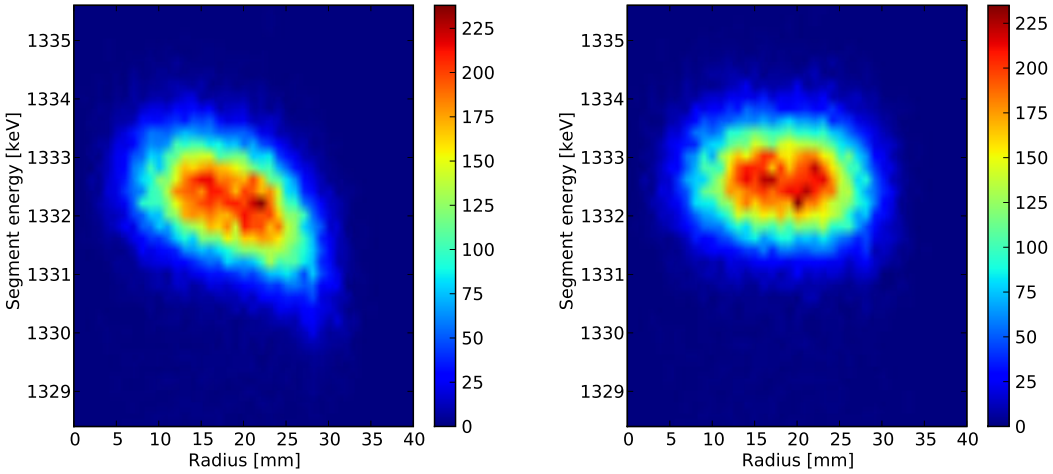

(c) Segments

(d) Segments corrected

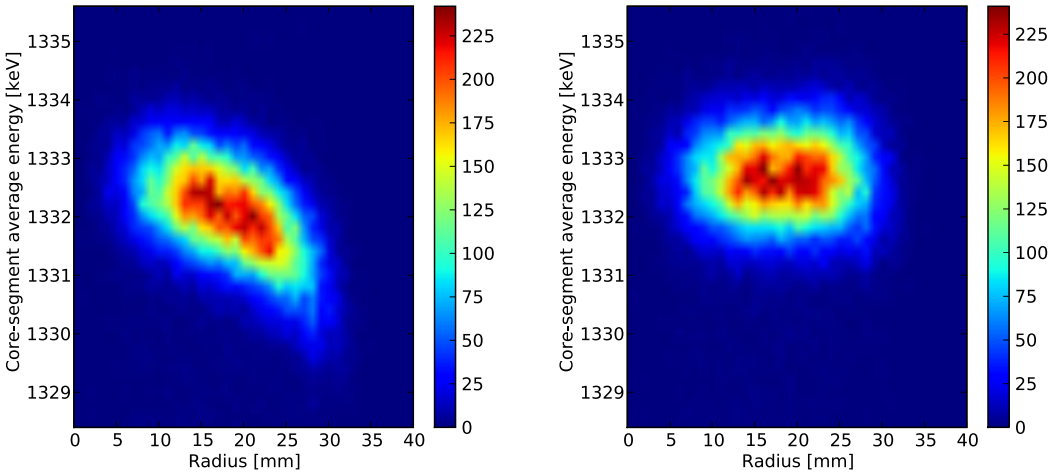

(e) Core segment average

(f) Corrected core segment average

Figure 6.10: Energy vs. radius matrices at $1.33\,\mathrm{MeV}$ in first ring of detector C002. A detailed description is found in the text.

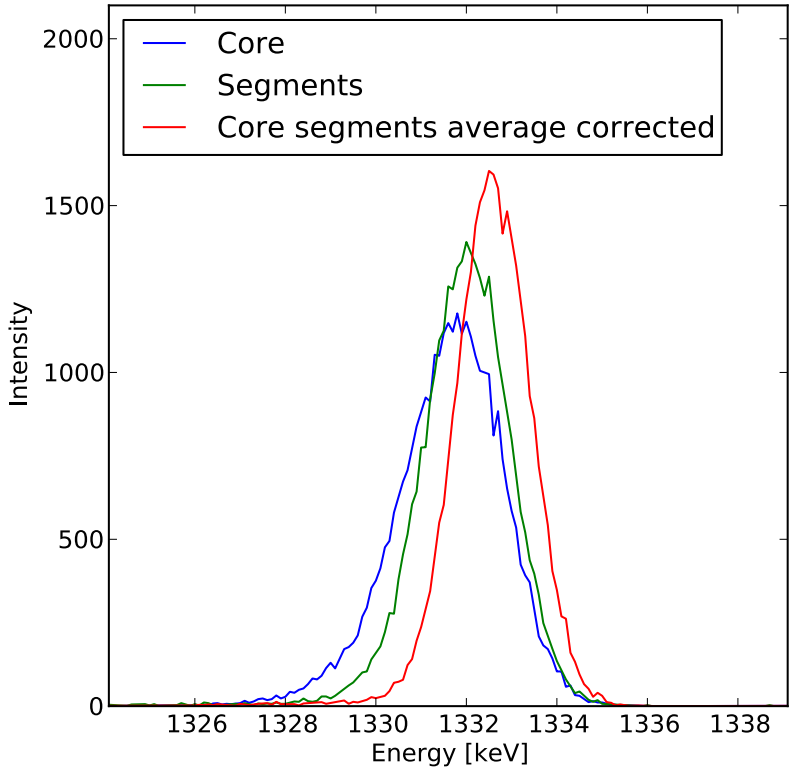

Figure 6.11: Spectra for core, segments and average of corrected core and segment energy (projections of 6.10 (a),(b) and (f)). The FWHM values are given in Tab. 6.3.

For the coaxial part of the detector, the centroids are plotted again for radius intervals of $4\,\mathrm{mm}$ in figure 6.12. The applied correction is demonstrated by the shift of the centroids, while also the energy resolutions are improved in the averaged signal to $1.82\,\mathrm{keV}$ at $1.33\,\mathrm{MeV}$. An example of a plot with the fit using ROOT libraries is shown in figure 6.12 (d). The ideal parameters for the coaxial part of detector C002 are: $N_e = 1/2050$ and $N_d = 1/14000$.

Now, all onefold events in the whole detector are taken into account with individual correction factors for each ring. The final results are shown in table 6.3 for the detectors B002 and C002. Both detectors show a significant improvement in energy resolution after the averaging of the core and the segments and after corrections for trapping. The improvement of the corrected energy resolution amounts to 18 respectively 19% relative to the uncorrected core spectrum.

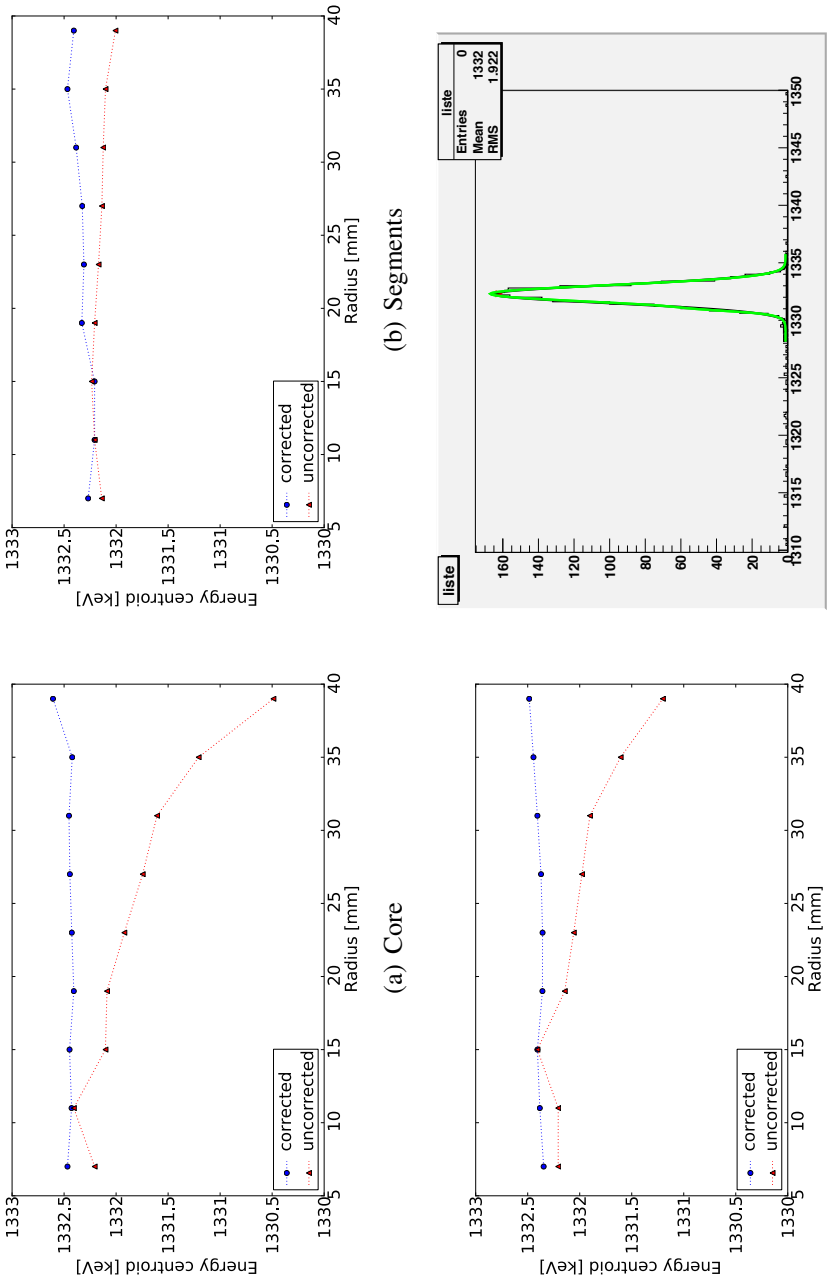

(a) Core (b) Segments (c) Core segments average (d) Fit example at radius of 30 mm.

Figure 6.12: Centroids of the $1.33\,\mathrm{MeV}$ line are plotted for radius intervals of $4\,\mathrm{mm}$ for all onefold events in the coaxial part of the detector. Figure (d) shows an example of a spectrum for the corrected core segments average peak at $30\,\mathrm{mm}$ radius with a FWHM of $1.93\,\mathrm{keV}$.

Detector	B002		C002	
	uncorrected	corrected	uncorrected	corrected
core	2.28	2.079	2.251	2.154
segments	2.026	1.986	2.004	1.979
average of core and segments	1.977	1.865	1.882	1.833

Table 6.2: FWHM for onefolds at $1.33\,\mathrm{MeV}$ in detectors B002 & C002 before and after trapping correction.

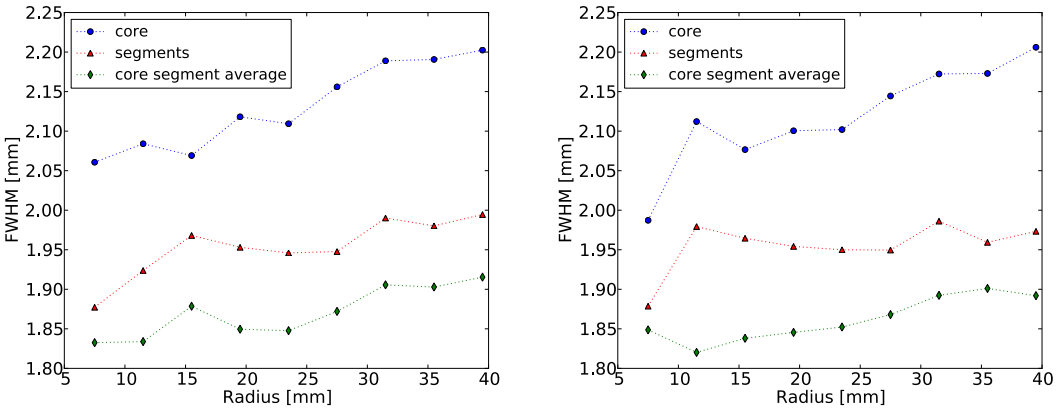

(a) Uncorrected FWHM (b) FWHM after trapping correction

Figure 6.13: FWHM for spectra in radius intervals of $\Delta r = 4\mathrm{mm}$ in the coaxial part of detector C002 for the core, the segments, and the core segment average signals.

Position-sensitive energy resolution

Another interesting correlation exists between the energy resolution and the detector region. The effect of trapping results not only in a deficit in the charge collection, which shifts the peak to lower energies, but also a peak broadening is observed. In figure 6.13, the FWHM for spectra in radius intervals $\Delta r = 4\,\mathrm{mm}$ in the coaxial part of the detector are shown for the core, the segments, and the average of core and segment energies for single hit events at $1.33\,\mathrm{MeV}$. Looking at the core signal resolution, there is a clear decrease of energy resolution with an increasing radius of the interaction position, i.e. on the core electrode the FWHM is best close to the inner electrode. This signal is mostly influenced by electron trapping and just weakly by hole trapping. Even after trapping correction the resolution in a Δr interval does not change significantly, while the centroid is shifted to its original energy.

For the segments, the behavior is different. Both partial trapping probabilities affect the FWHM so that the best energy resolution is achieved between the electrodes. In the segments, the impact from electron trapping is much larger than from holes in the core, so that a superposition from both trapping sensitivities is seen. The trend in

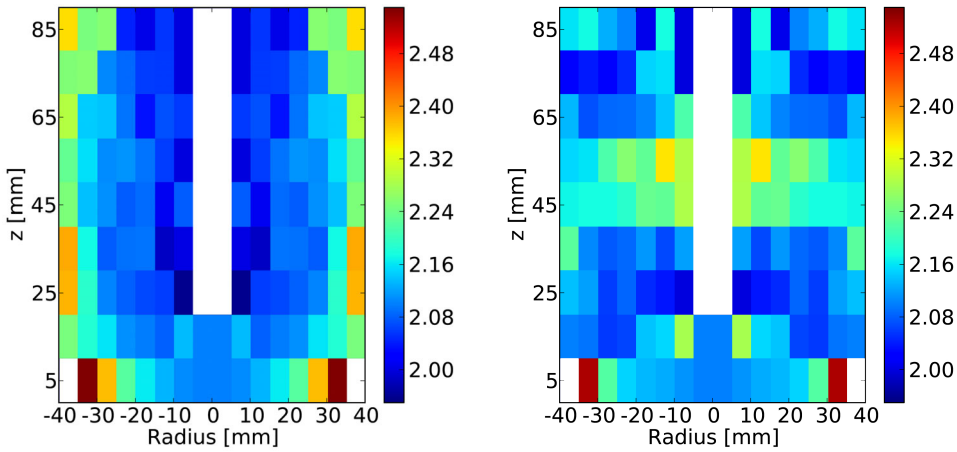

(a) Core FWHM (b) Segments FWHM

Figure 6.14: FWHM for the core and the segments at $1.33\,\mathrm{MeV}$ for $\Delta r = 5\,\mathrm{mm}$ and $\Delta z = 10\,\mathrm{mm}$ detector rings measured with detector B002 in ATC1.

the energy resolution with a rising radius is less pronounced than on the core. Also for the segments, trapping correction does not improve the resolution in the radius intervals.

Furthermore, the energy resolution is analyzed depending on the crystal depth $\Delta z = 10\,\mathrm{mm}$ and on the radius ($\Delta r = 5\,\mathrm{mm}$). The results are shown in figure 6.14 (a) for the core and (b) for the segments. The plots are symmetric around $r = 0$ and show the FWHM for rings of Δr and Δz.

The electric field varies not only with the radius but also with the crystal depth as a result of the geometry as well as the impurity concentration. In the front corners, where the field strength is very low, the energy resolution is the worst. The distance between the electrodes is large and the electric field is inhomogeneous. Therefore, the drift velocity is low for both charge carriers, which increases the trapping probability. This behavior is also seen in the segment resolution in the front corners.

Fano and "K" factor

The uncorrected core energy resolution values from events in the coaxial part of the detector B002 are now used to describe the trapping contribution to the FWHM of the peaks (see Fig 6.15). Trapping shifts the peak to lower energies and broadens it. The least effect of trapping is found on the core signal close to the inner electrode. The inner part of the detector gives much better results in a radius interval Δr than the outer part, where the field is weak and the travel path for the electrons is larger. According to [56], the contribution to the FWHM from trapping is given by:

$$W_X = 2.35\sqrt{\epsilon K E_0 (1 - \eta(r))} \tag{6.6}$$

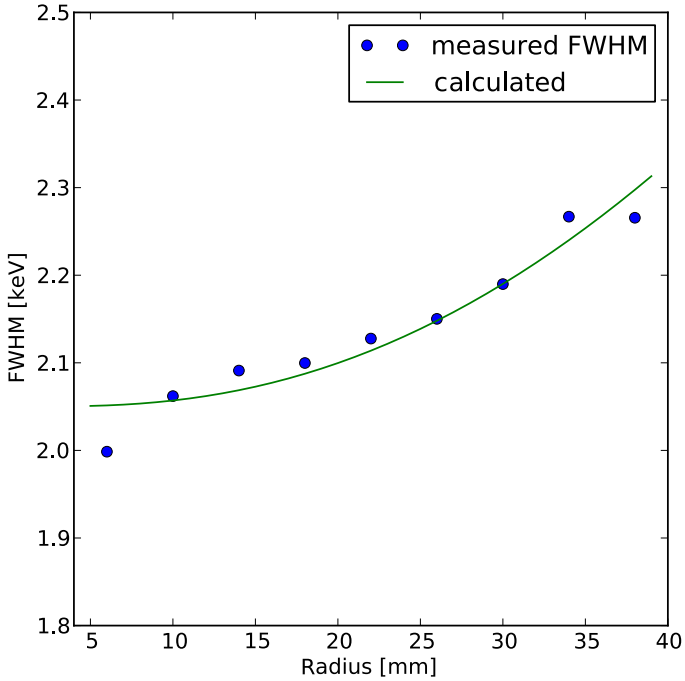

Figure 6.15: FWHM versus radius in the coaxial part of detector B002 at $1.33\,\mathrm{MeV}$. The influence of trapping on the energy resolution is clearly visible and described by the fit function.

with the average ionization energy $\epsilon = 2.96\mathrm{eV}$, the γ-ray energy E_0, the charge collection efficiency η, and a factor K, which can be seen as a value for the variation of the traps analog to the Fano factor.

However, looking at the core FWHM at lowest radii, one gets the best achievable resolution which is $2\,\mathrm{keV}$. The trapping contribution is minimal here due to the short travel length to the electrode for the electrons and a high electric field. It is considered negligible. Hence, the remaining contribution to the observed peak width, besides the electronic noise, is the statistics of the charge generation process. The electronic noise can be determined with the electronic response to an injected pulser signal. The FWHM of the pulser in detector B002 equals $1.47\,\mathrm{keV}$. The error contribution arising from the statistics in the charge creation process including the Fano factor F is described in equation 2.4.

The electronic noise and the error contribution from charge statistics are independent of the radius. The charge collection efficiency η is calculated by means of the trapping sensitivity for a coaxial detector (see figure 6.4) and the ideal parameter $N_e = 1/2050$ and amounts to a minimum value of $99.902\,\%$ at the outer electrode. Hole trapping can be neglected as it is one order on magnitude less pronounced.

Equation 2.3 combines the three error contributions to the total FWHM. The con-

stant K in the summand 6.6 of the total FWHM and the Fano factor F in equation 2.4 are used as fit parameters to describe the radius dependency, which is observed in the measured FWHM.

The resulting parameters of the least square fit are $F = 0.095 \pm 0.006$ and $K = 59.9 \pm 0.6$. For the estimated error, an uncertainty of $50\,\mathrm{eV}$ in the FWHM was included. The meaning of the Fano factor is already described in chapter 2. This result for the Fano factor is between the average value 0.062 ± 0.02 determined with a $86\mathrm{cm}^3$ germanium detector [59] and the standard value of 0.129 ± 0.003 in literature [24]. The value for the K factor obtained in [56] with a lithium drifted detector is much higher (~ 340), which correlates with a much lower charge collection efficiency.

Energy dependence of trapping

The knowledge about the energy dependence of the trapping probability is essential for trapping correction. Not only because the correction has to be applied on a wide range of γ-ray energies, but also because of energy splitting in multifold events (see subsection 6.3). Trapping is expected to be linearly proportional to the energy in the relevant energy range, because the amount of the created charge increases linearly with the energy. According to figure 6.16, where the slopes of the fit (see Fig. 6.6) of the trapping sensitivity are plotted versus the energy, a linear relation between energy and trapping is proven. Three measurements are combined in this plot. The ^{60}Co data, which were used to study the radial dependence with the two lines at 1.17 and $1.33\,\mathrm{MeV}$ as well as the transition in ^{137}Cs at $662\,\mathrm{keV}$ and the most prominent lines from ^{152}Eu provide a good distribution in the region of interest.

Not only shows the trapping sensitivity an energy dependence, but also the improvement of the FWHM of the core signal. The correction itself and the relative correction $\frac{\Delta E}{E}$ rise from low to higher energies. The relative correction is lower at low energies due to a worse position resolution (more details in next subsection).

Multifold events

Only about 30% of the events are onefold events at $1.33\,\mathrm{MeV}$ (see fig. 5.11). About 40% are twofolds. For the correction of trapping effects in events with more than one segment involved, the energy splitting as well as the energy need to be known. Therefore, the ratios between the individual segment energies, where the interactions take place, and the sum of all segment energies are calculated. The correction for the partial energy of the core, which is also measured in hit segment i, is

$$\frac{E_{seg_1}/E_{segsum}}{1 + s_e^i \cdot N_e + s_h^i \cdot N_h}$$

Generally $E_{core} \approx E_{segsum}$ is valid. The total correction for the core is then

$$E_{core_{corr}} = E_{core} \cdot \left(\frac{E_{seg_1}/E_{segsum}}{\eta_{tot,pos_1}} + \frac{E_{seg_2}/E_{segsum}}{\eta_{tot,pos_2}} + ... \right)$$

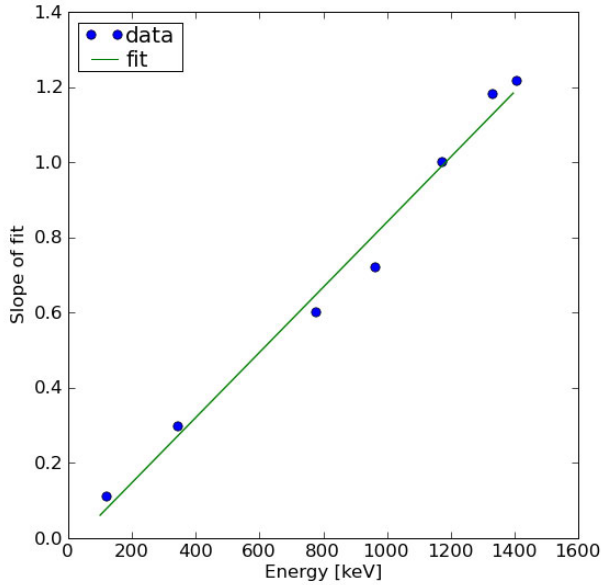

Figure 6.16: Energy versus slope of fit shown in figure 6.6 for the coaxial part of detector C002 at different energies.

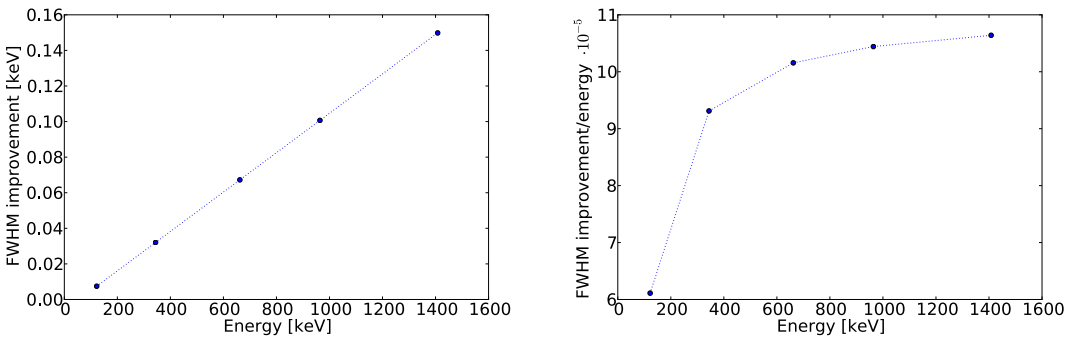

(a) Improvement of FWHM (b) Improvement/energy

Figure 6.17: The energy resolution of the core is improved by the correction. The difference in the energy resolution between the uncorrected and the corrected spectra is shown in (a) for detector B002 at different energies. (b) shows the relative improvement for different energies.

with the total collection efficiency η_{tot,pos_i} for the partial energy deposited in hit-segment i.

Fold-dependent correction works best for onefolds. At higher segment-folds, the energy resolution decreases (see fig 5.12). The correction is less effective with rising fold due to the uncertainty in each position determination and the electronic noise con-

tribution from each involved preamplifier. The crosstalk correction, which is described in the previous chapter, needs to be applied as well. The final results of the FWHM are shown in table 6.3 with results for up to fold six for corrected and uncorrected spectra.

	Core		Segments		Core and segment average	
Fold	uncorrected	corrected	uncorrected	corrected	uncorrected	corrected
1	2.29	2.129	2.091	2.052	1.978	1.865
2	2.198	2.079	2.356	2.349	2.037	1.968
3	2.165	2.074	2.613	2.647	2.109	2.054
4	2.125	2.042	2.883	2.949	2.19	2.149
5	2.106	2.058	3.198	3.216	2.288	2.263
6	2.057	2.015	3.412	3.405	2.268	2.285
all	2.194	2.154	2.611	2.567	2.081	2.011

Table 6.3: FWHM [keV] at $1.33\,\mathrm{MeV}$ for up to 6 folds in detector B002 before and after correction. The values in the last line show the FWHM combining all observed hit-segment multiplicities.

The main uncertainty for trapping correction is the limited position resolution. The estimated uncertainty of the PSA shows a normal distribution around a mean position. The FWHM of the interaction position resolution varies roughly linearly as a function of γ-ray energy from $8.5\,\mathrm{mm}$ at $250\,\mathrm{keV}$ to $4\,\mathrm{mm}$ at $1.5\,\mathrm{MeV}$, and has an approximately constant value of about $4\,\mathrm{mm}$ in the γ-ray energy range from $1.5\,\mathrm{MeV}$ to $4\,\mathrm{MeV}$ [48, 60]. The lower position resolution at lower energies arises from a worse signal-to-noise ratio. Especially in the very small transient signals of a couple of mV, this effect is very relevant. The error in the position determination is shown in figure 6.18 in the x error bars. The position uncertainty leads to a higher energy uncertainty in the process of trapping correction thus worse FWHM. The variation in energy can be calculated with the propagation of uncertainty $\Delta E = |\frac{dE(r)}{dr}| \cdot \sigma_r$ from equation 6.5.

$$\Delta E(r) = \frac{1}{b \cdot \ln(r_2/r_1)}(2 \cdot x \cdot \ln(r_1/r) - x) \cdot \Delta r$$

The above equation gives the energy uncertainty and is displayed in the y error bars in plots 6.18 (a) and (b). At larger radii the FWHM of the PSA results in a FWHM of the energy of up to $0.6\,\mathrm{keV}$ at largest radii and $0.02\,\mathrm{keV}$ at lowest radii. Unfortunately, most of the detection efficiency is found at larger radii due to the cylindrical geometry.

The next step is to combine all events from the whole detector for each segment-hit multiplicity. The final results combining all segment multiplicities for trapping correction and averaging for detector B002 at $1.3\,\mathrm{MeV}$ is $2.01\,\mathrm{keV}$. This result is shown in Tab. 6.3, where the FWHM values for individual segment multiplicities are also given.

For detector C002 the results from ^{152}Eu are presented in the spectrum in figure 6.19 and the FWHM of the most prominent lines in table 6.3. These results underscore

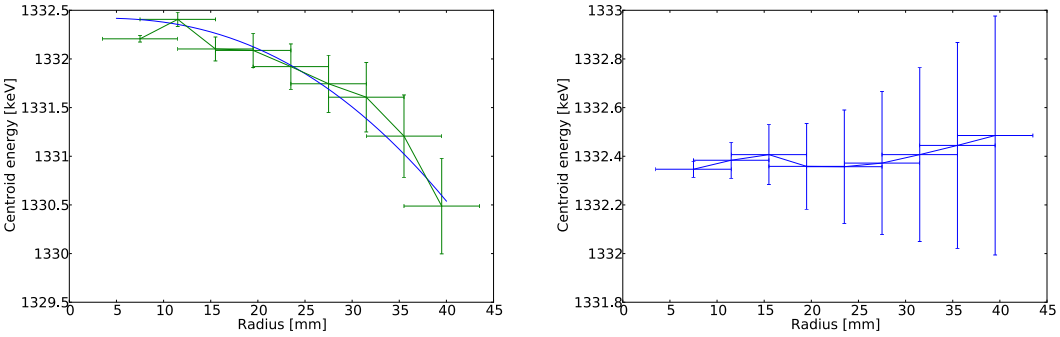

(a) Uncorrected centroids with fit

(b) Corrected centroids

Figure 6.18: Centroids of the spectra of uncorrected core signals in radius intervals of in $4\,\mathrm{mm}$ with a fit according to equation 6.5 with position and energy errorbars (a). The trapping corrected energy positions of the core are shown with the same errorbars in (b).

that trapping correction can be applied to the whole energy range with a significant improvement in the energy resolution. While averaging of core and segment signals the improvement is best at lower energies due to a dominant contribution of the electronic noise, the gain in energy resolution after trapping correction stands out at higher energies.

Energy [keV]	Core FWHM	Segments FWHM	Averaged FWHM	Final FWHM
121.8	1.494	1.208	1.057	1.054
344.3	1.632	1.751	1.407	1.395
778.9	1.874	2.183	1.777	1.749
964	1.992	2.314	1.88	1.851
1408	2.231	2.563	2.129	2.089

Table 6.4: FWHM [keV] from most prominent ^{152}Eu peaks for all events measured with detector B002 for core and segments compared to the FWHM of the averaged and corrected signals.

A high focus is still put on the PSA to further improve the position resolution. From the energy error bars it is obvious that this would lead to a further improvement in the energy resolution. Additionally, multiple interactions are considered as one interaction, which gives the best agreement between the measured and calculated waveforms. For a total absorption of a γ-ray of $1.3\,\mathrm{MeV}$, the most probable amount of interaction points is 4, for example double interactions in two segments [4]. Therefore, a considerable amount of the onefold events has more than one interaction in a segment. A decomposition of these interaction points is intended [61]. Improved PSA and decomposition algorithms will lead to an even more effective trapping correction.

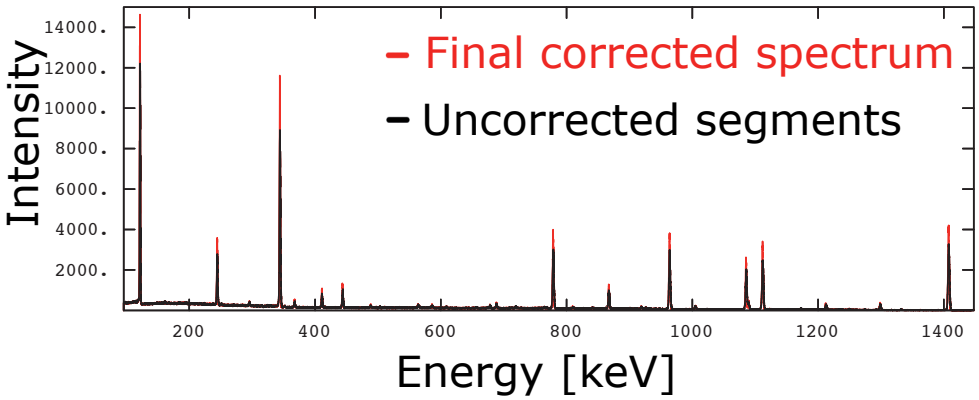

Figure 6.19: ^{152}Eu spectrum for the uncorrected segment-sum (black) and the final spectrum after trapping correction and signal averaging (red) for events of all observed hit-segment multiplicities of up to 10.

Chapter 7

Summary and outlook

A new generation of γ-ray detector arrays is required for the study of new challenging nuclear structure topics. The γ-spectrometer AGATA, based on the principle of γ-ray tracking, will provide the requirements to meet the challenges for nuclear spectroscopy arising from the next generation of beam facilities. The AGATA demonstrator is a subset of five triple cluster detectors of the whole AGATA array and is designed to show the feasibility of position-dependent γ-ray detection by means of γ-ray tracking, which is based on pulse shape analysis.

The first four asymmetric AGATA triple cluster detectors comprising three 36-fold segmented HPGe detectors were successfully assembled, optimized, and installed in Legnaro, the current host laboratory of the AGATA demonstrator (see Fig. 7.1). All 444 signals are operational, most of them with specified energy resolutions. The average energy resolution values for the segments of each crystal are in the range of $0.965 - 1.144\,\mathrm{keV}$ at a γ-ray energy of $60\,\mathrm{keV}$. At $1.33\,\mathrm{MeV}$, the average segment energy resolution values are between 1.943 and $2.131\,\mathrm{keV}$ for the 12 crystals. The crosstalk properties of the highly packed analog preamplifier circuitry and of the detector assembly were investigated. The crosstalk level between different detectors was found to be negligible on a level below 10^{-5}. A low crosstalk level of 10^{-3} was found for the segment signals within the same HPGe detectors caused by the interplay of the core coupling capacitor and the capacities of the 36 segments.

The assembly of the new ATC detectors required an elaborated optimization procedure with regard to electronic properties, including modifications of the electrical grounding scheme of the triple cluster detectors. Initially, high frequency oscillations caused major disturbances and were sustainably removed from the first four triple cluster detectors. The improvement of the detector properties, which was achieved through the optimization of the electronic grounding and of the preamplifier settings, was presented for the first triple cluster detectors. The energy resolution values of the three crystals in ATC1 and Fast Fourier Transform spectra clearly state the improvement of the signal quality for the pulse shape analysis and for the energy resolution values.

The novel segmented high-purity germanium AGATA detectors provide a redundant energy measurement from independent core and segment electrodes. The signal-

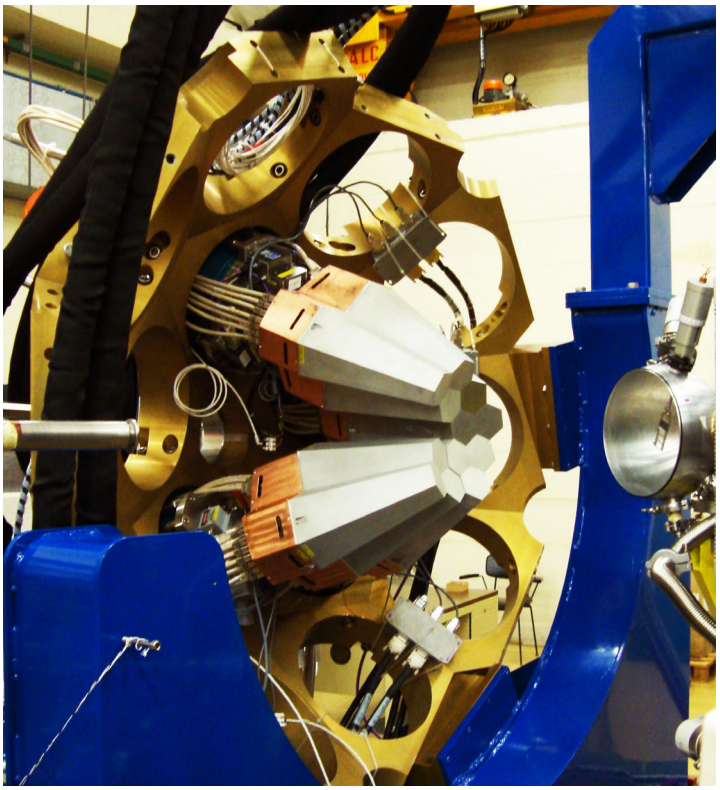

Figure 7.1: The four AGATA triple cluster detectors mounted in the AGATA demonstrator frame in INFN Legnaro facing the open target chamber at the focal plane of the PRISMA spectrometer during the first campaign of in-beam γ-ray spectroscopy experiments.

to-noise ratio is improved through averaging of the core and of the segment signals. The electronic noise is considerably reduced, especially at low γ-ray energies. In combination with crosstalk correction a significantly improved energy resolution is achieved also for high segment multiplicities. At low energies of $60\,\mathrm{keV}$, the averaging of the core and the segment signals leads to an improvement by the expected factor of almost $\sqrt{2}$ to $0.87\,\mathrm{keV}$. The combination of the signals can already be applied on-line during data-taking with the acquisition system or off-line with stored data.

In AGATA ν-type germanium detectors, position-dependent electron trapping is observed on the core electrode as an inherent property of the new crystals. These trapping effects were studied and corrected utilizing the position information obtained by means of the pulse shape analysis. The electron trapping correction itself leads to an improvement in the energy resolution of $100 - 300\,\mathrm{eV}$ for events with only one hit segment at γ-ray energies of $1.33\,\mathrm{MeV}$. In combination with the signal averaging and the crosstalk correction, the energy resolution was further improved. For the first time, a total energy resolution of $2.01\,\mathrm{keV}$ at $1.33\,\mathrm{MeV}$ was achieved with a segmented, large volume germanium detector. Add-back spectra of segment multiplicities of up

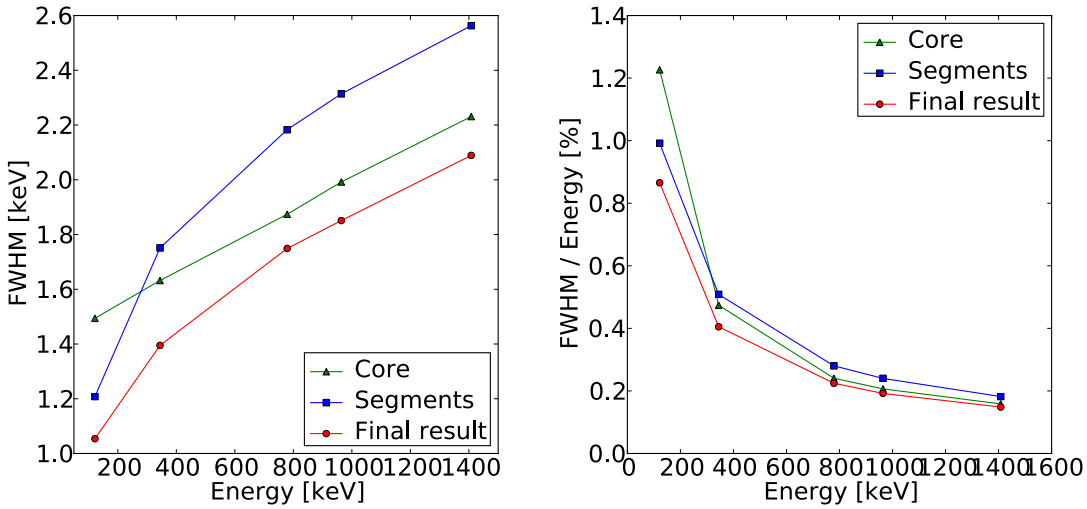

Figure 7.2: FWHM values measured with ^{152}Eu for the core (green), for the uncorrected segment sum (blue), and the final result after trapping correction and signal averaging (red) for events of all observed hit-segment multiplicities of up to 10 are shown in the left figure. The relative energy resolution is plotted in (b).

to 10 were included. The energy-dependence of the corrections was shown in a range from $122\,\mathrm{keV}$ to $1.41\,\mathrm{MeV}$ with ^{152}Eu measurements. The figure 7.2 (a) gives an overview of the finally achieved energy resolution compared to the core and segment sum FWHM. The relative energy resolution is shown in figure 7.2 (b). The improvement from the segment sum to the corrected FWHM is approximately $20\,\%$.

Position-dependent energy resolution was measured individually for small detector volumes benefitting from the position information of the pulse shape analysis. The position information allowed for calculating the Fano factor by separating the noise arising from the statistics of the charge creation process from the noise arising from incomplete charge collection. The new value equals $F = 0.095 \pm 0.005$. The standard value from literature for large volume germanium detectors is 0.129 ± 0.003.

The corrections ensure a significantly improved operation of the new AGATA detectors. But in fast beam experiments with heavy nuclei, a large neutron background is produced and corrupts the germanium detectors. These neutrons induce crystal damages which cause hole trapping. Hole trapping deteriorates the energy resolution of the segments. It can be corrected in the same way as electron trapping. The crystal damages can be removed by annealing the detectors. However, the operation time of the detectors and thus the period between annealing cycles can be extended through trapping correction.

The feasibility of the principles of γ-ray tracking and pulse shape analysis has been demonstrated by the AGATA collaboration in several commissioning and nuclear structure experiments. The position resolution amounts to $4\,\mathrm{mm}$ at $1.33\,\mathrm{MeV}$ [48].

An additional increase in the position resolution through the pulse shape analysis algorithms will be accomplished and will lead to further improvement of the energy resolution by applying the new analysis methods based on trapping and average corrections.

Bibliography

[1] AGATA homepage.
URL http://www-win.gsi.de/agata/

[2] D. Bazzacco et al., Technical Proposal for an Advanced Gamma Tracking Array for the European Gamma Spectroskopy Community, Tech. rep. (September 2001).
URL http://www-win.gsi.de/agata/Publications/Agata_pub-proposal.pdf

[3] J. Eberth and J. Simpson, From Ge(Li) detectors to gamma-ray tracking arrays-50 years of gamma spectroscopy with germanium detectors, Progress in Particle and Nuclear Physics 60 (2) (2008) 283 – 337.

[4] I. Y. Lee et al., Rep. Prog. Phys. 66 (2003) 1095–1144.

[5] The official GRETINA Homepage.
URL http://grfs1.lbl.gov/

[6] P. Reiter et al., The new position sensitive triple cluster detector for AGATA, in: In Proc. of the 13th Int. Symp. on Capture Gamma-Ray Spectr., Vol. 1090, 2009, pp. 97–101.

[7] J. Eberth et al., Encapsulated Ge detectors: development and first tests, Nucl. Instr. and Meth. A 369 (1996) 135–140.

[8] J. Eberth et al., The EUROBALL Collaboration, Prog. Part. Nucl. Phys. 38 (1997) 29.

[9] J. Eberth et al., The MINIBALL Collaboration, Prog. Part. Nucl. Phys. 46 (2001) 389.

[10] Th. Kröll and D. Bazzacco, Simulation and anylysis of pulse shapes from highly segmented HPGe detectors for the γ-ray tracking array MARS, Nucl. Instrum. Meth. A 463 (2001) 227–249.

[11] AGATA Technical Design Report.
URL http://npg.dl.ac.uk/AGATA/TDR/TDR_EUJRA.pdf

[12] R. Venturelli and D. Bazzacco, Adaptive gridsearch as pulses hape analysis algorithm for g-tracking and results, LNL-INFN(REP)-204 (2005) 220.

[13] INFN (National Institute of Nuclear Physics) homepage.
URL http://www.lnl.infn.it/

[14] E. Simoen and C. Claeys, Metals in Germanium, Elsevier, 2007.

[15] B. Birkenbach et al., Determination of space charge distributions in highly segmented large volume HPGe detectors from capacitance-voltage measurements, Nucl. Instr. and Meth. A 640 (1) (2011) 176 – 184.

[16] G. F. Knoll, Radiation Detection and Measurement, John Wiley & Sons, Inc., New York, 2000.

[17] A. Starostin, A. Beda, Germanium detector with an internal amplification for investigating rare processes, Physics of Atomic Nuclei 63 (2000) 1297–1300, 10.1134/1.855787.
URL http://dx.doi.org/10.1134/1.855787

[18] Z. He, Review of the Shockley-Ramo theorem and its application in semiconductor gamma-ray detectors, Nucl. Instr. Meth. A 463 (2001) 250–267.

[19] S. Ramo, Currents induced by electron motion, Proc. IRE 27 (1939) 584.

[20] E. Gatti and P. F. Manfredi, Processing the signals from solid-state detectors in elementary-particle physics, Della Societa Italiana di Fisica, 1986.

[21] L. Mihalescu, Principles and methods for γ-ray tracking with large volume germanium detectors, Ph.D. thesis, Rheinische Friedrich-Wilhelms-Universität Bonn (2000).

[22] B. Bruyneel et al., Characterization of Large Volume HPGe Detectors. Part I: Electron and Hole Parameterization, Nucl. Instr. and Meth. A 569 (3) (2006) 764–773.

[23] B. Bruyneel, Characterization of Segmented Large Volume, High Purity Germanium Detectors, Dissertation, IKP der Universität zu Köln (2006).

[24] H. R. Bilger, Fano Factor in Germanium at 77K.

[25] E. Farnea and D. Bazzacco, A Monte Carlo code for the AGATA array, LNL-INFN(REP)-202 (2004) 158.

[26] E. Farnea, AGATA: comparison of the A120, A180 configurations.
URL http://agata.pd.infn.it/documents/simulations/comparison.html

[27] H. Hess, Ph.D. thesis, IKP der Universität zu Köln, in preparation.

[28] G. Pascovici et al., WSEAS Trans. Circuits Syst. 7 (6) (2008), p. 470.

[29] F. Zocca et al., Wide dynamic range front-end electronics for gamma spectroscopy with a HPGe crystal of AGATA, in: IEEE Nuclear Science Symposium Conference Record, CD-ROM, Paper N03-2, ISBN 1-4244-0923-3/07, Honolulu, HI, USA, Oct. 27 - Nov. 3, 2007 156.

[30] A. Pullia et al., The AGATA charge sensitive preamplifiers with built-in active-reset device and pulser, in: 2004 IEEE Nuclear Science Symposium Conference Record, vol. 3, Rome, Italy, 16-22 October 2004, 1411-1414.

[31] WolframMathWorld on Fast Fourier Transform.
URL `http://mathworld.wolfram.com/FastFourierTransform.html`

[32] The LeCroy product page.
URL `http://www.lecroy.com/Oscilloscope/OscilloscopeModel.aspx?modelid=1965`

[33] G. Pascovici, private communication (2011).

[34] P. Horowitz and W. Hill, The Art of Electronics, Cambridge Universtity Press, 1980.

[35] A. Pullia, private communication (2009).

[36] P. v. Dijk, Contacts in motion, AMP Automotive Development Centre.
URL `http://www.pvdijk.com/pdf/contacts_in%20_motion.pdf`

[37] P. v. Dijk, Contact problems due to fretting and their solutions, AMP Automotive Development Centre.
URL `http://www.tycoelectronics.com/documentation/whitepapers/pdf/5jot_2.pdf`

[38] H. W. Ott, Noise Reduction Techniques in Electronic Systems, 2nd Edition, John Wiley & Sons, 1988.

[39] The Fischer Elektronic homepage.
URL `http://www.fischerelektronik.de/`

[40] H. W. Ott, Partitioning and layout of a mixed-signal pcb.
URL `http://www.hottconsultants.com/pdf_files/june2001pcd_mixedsignal.pdf`

[41] CTT Homepage.
URL `http://www.ctthomas.de`

[42] X-Ray Instrumentation Associates, User's Manual, Digital Gamma Finder (DGF) Model DGF-4C, version 3.02 Edition (July 2003).

[43] B. Bruyneel et. al., Crosstalk properties of 36-fold segmented symmetric hexagonal hpge detectors, Nucl. Instr. and Meth. A 599 (2-3) (2009) 196 – 208.

[44] B. Bruyneel, P. Reiter, A. Wiens et al., Crosstalk corrections for improved energy resolution with highly segmented HPGe-detectors, Nucl. Instr. and Meth. A 608 (1) (2009) 99 – 106.

[45] L. Corradi, The Tandem-ALPI accelerator: facility usage, INFN, Laboratori Nazionali di Legnaro.
URL http://www.lnl.infn.it/t̃andem/Reports/arep2005a.pdf

[46] E. Fagotti et al., Operational experience in PIAVE-ALPI complex.
URL http://www.lnl.infn.it/H̃IAT09/papers/oral/FR4T.pdf

[47] F. Recchia, Installation of the AGATA Demonstrator and commissioning experiments at LNL, J. Phys.: Conf. Ser. 205 (2010) 012045.
URL http://stacks.iop.org/1742-6596/205/i=1/a=012045

[48] P.-A. Söderström et al., Simulations and In-beam Measurements of the Interaction Position Resolution of the AGATA HPGe detectors, Nucl. Instr. Meth. A 638 (1) (2011) 96 – 109.

[49] J. Kiko et al., Noise reduction for proportional counter signals in the GNO solar neutrino experiment, Nucl. Instrum. Methods A 482 (1-2) (2002) 434 – 440.

[50] Wolfram Mathworld - Covariance.
URL http://mathworld.wolfram.com/Covariance.html

[51] R. Venturelli et al., Fold-dependent energy correction in segmented germanium detectors, LNL-INFN(REP)-198 (2002) 156–157.

[52] I. Romandic, Workshop on Germanium-Based Detectors and Technologies, Germanium Crystal Growth at Umicore, 2010.
URL http://physics.lbl.gov/MaKaC/materialDisplay.py?contribId=18&sessionId=1&materialId=slides&confId=0

[53] V. Markevich et al., Radiation Performance of Ge Technologies, Elsevier, 2007.

[54] L. Reggiani and V. Mitin, Recombination and ionization processes at impurity centres in hot-electron semiconductor transport, La Rivista del Nuovo Cimento (1978-1999) 12 (11) (2005) 1–90.

[55] L. S. Darken et al., Mechanism for fast neutron damage of Ge(HP) detectors, Nucl. Instr. and Meth. A 171 (1) (1980) 49 – 59.

[56] T. W. Raudorf et al., Effect of charge carrier trapping on germanium coaxial detector line shapes, Nucl. Inst. and Meth. A 255 (3) (1987) 538 – 551.

[57] B. Bruyneel, A. Wiens et al., Correction for neutron damage in AGATA detectors using Pulse Shape Analysis, LNL Annual Report (2011) 64–65.
URL `http://www.lnl.infn.it/ annrep/read_ar/2010/contributions/pdfs/064_A_114_A109.pdf`

[58] B. Bruyneel, A. Wiens and D. Bazzacco, Neutron damage and trapping effects, AGATA week, Lyon (2010).
URL `http://www.ikp.uni-koeln.de/research/agata/talks/LYON2010_Bruyneel.pdf`

[59] A. Owens, Spectral degradation effects in an 86 cm3 Ge(HP) detector, Nucl. Instr. and Meth. A238 (2-3) (1985) 473 – 478.

[60] F. Recchia et al., Performance of an agata prototype detector estimated by compton-imaging techniques, Nucl. Instr. and Meth. A 604 (1-2) (2009) 60 – 63.

[61] F. Crespi, Application of the Recursive Subtraction Pulse Shape Analysis algorithm to in-beam HPGe signals, Nucl. Instr. and Meth. A 604 (1) (2009) 604–611.

Acknowledgements

First of all, I would like to thank my supervisor Prof. Dr. P. Reiter for providing me with the very interesting field of study and his strong support during the past years.

Furthermore, many thanks go to Dr. J. Eberth, who is one of the experts in the germanium detector technology, for plenty of interesting and very helpful discussions.

Moreover, I would also like to thank the other current or former members of the AGATA detector group in Cologne, B. Birkenbach, Dr. B. Bruyneel, H. Hess and D. Lersch. I enjoyed very much working in this group, the work in the lab with Herbert and Daniel, and a lot of fruitful discussions, especially with Bart. Thanks to Benedikt for helping me with a lot of computer related stuff and installing NARVAL in Cologne.

I would like to express my gratitude to the locals in Legnaro, Dr. D. Bazzacco, Dr. E. Farnea, and Dr. F. Recchia, D. Rosso, and C. Fanin for their excellent support for the installation of the detectors. It was always fun to work there in an atmosphere, which was almost as good as in Cologne. I've got some insight into the advanced knowledge of the Italian cuisine from the trips to Italy.

Additionally, thanks to Dr. H. G. Thomas for his excellent know-how on the cryostats and the outstanding collaboration between his company and the detector working group.

My thanks goes also to Dr. G. Pascovici, C. Görgen and G. Richardt, Dr. A. Pullia, Dr. N. Karkour, and M. Tripon for discussions on electronics topics and the terrific work in the electronics workshop at IKP. I also would like to thank S. Thiel and his mechanical workshop for their excellent work.

Thanks to the other group members Kerstin Geibel, Raphael German, Tanja Kotthaus, Burkhard Siebeck, Michael Seidlitz, Jan Taprogge and Andreas Wendt for the excellent working atmosphere and the time spent together during breaks.

Last but not, least I would like to thank my girlfriend Sina for her patience and all her support during the past years.

Erklärung

“Ich versichere, dass ich die von mir vorgelegte Dissertation selbständig angefertigt, die benutzten Quellen und Hilfsmittel vollständig angegeben und die Stellen der Arbeit – einschließlich Tabellen, Karten und Abbildungen –, die anderen Werken im Wortlaut oder dem Sinn nach entnommen sind, in jedem Einzelfall als Entlehnung kenntlich gemacht habe; dass diese Dissertation noch keiner anderen Fakultät oder Universität zur Prüfung vorgelegen hat; dass sie – abgesehen von unten angegebenen Teilpublikationen – noch nicht veröffentlicht worden ist sowie, dass ich eine solche Veröffentlichung vor Abschluss des Promotionsverfahrens nicht vornehmen werde. Die Bestimmungen der Promotionsordnung sind mir bekannt. Die von mir vorgelegte Dissertation ist von Prof. Dr. Peter Reiter betreut worden.”

Teilveröffentlichungen:
Andreas Wiens, Herbert Hess, Benedikt Birkenbach, Bart Bruyneel, Jürgen Eberth, Daniel Lersch, Gheorghe Pascovici, Peter Reiter, Heinz-Georg Thomas for the AGATA Collaboration,
The AGATA triple cluster detector
Nuclear Instruments and Methods in Physics Research Section A: Accelerators, Spectrometers, Detectors and Associated Equipment, 618 (1-3) (2010) 223-233.

CURRICULUM VITAE – ANDREAS WIENS

Andreas Wiens
Wilhelm-Backhaus-Straße 6a
50931 Köln

(0221) 470-3620
a.wiens@ikp.uni-koeln.de

Geburtsdatum:	19. Mai 1979
Geburtsort:	Karaganda (Kasachstan)
Familienstand:	Ledig
Eltern:	Valeri Wiens Lili Wiens
Schulausbildung:	1990 bis 1996 Realschule Delbrück
	1996 bis 1999 Pelizaeus-Gymnasium Gymnasium der Stadt Paderborn
Schulabschluss:	Allgemeine Hochschulreife (1999)
Zivildienst:	September 1999 bis Juli 2000 St. Josefskrankenhaus Salzkotten
Studium:	Physik Grundstudium: WS 2000/01 bis SS 2002 Universität Paderborn
	Physik Hauptstudium: WS 2002/03 - WS 2006/07 Universität zu Köln
Studienabschluss:	Februar 2007 Diplom-Physik
Promotion:	seit März 2007 am Institut für Kernphysik der Universität zu Köln

Köln, May 16, 2011

Andreas Wiens